Materials Today Advances 22 (2024) 100488

Contents lists available at ScienceDirect

Materials Today Advances

journal homepage: www.journals.elsevier.com/materials-today-advances/

Strategies for robust electrocatalytic activity of 2D materials: ORR, OER, HER, and CO_2RR

Ali Raza [a,*,1], Jahan Zeb Hassan [b,1], Usman Qumar [c,1], Ayesha Zaheer [a], Zaheer Ud Din Babar [d], Vincenzo Iannotti [a,e], Antonio Cassinese [a,**]

[a] Department of Physics "Ettore Pancini", University of Naples Federico II, Piazzale V. Tecchio, 80, 80125, Naples, Italy
[b] Department of Physics, Riphah Institute of Computing and Applied Sciences (RICAS), Riphah International University, 14 Ali Road, Lahore, Pakistan
[c] Consiglio Nazionale Delle Ricerche, Istituto per La Microelettronica e Microsistemi (IMM), Via P. Gobetti 101, I-40129, Bologna, Italy
[d] Scuola Superiore Meridionale (SSM), University of Naples Federico II, Largo S. Marcellino, 10, 80138, Italy
[e] CNR–SPIN (Institute for Superconductors, Oxides and Other Innovative Materials and Devices), Piazzale V. Tecchio 80, 80125, Naples, Italy

ARTICLE INFO

Keywords:
2D materials
Electrocatalysis
OER
ORR
HER
CO_2 reduction
Defect engineering
Phase engineering
Interface engineering
Heteroatoms doping
Surface modification
Electrolyte optimization

ABSTRACT

Electrocatalysis utilizing 2D materials is an encouraging approach for advancing sustainable energy conversion technologies. This review explores the strategies employed to achieve robust electrocatalytic activity of 2D materials in key reactions, namely, the OER, HER, and CO_2RR. The distinct structural and electrical characteristics of 2D materials offer opportunities for rapid catalytic performance, indicating significant energy efficiency and selectivity. We systematically discuss the factors governing the electrocatalytic efficiency of two-dimensional materials, including their intrinsic properties, surface modification techniques, heterostructure engineering, and the role of defects. Furthermore, we summarize the recent advances in experimental and theoretical studies to understand the fundamental mechanisms of 2D materials with respect to their catalytic behavior. For the HER, OER, and ORR, defect engineering, phase engineering, interface engineering, and heteroatom doping techniques have been explored. In addition, in the case of the CO_2RR, surface modification, surface-structure tuning, and electrolyte and electrolyzer optimization strategies were examined. This review emphasizes prospective two-dimensional materials as efficient and sustainable electrocatalysts for energy conversion processes. Moreover, it provides future insights into this rapidly evolving field and highlights the possible challenges. In conclusion, it aims to serve as a remarkable resource for researchers seeking to harness the potential response of two-dimensional materials for sustainable energy conversion applications.

1. Introduction

Electrocatalysis plays a vital role in the production of hydrogen, oxygen, and ammonia, either as substitutes or in conjunction with conventional energy production methods. These pathways utilize atmospheric components such as water, carbon dioxide, and nitrogen as universal resources, are convertible into these products through electrochemical processes, and can be further integrated with renewable energy sources, when feasible. The development of appropriate electrocatalysts is crucial to facilitate these transformations. Specifically, attention has been drawn to the water splitting process, which yields hydrogen (hydrogen evolution reaction-HER) and oxygen (oxygen evolution reaction-OER) as clean energy carriers and the oxygen reduction reaction (ORR), capable of generating hydrogen peroxide (H_2O_2) for industrial applications. Analogously, the electrochemical reduction of carbon dioxide (CO_2 reduction reaction-CO_2RR) and nitrogen presents opportunities for sustainable production of fuels, chemicals, and fertilizers. The primary challenge lies in enhancing the electrocatalysts to improve the efficiency and selectivity of these energy conversions. Key strategies involve increasing the number of active sites on the electrodes, controlling the catalyst loading, micro-nano structuring of the catalyst, and tuning the intrinsic activity of the respective active sites. Two-dimensional (2D) materials have proven to be seminal in this context; however, further improvements are required. The

* Corresponding author.
** Corresponding author.
E-mail addresses: ali.raza@unina.it (A. Raza), antonio.cassinese@unina.it (A. Cassinese).
[1] A. Raza, J. Z Hassan, and U. Qumar contributed equally to this work.

https://doi.org/10.1016/j.mtadv.2024.100488
Received 8 January 2024; Received in revised form 2 April 2024; Accepted 6 April 2024

optimization of 2D materials for robust activity in key reactions, such as the OER, ORR, HER, and CO_2RR, has become a topic of immense research interest. To meet these energy requirements, effective electrocatalysts are vital for sustainable energy conversion and storage applications [1–6]. Expanding the family of 2D materials, ranging from graphene derivatives to MXenes, and recently synthesized transition metal carbochalcogenides (TMCCs) highlight their diversity and potential in the field of catalysis (Fig. 1a–i). Conventionally, as a basic

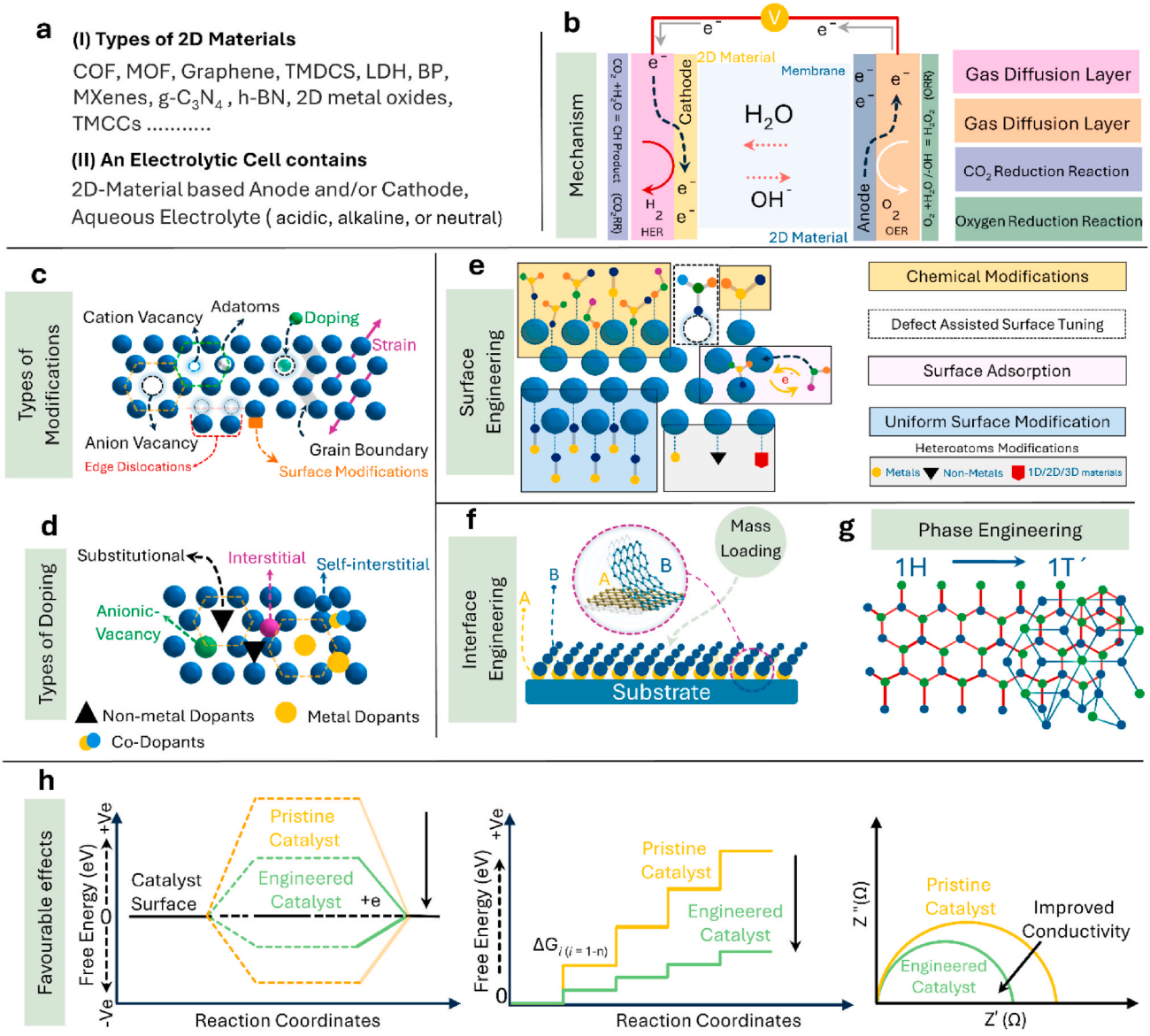

Fig. 1. Introduction to 2D materials for electrocatalysis, modification approaches, and resulting improvements. (a–i) Various members of 2D materials family; COF: Covalent Organic Framework, MOF: Metal Organic Framework, Graphene and its derivatives (e.g., Graphene Oxide, Reduced Graphene Oxide), TMDs: Transition Metal Dichalcogenides, LDH: Layered Double Hydroxides, BP: Black Phosphorous, MXenes: Transition Metal Carbides and Nitrides, g-C_3N_4: Graphitic Carbonitrides, h-BN: Hexagonal Boron Nitrides, 2D metal Oxides and recently synthesized TMCCs: Transition metal Carbo chalcogenides. (ii) Basic Components of the electrocatalytic chamber. It contains an anode and cathode, generally made up of any material of choice, 2D materials in the present case (as per the context of the review), and an appropriate aqueous electrolyte that can be acidic, alkaline, or neutral, because pH plays an important role. **(b)** Typical geometry of the electrocatalytic chamber for the splitting reaction, where the reduction of water to molecular hydrogen occurs at the cathode and oxidation occurs at the anode. The former is known as the HER, and the latter accommodates the conversion of hydroxide ions to oxygen, which is known as the OER. The cathode and anode can accompany CO_2 capture for its reduction to CH-products (CO_2 reduction reaction (CO_2RR)), and the anode can host the reduction of oxygen to H_2O_2 (ORR). **(c)** Crystallographic and morphological modification approaches applied to nanomaterials for structure-property tuning. These include vacancy creation, adatoms, doping, surface modifications (e.g., extrinsic surface functionalization), and lattice modifications such as strain, edge dislocations, and grain boundary modifications. **(d)** Doping and its various types: Dopants can be metallic (Co, Cu, etc.), non-metallic (P, O, N, etc.), and/or co-doping/hetero doping. Doping can also be induced by defects, such as vacancies, which are mediated by breaking local bonds. **(e)** Surface engineering. It involves chemical modification of the surface, edges, or both; defect-mediated chemical modifications; and physical adsorption of chemical modifiers. Uniform surface tuning and extrinsic tuning with metals, non-metals, and complex systems with 1D/2D/3D systems is another approach for surface tuning, such as interface engineering **(f)** with other 2D materials to ensure synergistic cooperation. This can be attributed to the mass loading of the catalysts during subsequent stages. **(g)** Phase transitions, particularly in TMDs, can be induced by mechanical (strain and/or external fields) and chemical (intercalation and/or doping) methods [7]. **(h)** This approach modifies the atomic structure and thermodynamic properties (Gibbs Free Energy), thereby modifying the electronic configuration, increasing the active sites, and facilitating better electron transfer and surface interactions [8]. These characteristics are crucial for guaranteeing excellent surface interactions and catalytic activity.

component, 2D materials can be used as active electrode materials (Fig. 1b) of an electrocatalytic chamber (Fig. 1a–ii). Generally, 2D materials are pronounced for their exceptional activities; however, their performance can be further tuned for a wide range of applications. In this context, various modification approaches have been applied, including crystallographic and morphological tuning such as doping, surface engineering, phase transition, and defect engineering. Panels (Fig. 1c–g) delve into such modification approaches in a systematic and tutorial manner for a comprehensive understanding. These strategies lead to the modification of the atomic structure, thereby altering the thermodynamic properties, varying the electronic configuration, increasing the number of active sites, and facilitating better electron transfer and surface interactions that are crucial for the overall catalytic performance with a good figure of merit (Fig. 1h).

Comparatively, a 2D materials are recognized for their respective features, specific to that 2D material, and for a certain reason, makes it viable in fundamental sciences and fulfills some industrial requirements. MXenes are considered better because of their intrinsically decorated surfaces, conductivity, and structural versatility [9]. Graphene, for example, is characterized by its mechanical robustness and wider surface, where there is a direct correlation between the abundant surface area and enhanced catalytic sites [10]. Edge sites within materials, such as MoS_2, are well known for their increased catalytic activity compared to the basal plane. This increased activity is attributed to the unsaturated coordination of atoms at the edges, which facilitates the adsorption and activated [11]. The introduction of defects or doping improves catalytic performance. For example, the electronic structure of graphene is modified after doping with nitrogen, which creates new active sites and enhances the catalytic performance [12]. The catalytic properties of 2D materials are fundamentally influenced by their electronic structures. Specifically, band alignment in layered materials plays a critical role in facilitating charge-transfer processes during catalytic reactions [13]. The electronic and catalytic properties of 2D materials such as MoS_2 are influenced by their thicknesses. Few-layered materials frequently display distinct catalytic activities in contrast to their bulk counterparts owing to the quantum confinement effects [14].

Specifically addressing the applications, different strategies have been applied to different 2D materials to achieve different reduction mechanisms [15,16]. Therefore, there exists a constraint or a sort of natural order, as there is no universal approach because different factors, such as specific material properties, reaction environment, interactions with reagents, and initial synthesis methods, can influence the success of a modification strategy and play a decisive role. Although there may be some general trends or principles that apply to an individual material, it is important to address each material, application, and modification individually. For example, in OR, defect engineering involving the controlled introduction of lattice imperfections, vacancies, or edge sites has been demonstrated to improve catalytic performance by inducing active sites and facilitating charge transfer [17,18]. Nonmetal doping, where nonmetallic atoms are doped into the 2D material lattice, has shown the greatest response towards the modification of electronic structure, thus increasing the catalytic response and stabilizing reaction intermediates. Additionally, metal doping, which incorporates metallic species into 2D materials, has proven effective in promoting catalytic activity by altering the surface properties and facilitating charge transfer [19–22]. In the context of *the HER*, a variety of approaches have been implemented to accelerate the electrocatalytic behavior of 2D materials [23]. Phase engineering, which involves control of the crystal phase or morphology, has been used to enrich the intrinsic catalytic response and stability. Interface engineering, which focuses on designing heterointerfaces or hybrid structures, has been employed to optimize charge transfer and improve catalytic performance. In addition, defect engineering introduces defects or vacancies that act as active sites for hydrogen adsorption/desorption [17,24]. Moreover, heteroatom doping [25], which introduces foreign atoms into 2D materials, is an evident approach to increase the catalytic response by modulating the electronic structure and adsorption properties. For *CO_2RR*, Surface modification involving the deposition of functional groups or metal nanoparticles on a 2D material surface has shown promise for improving CO_2 adsorption and facilitating reaction kinetics [26–31]. Surface structure tuning, which includes the control of surface defects, step edges, and grain boundaries, has been explored to boost catalytic activity and selectivity. In general, optimization of the electrolyte composition and electrolyzer design has been pursued to achieve efficient mass transport and tailor the reaction conditions for enhanced activity [7,26].

The present review is structured to systemically explore various reduction reactions and encompass various strategies applied to various 2D catalysts. Section 2 discusses the ORR of 2D catalysts and explores various strategies for optimizing their electrocatalytic proficiency. In addition, the subsections include defect engineering, nonmetal doping, and metal doping, which offer a means to tailor the electrical and structural characteristics of 2D materials to enhance their catalytic activity. Section 3 focuses on the HER and presents different approaches utilized to boost the electrocatalytic response of 2D materials for this reaction. The following subsections discuss defect engineering, phase engineering, interface engineering, and heteroatom doping, all of which significantly enhance the 2D materials. Section 4 examines CO_2RR and highlights various schemes intended to boost the electrocatalytic activity of 2D materials. Further subsections cover surface modification, surface-structure tuning, and optimization of electrolytes and electrolyzers, which contribute to accelerating the catalytic efficacy of two-dimensional materials in the CO_2RR. By comprehensively exploring these strategies, this study aims to provide researchers and scientists with insights into designing and optimizing robust electrocatalysts based on 2D materials for ORR, HER, and CO_2RR. Understanding the underlying principles and advantages of these strategies is crucial for developing high-performance catalysts that can advance renewable energy technologies. Additionally, this paper identifies current challenges and provides a platform for future research directions in electrocatalysis (see Fig. 2).

2. Oxygen reduction and evolution reactions

The experimental discovery of 2D graphene in 2004, which later emerged as a possible ORR catalyst, an era of 2D materials originated and piqued the interest of the scientific community [32–34]. Transition metal dichalcogenides (TMDs: MoS_2, $MoSe_2$, etc.), graphitic carbon nitride (g-C_3N_4), metal-organic frameworks, layered metals, layered transition metal oxides (MnO_2), and hexagonal boron nitride (*h*-BN) are among the materials that make up a two-dimensional family. The fabrication and utilization of these materials has been successfully performed in electrochemistry in recent years (Fig. 3) [35]. The critical qualities of these 2D materials are their dimensional attributes: they are few- or single-layer thick. Their exceptional physiochemical characteristics, including mechanical flexibility and enormous specific surface area, render them promising catalyst supports for electrochemical energy conversion. Moreover, the electrocatalytic behavior of 2D nanomaterials can be accelerated by introducing intramolecular charge transfer via defect engineering or heteroatom doping. Their exceptional electronic structures and numerous active sites make them favorable ORR catalysts [36]. Conversely, the active sites of these 2D materials can be tuned significantly, providing an additional degree of freedom to exploit their catalytic behavior, as explained in the following section. Furthermore, ORR involves a four-proton-electron shift mechanism; these mechanisms can be dissociative or associative, which is purely centered on the O_2 dissociation barrier of the catalyst surface (*) to convert O_2 into H_2O, as shown in Eqs. (1)–(8) [37]:

$$O_2 \rightarrow 2O^+ + 2e^- \quad (1)$$

$$2O^+ + 2H^+ + 2e^- \rightarrow 2OH^+ \quad (2)$$

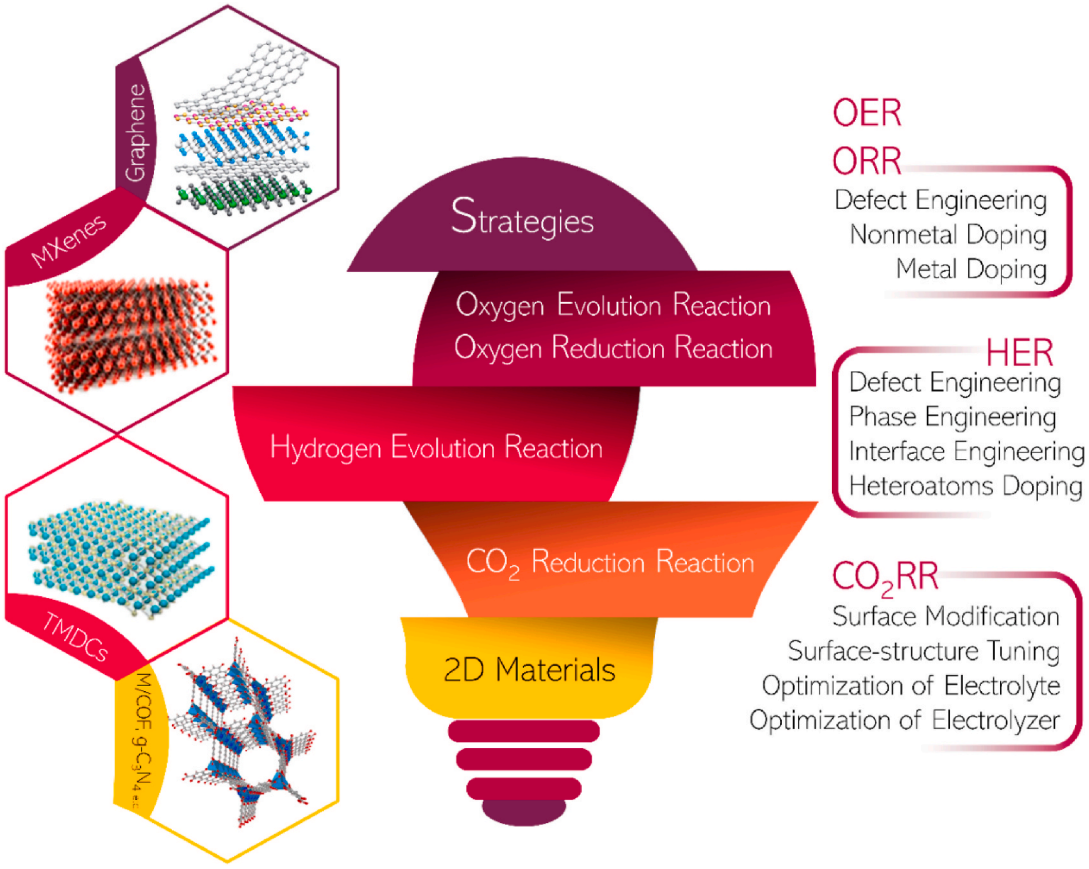

Fig. 2. Graphical summary offering a comprehensive insight into the review's content.

$$2OH^+ + 2H^+ + 2e^- \rightarrow 2H_2O \quad (3)$$

$$O_2 + e^- \rightarrow O_2^+ + 2e^- \quad (4)$$

$$O_2^+ + H^+ + e^- \rightarrow OOH^+ \quad (5)$$

$$OOH^+ + H^+ + e^- \rightarrow H_2O_2^+ \quad (6)$$

$$O^+ + H^+ + e^- \rightarrow OH^+ \quad (7)$$

$$OH^+ + H^+ \rightarrow H_2O \quad (8)$$

The adsorption-free energy (ΔG_o) of O_2 is a critical factor that influences overall ORR activity. Similar to the HER mechanism, if the catalyst efficiently binds to O_2, the reaction proceeds effectively. However, this process is constrained by the transfer of positive and negative charges to O* or OH*, respectively. In the case of catalysts with weak O_2 binding, their performance is limited by either the dissociation of the O_2 molecule involving the O-O bond (dissociative route) or by the e^--h^+ transfer to O_2* (associative way) [37]. The evaluation of catalytic progress in ORR involves limitations such as the onset potential, Tafel plots, and half-wave potential [38,39]. These factors encompass the potential ascribed to half of the current, which is influenced by the diffusion limitations. Carbon materials, known for their high conductivity, excellent corrosion resistance, and cost-effectiveness, have garnered significant research attention as potential electrocatalysts for ORR [40]. Tables 1 and 2 illustrate recent achievements in OER and ORR.

2.1. Strategies

In the realm of electrochemical reactions, many strategies have been devised and explored to enhance the performance and efficiency of various processes. This section discusses strategies that have been devised to improve electrocatalytic activity and selectivity in the context of ORR, HER, and CO_2 reduction reactions. By critically examining these strategies, we aimed to provide a comprehensive overview of the advancements in electrocatalysis that have the potential to reform current energy conversion technologies and environmental sustainability.

2.1.1. Defect engineering

Defect engineering in the context of ORR using 2D materials is an emerging field of research that holds great promise for advancing energy-conversion technologies. Defects in materials refer to structural imperfections, such as vacancies, adatoms, grain boundaries, and dopants, which also influence the material surface characteristics and electronic structure. By strategically engineering the defects in 2D materials, researchers can tailor their selectivity, stability, and catalytic response en route for ORR reactions, which is a crucial step in metal-air batteries, fuel cells, and other electrochemical energy devices [79]. Defect engineering in ORR using two-dimensional materials requires abundant consideration of the structure-property associations and precise control over defect types, concentrations, and distributions. Advanced fabrication techniques such as ion irradiation, chemical functionalization, and atomic layer deposition have been employed to introduce and manipulate defects in a controlled manner. Furthermore, several characterizations, such as scanning probe microscopy, TEM, and XRD, have been used to elucidate defect-induced modifications in the material properties [80,81]. Processes similar to the ORR are involved in the OER but in the reverse order. The variations in the free energies of oxygen adsorption and hydroxide adsorption, ΔG_o, and ΔG_{OH} determine the overall OER rate [37]. Commonly employed criteria for assessing electrocatalytic activity in OER include onset potential, Tafel slope, and most desirable to obtain 10 mA/cm^2 (η_{10}), similar to the analysis of HER

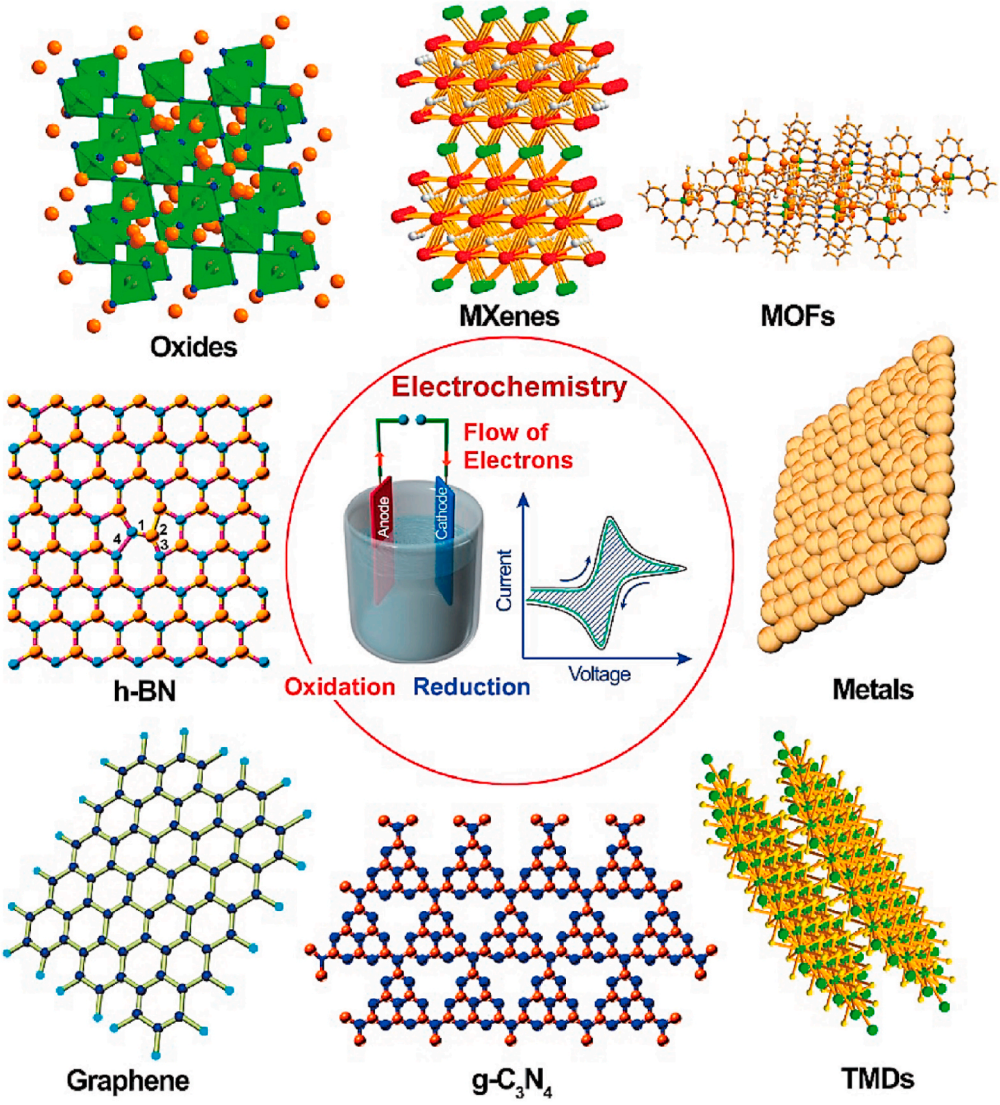

Fig. 3. Schematic of different two-dimensional nanomaterials used in electrochemistry. Adapted from Ref. [35] Copyright 2017, The Chemical Society of Japan.

[79,82,83]. The obstacle to its widespread application has arisen because of the high cost of noble metal-based OER catalysts (that is, Ir/IrO_2 and Ru/RuO_2) [82–86]. Generally, OER activity is most influenced by the active sites accessible to the electrolyte and the transition metal elements oxidation state [85]. For instance, the fabrication of Co_3O_4 nanosheets reported by Du et al. [83] displays eminent OER activity along with higher stability as a result of abundant exposed active sites. Additionally, the 2D $FeSe_2$ nanoplatelets demonstrated significant catalytic behavior and stability for the OER, as shown in Fig. 4a and b [84]. The exceptional electrocatalytic efficiency of $FeSe_2$ nanoplatelets is attributed to the exposed active sites associated with the 2D nanostructures, which is promising for enhancing the kinetics of water oxidation (e.g., Tafel slope: 48.1 mV/dec; Overpotential: 2.2 times superior compared to commercial RuO_2 at 500 mV; steady-state current densities that remain unaffected after 70 h). The efficiency of 2D copper oxide (CuO) as an OER catalyst was investigated by Pawar et al. [85]. The optimized two-dimensional CuO nanosheet electrode in a 1 M KOH electrolyte solution exhibited a minimal overpotential of 250 mV with a Tafel Tafel slope of 59 mV/dec. Discussions in the literature on defect engineering in 2D oxides are limited, as the field is still in its early stages concerning 2D OER catalysts.

Tripkovic et al. explored the OER activities of Co- and Ni-layered oxyhydroxides (oxhys) incorporating various heteroatom dopants for 25 elements [90]. The results from these experiments revealed a more favorable response to Ni doping compared to Co oxides. Noble and transition metals (first row) have emerged as stable dopants. Additionally, promising OER catalysts have been identified as Ni-oxyhydroxides with Rh doping [90]. Thin sheets of MoS_2 and TaS_2, exfoliated chemically into 2D structures, have recently been investigated for OER catalysis under acidic conditions, encompassing both their 1T and 2H polymorphs [91]. Interestingly, the OER activity decreased in the following sequence: 1T-MoS_2, 1T-TaS_2, 2H-MoS_2, and 2H-TaS_2. The majority of catalytic activity is believed to occur at edge locations rather than at the basal planes. The 1T polymorph exhibited greater activity than its 2H counterpart, as supported by both the experimental and theoretical findings. Hence, enhancing its OER activity through defect engineering, particularly by incorporating the edge-rich and 1T phases of TMDs, is a prudent approach. In an alkaline solution, Weng et al. [85] showed that layered $Na_{1-x}Ni_yFe_{1-y}O_2$ double oxide electrocatalysts exhibit high ORR activity, achieving an overpotential of 0.26 V vs. RHE at 10 mA/cm^2 current density of 10 mA/cm2 and a Tafel slope of 44 mV dec-1. To enhance ORR activity, two-dimensional $CoSe_x$ nanocrystalline dotted porous CoCo LDH nanosheets (Co-Se NSs) were designed [87] with enhanced vacancies and a highly oxidized state of Co (Fig. 4c and d). This structural modification resulted in a higher density of ORR active sites, improved electrical conductivity, and a larger available

Table 1
Oxygen evolution reaction.

Electrocatalyst	Synthesis	Engineering Strategies	Electrolyte	Catalyst Loading (mg cm^2)	Onset Potential	Over Potential (V)	Tafel Slope (mV dec^1)	*n*	Current Density (mA cm^{-2})	Comments		Ref.
										Advantages	Disadvantages	
$Pt/Ti_{0.7}Mo_{0.3}O_2$	Microwave Assisted Polyol Synthesis	Metal Doping	0.5 M H_2SO_4	0.02	0.9 V Vs. NHE	–	–		4.5	Enhanced electron transfer to Pt; high-performance catalyst	May increase cost due to metal doping	[41]
N doping carbon nanosheets	Hard Template Method	Non Metal Doping	0.1 M KOH	0.204	0.076 V Vs. RHE	–	–	3.9–4.0	–	Metal-free; efficient for oxygen reduction	Potential stability issues due to non-metal doping	[42]
Pt/WO3	Precursor Phase Synthesis	Vacancy Defect	0.1 M $HClO_4$	6.32	0.85 V Vs. NHE	–	–	3.7	–	Improved active sites availability	Potential reduction in structural integrity due to vacancy defects	[43]
MoS_2/NG	Physical Mixing Method	Heteroatom Doping	0.1 M KOH		−0.12 V Vs. SCE	–	–	3.75–3.90	–	Efficient electrocatalyst for oxygen reduction	Complex synthesis process	[44]
Au $NiCoFe_7S_8$	Ion Diffusion Method	Metal Doping	1 M KOH	~0.255	–	0.243	43	4	–	Exceptionally high oxygen evolution reaction activity	Higher cost due to metal doping	[45]
Pd@PANI	Solvothermal Method	Interface Engineering	0.1 M KOH	–	1.02 V Vs. RHE		56.8	3.89	–	Enhanced alkaline oxygen reduction reaction	Complex fabrication process	[46]
Co_3O_4-N-doped graphene	Hydrothermal Method	Non Metal Doping	1.0 M KOH	1.0	~1.49 V Vs. RHE	0.31 V	67	3.9	10	Hydrothermal method can yield high-quality materials, non-metal doping could improve performance	High catalyst loading and Tafel slope, indicating potential efficiency issues	[47]
N-doped graphene $NiCo_2O_4$	Heterogeneous Reaction Method	Non Metal Doping	0.1 M KOH	2.0	~1.54 V Vs. RHE	1.69 V	156	–	10	Heterogeneous reaction method could yield a highly active material, non-metal doping is innovative	Very high catalyst loading, over potential, and Tafel slope, indicating significant challenges in efficiency and kinetics	[48]
g-C_3N_4-graphene	Physical mixing	Interface Engineering	0.1 M KOH	1.0	~1.61 V Vs. RHE	1.65 V	128	–	10	Physical mixing might offer structural advantages, interface engineering could enhance electron transfer	High catalyst loading, over potential, and Tafel slope, suggesting less efficient operation	[49]
g-C_3N_4-NS–CNT	Sonication/exfoliation	Interface Engineering	0.1 M KOH	0.2	~1.53 V Vs. RHE	1.60 V	83	–	10	Low catalyst loading, sonication/exfoliation technique may offer unique structural benefits	High over potential and Tafel slope, indicating possible efficiency issues	[50]
NG-CNT	Layer by layer assembly	Heteroatom Doping	0.1 M KOH	~1.75	~1.54 V Vs. RHE	1.70 V	141	–	10	Layer by layer assembly could yield a structurally optimized material, dual doping might enhance activity	Very high catalyst loading, over potential, and Tafel slope, suggesting efficiency issues	[51]
NiFeLa-LDH/v-MXene/NF	Electrodeposition	Heteroatom Doping	1.0 M KOH	3.85	171 mV Vs. RHE	255 mV	40	4	500	Electrodeposition might provide precise material control, la-doping can be beneficial for catalysis	Extremely high catalyst loading, over potential, and Tafel slope, indicating major efficiency challenges	[52]
CoSe@NiFe-LDH/NF	Hydrothermal-selenization-hydrothermal method	Heteroatom Doping	1.0 M KOH	1.5	–	201 mV	39	3	10	Hydrothermal-selenization method may enhance material properties, heteroatom doping could improve activity	High catalyst loading, missing onset potential data, indicating potential limitations in efficiency	[53]
Co/N-CNTs@ $Ti_3C_2T_x$	In-situ growth	Interface Engineering	0.1 M KOH	0.408	1.641 V Vs. RHE	411 mV	79.1	3.8	10	In-situ growth might offer high-quality material synthesis, interface engineering could be advantageous	High over potential and Tafel slope, suggesting challenges in efficiency and kinetics	[54]
NiFe-LDH/Co, N-CNF	Deposition	Heteroatom Doping	0.1 M KOH	0.12	154 V Vs. RHE	312 mV	60	3.89	10	Deposition method could yield high-purity materials, heteroatom doping could enhance catalytic activity	Very high over potential and Tafel slope, low catalyst loading, suggesting significant challenges in operation efficiency	[55]

(*continued on next page*)

Table 1 (*continued*)

Electrocatalyst	Synthesis	Engineering Strategies	Electrolyte	Catalyst Loading (mg cm^2)	Onset Potential	Over Potential (V)	Tafel Slope (mV dec^1)	*n*	Current Density (mA cm^{-2})	Comments		Ref.
										Advantages	Disadvantages	
$Ti_3C_2T_x$-CoBDC	Interdiffusion reaction-assisted process	Interface Engineering	1.0 M KOH	0.21	164 V Vs. RHE	–	48.2	4	10	Interdiffusion reaction-assisted process might offer unique material advantages, interface engineering could improve catalysis	High Tafel slope suggests slower reaction kinetics, missing over potential data	[56]
CoP@3D Ti_3C_2-MXene	Capillary-forced assembling strategy	Interface Engineering	1.0 M KOH	0.2	160 V Vs. RHE	290 mV	51	–	10	Capillary-forced assembling strategy could yield structurally advantageous materials, 3D architecture might enhance electrocatalytic activity	High Tafel slope indicates potential efficiency issues, high over potential	[57]
$CuCo_2O_4$/N-rGO	Solvothermal method	Heteroatom Doping	1.0 M KOH	0.12	41 V Vs. AgCl	0.36 V	62	4	10	Solvothermal method likely provides high-purity materials, heteroatom doping could enhance performance	Relatively high over potential and Tafel slope, suggesting efficiency challenges, onset potential data missing	[58]
Co_3S_4@MoS_2	One Pot /Hydrothermal method	Heteroatom Doping	0.5 M H_2SO_4	0.283	210 mV Vs. RHE	–	88	–	10	One Pot/Hydrothermal method can yield high-quality materials, heteroatom doping might improve catalytic activity	High Tafel slope indicating less efficient kinetics, missing over potential data	[59]

Abbreviations:

Pt = Platinum; HCCs = highly concave cubic (HCC); NG = Nitrogen Doped Graphene; Au = Gold; Pd = Palladium; PANI = Polyaniline.
Pt/NPC = Pt atoms on a Nitrogen Doped Porous Carbon; C_3N_4 = Carbon Nitride; Pt_1 N/BP = Carbon Supported Doped N Triggered Pt SAC.
Ru N/G = Ru on Nitrogen Doped Graphene; $Ru_xFe_ySe_z$ = Ruthenium Based Clusters; CNP = carbon nanoparticle.
N Fe CNT/CNP = Nitrogen-Doped Carbon Nanotube/Nanoparticle Composite; PPCN = Phosphorus-doped carbon nanosheets.
VA NCNTs = Vertically Aligned Nitrogen-Containing Carbon Nanotubes; NS G = N & S co-doped Graphene.
Ru SSC = Single Site Catalyst; Ir N C Single Atom Catalyst = Ir SAC.
(BN GQD/G)B = Boron and Nitrogen-Doped Graphene Quantum Dots/Graphene Hybrid.
N, O VAGNs/CC = Nitrogen Doped, Oxygen Functionalized and Edge/Defect Rich Vertically Aligned Graphene Nanosheets on the Surface of a Carbon Cloth.

Table 2
Oxygen reduction reaction.

Electrocatalyst	Synthesis	Engineering Strategies	Electrolyte	Catalyst Loading (mg cm^2)	Onset Potential	Over Potential (V)	Tafel Slope (mV dec^1)	*n*	Current Density (mA cm^{-2})	Comments		Ref.
										Advantages	Disadvantages	
Pt HCC nano Crystal	Hummers Method	Interface Engineering	0.1 M $HClO_4$	0.046	0.967 V Vs. RHE	–	−120	4.0	–	High activity, durability, and unique hybrid structure	Complex synthesis process; high cost	[60]
Pt_1/NPC	Photochemical Solid Phase Reduction	Metal Doping	0.1 M KOH	0.0152	0.887 V Vs. RHE	0.025	55	~3.95	–	High catalytic efficiency; enhanced bifunctional capabilities	Expensive due to platinum usage; scalability issues	[61]
Au_1N_x single site/ C_3N_4	Amine Induced Reduction	Metal Doping	0.1 M KOH	–	0.76 V Vs. RHE	0.76	74	~3.9	5	Good electrocatalytic performance; efficient bifunctional catalyst	Stability issues; potential high cost of gold	[62]
Pt_1 N/BP	Oil Bath Reflux	Metal Doping	0.1 M $HClO_4$	0.09	0.87 V	2.87	–	4	−600	High performance with significant Tafel slope	High cost; environmental concerns	[63]
Pt_1 N/BP	Oil Bath Reflux	Metal Doping	0.1 M KOH	0.09	–	–	–	4	–	Versatile for different electrolytes	High cost; environmental concerns	[63]
Ru N/G	NH_3 Atmosphere Annealing	Metal Doping	0.1 M $HClO_4$	0.32	0.75 V	+0.89	134	4	3	Enhanced reaction with single-atomic ruthenium sites	Complex synthesis; limited availability	[64]
Se/Ru(Se)/C	Reduction Procedure/ Campbell's Method	Metal Doping	0.1 M H_2SO_4	1.0	0.85 V	–	–	–	320	Promising ruthenium-selenium catalyst	Limited information on long-term stability	[65]
N Fe CNT/CNP	Single Scalable Method	Doping	0.1 M NaOH	0.2	0.87 V	–	80	4	10^{-2}–10^{1}	Stable and active composite electrocatalyst	Scalability and mass production challenges	[66]
VA NCNT/GC	–	Heteroatom Doping	0.1 M KOH	–	0.22V	80	–	4	0.8–1.1	High electrocatalytic activity with nitrogen doping	Limited information on real-world applications	[67]
Ru SSC	Rotary Vacuum	Doping	0.1 M $HClO_4$	0.0025	0.824 V	0.92	54.3	4.0	11.95	Efficient and durable single site catalyst	Complexity in synthesis and higher cost	[68]
Ir SAC	Host–Guest Strategy	Doping	0.1 M $HClO_4$	0.0008	864 mV	0.97	41	4.0	–	High efficiency in oxygen reduction	Expensive and complex to produce	[69]
NS G	Ultrasonic Exfoliation	Defect Engineering	0.1 M KOH	–	0.89 V	–	–	–	–	Multifunctional electrode materials for various applications	Unclear long-term durability	[70]
BN GQD/G	Hydrothermal	Heteroatom Doping	0.1 M KOH	–	–	0.98	–	3.93	−11.1	Efficient electrocatalysts with doped graphene quantum dots	Potential scalability and production challenges	[71]
2D PPCN	Template Method	Heteroatom Doping	0.1 M KOH	1.0	–	0.92	96	3.6		Tunable porosity for oxygen reactions	Limited application data	[72]
B,N carbon	Pyrolysis, Templated	Heteroatom Doping	0.1 M KOH	–	0.98 V V Vs. RHE	–	84	~3.8	−50	Promising metal-free bifunctional electrocatalyst	Stability and long-term performance concerns	[73]
S, N Dual Doped Graphene like Carbon	Pyrolysis	Heteroatom Doping	0.1 M KOH	–	0.97 V V Vs. RHE	0.785	–	3.6–3.9	−4.9 (0.2 V vs RHE)	High efficiency in oxygen reduction	Synthesis complexity and cost	[74]
S, N Dual Doped Graphene like Carbon	Pyrolysis	Heteroatom Doping	0.5 M H_2SO_4	–	0.797 V V Vs. RHE	–	–	3.6–3.9	–	Versatile in different electrolytes	Synthesis complexity and cost	[74]
BCN/KBC	Solvothermal	Interface Engineering	0.1 M KOH	0.226	-	1.01	72.4	4	–	Metal-free electrocatalyst with potential in alkaline medium	Longevity and mass production yet to be established	[75]
MnBN/C 75	Chemical Method	Interface Engineering	0.1 M KOH	0.16	0.9 V V Vs. RHE	–	122	4.0	5.6	Tunable nanocomposite catalyst	Specificity in synthesis method	[76]
Co/N co-doped graphene	Pyrolysis	Phase Engineering	PBS Buffer	0.5	0.15 V Vs. Ag/AgCl	–	66	~3.9	5.2	Suitable for oxygen reduction in microbial fuel cells	Limited broader application	[77]

(*continued on next page*)

Table 2 (*continued*)

Electrocatalyst	Synthesis	Engineering Strategies	Electrolyte	Catalyst Loading (mg cm^{-2})	Onset Potential	Over Potential (V)	Tafel Slope (mV dec^{-1})	*n*	Current Density (mA cm^{-2})	Comments		Ref.
										Advantages	Disadvantages	
$Ru_xFe_ySe_z$	Pyrolysis	Metal Doping	0.5 M H_2SO_4	0.8	0.85 V Vs. NHE	0.40	111	4	−460	Potential application in polymer electrolyte fuel cells	Complexity in synthesis and cost considerations	[78]

Abbreviations:
Pt = Platinum; HCCs = highly concave cubic (HCC); NG = Nitrogen Doped Graphene; Au = Gold; Pd = Palladium; PANI = Polyaniline.
Pt/NPC = Pt atoms on a Nitrogen Doped Porous Carbon; C_3N_4 = Carbon Nitride; Pt_1 N/BP = Carbon Supported Doped N Triggered Pt SAC.
Ru N/G = Ru on Nitrogen Doped Graphene; $Ru_xFe_ySe_z$ = Ruthenium Based Clusters; CNP = carbon nanoparticle.
N Fe CNT/CNP = Nitrogen-Doped Carbon Nanotube/Nanoparticle Composite; PPCN = Phosphorus-doped carbon nanosheets.
VA NCNTs = Vertically Aligned Nitrogen-Containing Carbon Nanotubes; NS G = N & S co-doped Graphene.
Ru SSC = Single Site Catalyst; Ir N C Single Atom Catalyst = Ir SAC.
(BN GQD/G)B = Boron and Nitrogen-Doped Graphene Quantum Dots/Graphene Hybrid.
N, O VAGNs/CC = Nitrogen Doped, Oxygen Functionalized and Edge/Defect Rich Vertically Aligned Graphene Nanosheets on the Surface of a Carbon Cloth.

surface area with porous channels for charge adsorption and transport. An accelerated durability test confirmed the high stability of the $CoSe_x$ nanosheets. Numerous other 2D materials with engineered defects are studied as ORR catalysts, including graphene, TMDs, layered oxides, and LDHs [30,31,88,89,92–94]. Using density functional theory (DFT) calculations, Kong et al. [88] studied the ORR activity of functionalized graphene and found that B-dopants outperformed other dopants and showed enhanced ORR activity (Fig. 4e and f). Additionally, first-principles simulations were employed to analyze the ORR catalytic efficacy of a graphitic carbon nitride (g-CN) monolayer doped with five different transition metal atoms (Pt, Pd, Co, Ni, and Cu) [92]. A study reported in Ref. [89] revealed strong electrocatalytic activity in Ni_3N--loaded benzimidazole covalent organic frameworks for ORR using an overpotential (400 mV) and current density (10 mA/cm^2), as shown in Fig. 4g–i. For the ORR, the covalent organic framework served as a metal-free-standing scaffold. Such loaded covalent organic frameworks exhibited exceptional activity in an alkaline solution with a record-low overpotential (230 mV) at 10 mA/cm^2. The interaction between the p-conjugated covalent organic framework and conducting Ni_3N nanosheet contributed to this performance. Ren et al. [93] showed that 2D black phosphorus (BP) nanosheets exhibited better electrochemical activity than their bulk counterparts. Electrochemical experiments revealed an OER onset of 1.45 V and 88 mV/dec Tafel slope. The exfoliated 2D BP displayed potential as an efficient nanostructure for effective electrocatalysis, offering exceptional electrochemical ORR efficacy and strong long-term stability. The ORR activity of black phosphorus also showed an enhanced tendency as a function of increasing thickness. The specific surface area and number of active regions can be amplified by decreasing the number of layers in black phosphorous, which is thought to be a viable method for achieving outstanding electrochemical ORR efficacy [93].

2.1.2. Nonmetal doping

The literature shows that incorporating nonmetallic elements as dopants into MoS_2 nanosheets leads to improved ORR activity owing to the transformed electronic structures caused by the doped atoms. Additionally, integrating heteroatoms (P, O, and N, etc.) into MoS_2 reduces the bandgap energy, increases the conductivity by altering the electronic structure, and ultimately offers numerous catalytically active sites. Huang et al. reported MoS_2 nanosheets with enhanced edge defects by employing g-C_3N_4 as a self-sacrificial species. The nanosheets were obtained by a hydrothermal approach followed by heat treatment. Oxygen was incorporated into the MoS_2 sheet network using H_2O_2 (Fig. 5a). The sample exhibited advanced catalytic activity and showed a significant half-wave electric response (0.80 V) in addition to a primary potential (0.94 V) in 0.1 M KOH (Fig. 5b). Remarkably, the ORR selectivity of O-MoS_2 improved from the $2e^-$ route to the $4e^-$ path, emerged because of highly electronegative O atom polarizing the neighboring unsaturated Mo atoms (Fig. 5c). Moreover, edge Mo atoms produced a supplementary positive charge that was favorably adsorbed through O molecules, consequently accelerating the ORR [95]. Using DFT measurements, Xie et al. compared bare 2H-MoS_2 nanosheets (with a 1.75 eV bandgap energy) with O-bound MoS_2 nanosheets (~1.30 eV narrow bandgap energy), as displayed in Fig. 5d. This indicates that the synergy between the MoS_2 nanosheets and oxygen produces additional carriers and accelerates the material intrinsic conductivity [96], thereby promoting higher HER and ORR progress.

Furthermore, introducing low-electronegativity atoms (i.e., P and N) into MoS_2 can significantly improve the ORR activity, but there are still known challenges in explaining such sophisticated progress. The fabrication of P-doped MoS_2 nanosheets reported by Huang et al. showed a higher ORR progress. The improved ORR performance was defined by boundary molecular orbital theory (Fig. 6a and b) [97]. In semiconductors, elevating the energy level of the frontier orbital proves advantageous for electron donation. This facilitates easier oxygen adsorption and the formation of the intermediate product OH−, thereby

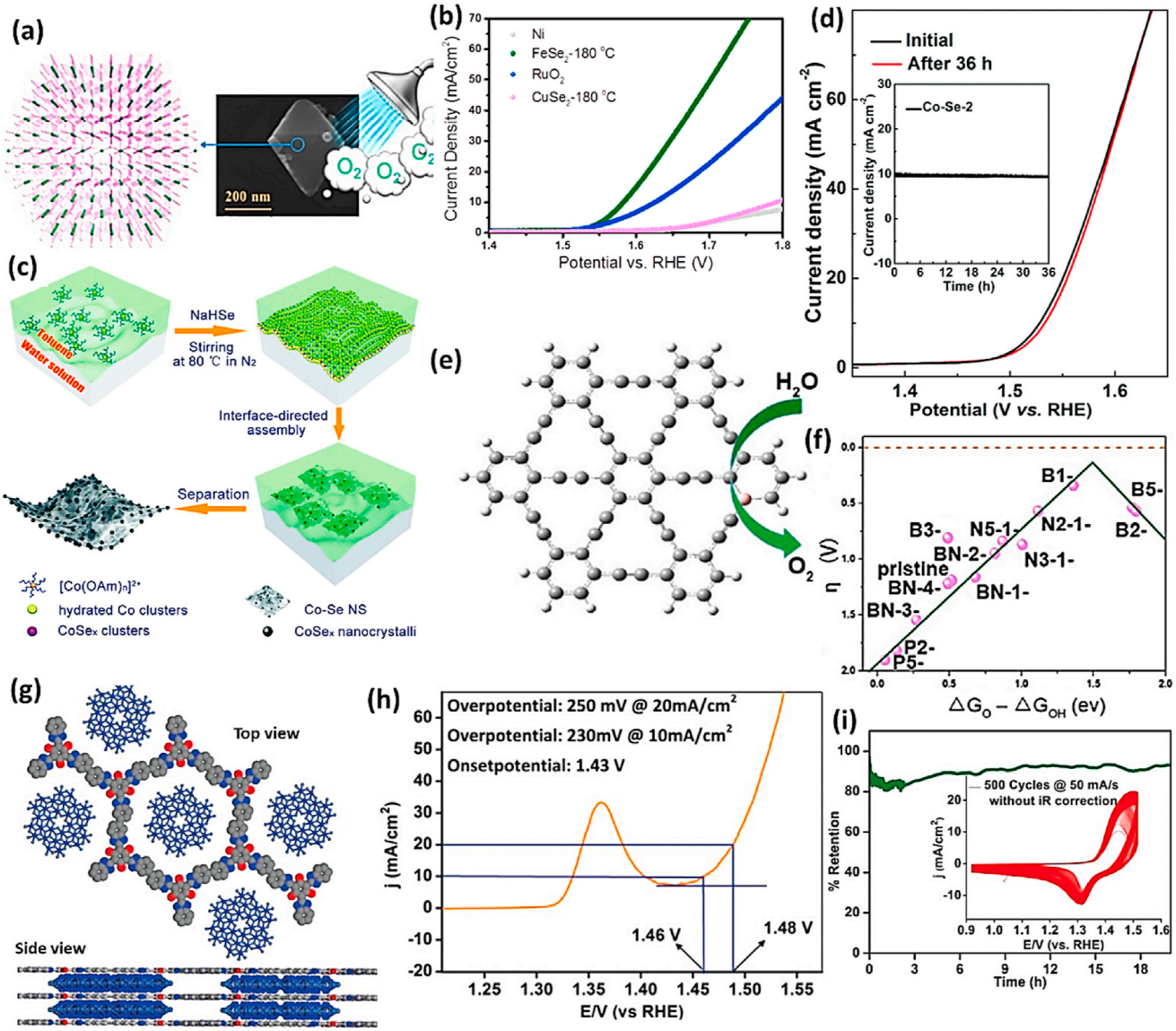

Fig. 4. (a) Illustration depicting OER activity (b) Linear sweep voltammetry (LSV) curves of $FeSe_2$ in 1 M KOH nanoplatelets. Adapted from Ref. [84] Copyright 2017, Elsevier B.V. (c) Graphical Illustration of the synthesis, and (d) LSV curves of $CoSe_x$ nanocrystalline speckled CoCo hydroxide bilayer nanosheets in 1.0 M KOH. Adapted from Ref. [87] Copyright 2017, The Royal Society of Chemistry. (e) Reaction scheme for B-doped graphene. (f) Volcano plot showing the overpotential of different ORR-doped graphene, denoted as FX- or FX-Y-, with "F," "X," and "Y" representing various heteroatoms. Adapted from Ref. [88] copyright 2017 Elsevier B. V. (g) Atomistic description of the material structure. (h) Linear voltammogram curves of IISERP-COF3 (a conjugated benzimidazole-based framework) loaded with Ni3N in 1 M KOH. (i) Chronoamperometric graph demonstrating the stability of current outputs (over 20 h). The inset shows that the Ni(III)–Ni(IV) redox couple remains stable over 500 CV cycles. A minor hump (~1.36 V) corresponds to the Ni(II)–Ni(III) redox couple. The reason for this is less obvious is due to high scan rate. Adapted from Ref. [89] Copyright 2016, John Wiley & Sons, Ltd.

accelerating the overall reaction rate [98].

Zhang et al. conducted calculations on the overpotential of single-layer MoS_2 doped with N- or P- during the ORR in acidic conditions [100]. Their findings indicate that the substitution of S atoms with P or N atoms in the MoS_2 single layer introduces a high spin density into the basal plane of MoS_2. This enhancement improves its capability to activate O_2, making the ORR step more likely to proceed through the more efficient $4e^-$ pathway. Significantly, the ORR progress of P-doped MoS_2 is insignificant than N-doped MoS_2 because of the exceptionally high adsorption sites for the intermediary product (for P-doped MoS_2) [5,6, 101–103]. However, such findings do not correspond to their P-doped counterparts and have no practical outcomes.

An investigation of the ORR mechanism, along with the detection of substantial active sites in P-doped MoS_2 (monolayer), was conducted by Liu et al. using DFT calculations. In their study, MoS_2 maintained specific structures, whereas P dopants were introduced in alkaline media (Fig. 6c). The results demonstrate that superior progress was achieved with double P-doped MoS_2 (greater P content) compared to single P-doped MoS_2. Furthermore, the enhanced catalytic activity of the dual P-doped catalyst can be attributed to the S_2 atoms neighboring two P-atoms, resulting in reduced S_2 site charge, which in turn creates a strong hydrogen bond that enhances the adsorption of H_2O and OH- groups. Notably, the doubly doped catalyst exhibited favorable adsorption energy for intermediary products compared to the single P-doped catalyst (Fig. 6d). The optimal P-doping content in the catalyst, as determined through DFT calculations, was found to be 5.5 % for the ORR experiment, which closely aligns with the observed experimental value (4.7 %). Consequently, Liu et al.'s study provides a plausible explanation for the catalytic effect of P, resolving a topic that has puzzled researchers to a great extent [99].

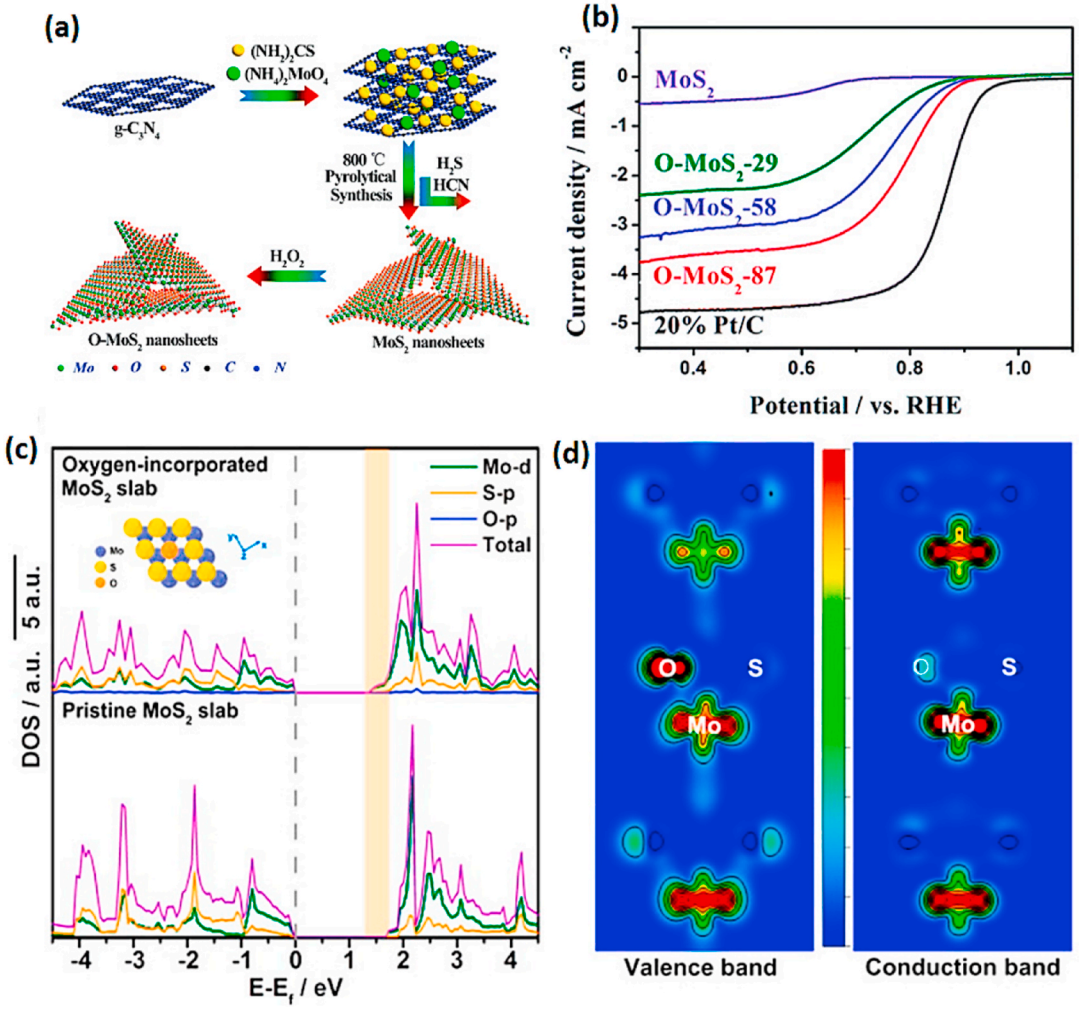

Fig. 5. (a) Design of the synthetic procedure for introducing oxygen into MoS_2 nanosheets. (b) Results depicting ORR activity for O-MoS_2, pure MoS_2 nanosheets, and 20 % Pt/C in O-saturated 0.1 M KOH. Adapted from Ref. [95] Copyright 2015, The Royal Society of Chemistry. (c) The measured density of states for the pristine 2H-MoS_2 slab (bottom) and oxygen-incorporated MoS_2 slab (top). Orange shading is a clear indication of a decrease in the bandgap energy after the introduction of oxygen. (d) Visualization of the charge-density distribution near the oxygen atom for the VB and CB (left and right) in the O-incorporated MoS_2 nanosheets. Adapted from Ref. [96] Copyright 2013, American Chemical Society.

2.1.3. Metal doping

To enhance the ORR activity, metallic doping can be introduced into the MoS_2 structure in addition to nonmetallic components. Incorporating Co, Cu, and other transition metal dopants into MoS_2 (creating S-vacancies) improves the ORR activity. Xiao et al. conducted theoretical investigations into the ORR activities of Co/Ni-doped ultrathin MoS_2. In the Co/Ni-doped MoS_2, the Co/MoS_2 site resembles the FeN_4 active site in the M-N-C catalyst, whereas the Ni/MoS_2 site resembles the CoN_4 active site. Consequently, compared to bare MoS_2, Co/Ni-doped MoS_2 (monolayer) exhibited improved ORR performance [104]. Furthermore, Urbanova et al. incorporated metal components (i.e., Mn, V, Ti, and Fe) into MoS_2 and observed a promising enhancement in ORR response (Fig. 7a and b) [105,106]. Although plentiful research has considered the inclusion of metal dopants in MoS_2 structures, the choice of specific metal types remains a critical parameter.

DFT calculations were adopted by Wang et al. to explore the ORR development for various transition-metal-doped MoS_2 (monolayer) configurations in this context. Outcomes specify that the introduction of transition metal atoms replaces the S-vacancies in MoS_2, significantly altering its electronic structure. Cu-doped MoS_2 showed the highest theoretical binding strength with an ORR intermediate, aligning with the better ORR performance observed in its counterparts, as shown in Fig. 7c and d [107]. These findings contribute to ongoing efforts in the growth of metal-doped MoS_2 materials for ORR catalysts. Because the S-bonds in metals are considered reactive sites in metal-doped TMDs and lead to increased metal atom density on the MoS_2 surface and minimizing metal accumulation during heat treatment becomes a crucial parameter for enhancing catalyst reactivity. However, achieving optimal metal-doping control on a relatively small MoS_2 surface remains a challenge. Addressing these issues is essential for improving the ORR progress of the metal-doped MoS_2.

3. Hydrogen evolution reaction

Recently, electrocatalysts based on 2D-TMDs, for example, WS_2 [108], NbS_2 [109,110], $MoSe_2$ [111,112], and MoS_2 [113,114], etc., proved as favorable applicants to encounter shortcomings of noble metals or associated compounds. Utilizing new techniques and two-dimensional TMDs, owing to their novel characteristics enhances HER activity. These methods can be separated into five assemblies: **1)** Creation of extra active sites, **2)** Doping of heteroatoms, **3)** Creation of heterostructures, **4)** Phase engineering, and **5)** Synergistic modulation. This section summarizes recent achievements in improving catalytic performance by utilizing these strategies. Table 3 showcases the recent advancements in HER.

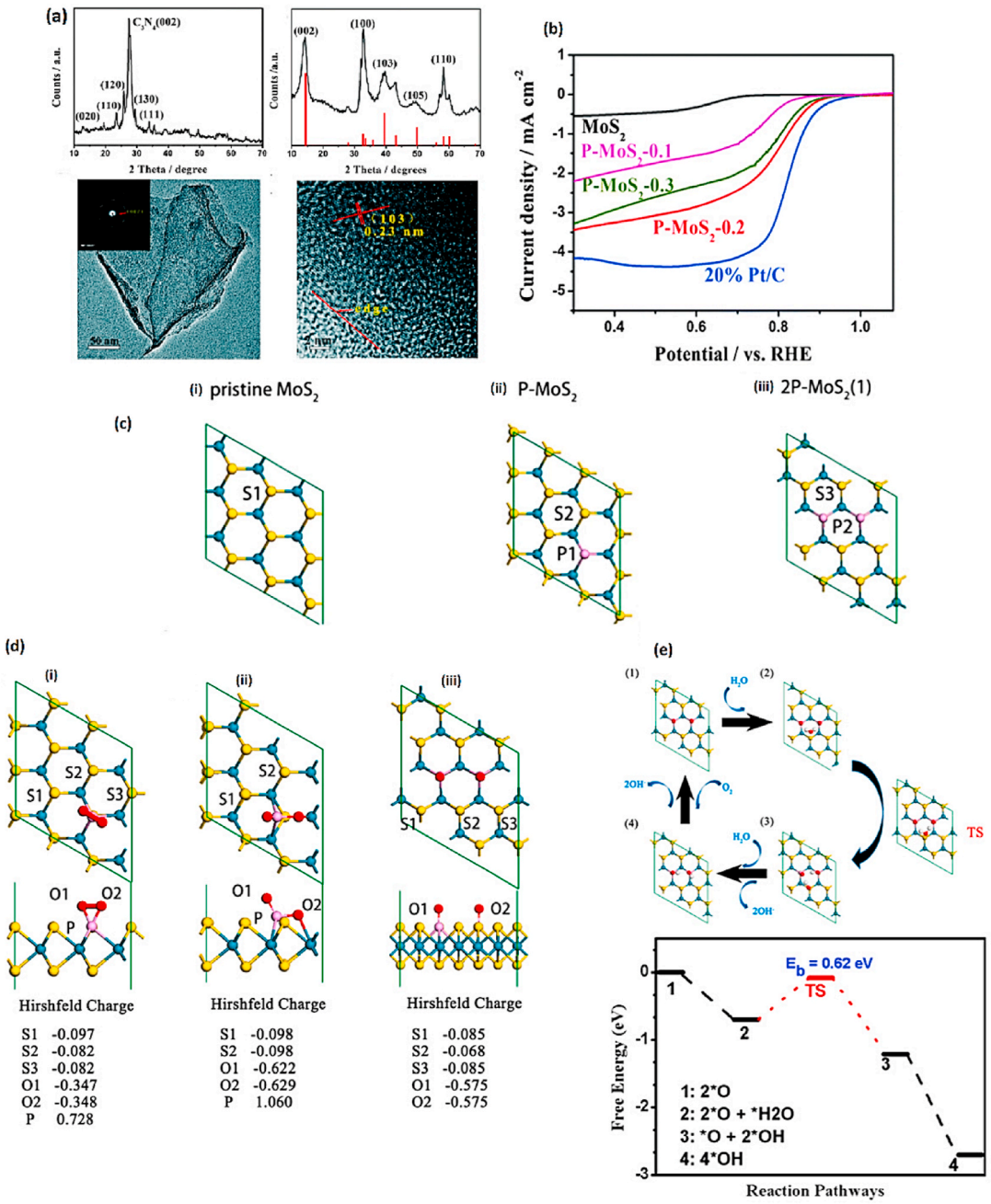

Fig. 6. (a) XRD patterns of ultrathin P-MoS_2 nanosheets and MoO_3/g-C_3N_4 intermediate, along with TEM and HRTEM images of P-MoS_2 nanosheets. **(b)** Results for ORR electrocatalysis of the P-MoS_2-0.1 to −0.3, MoS_2, and Pt/C (20 %) catalysts. Adapted from Ref. [97] Copyright 2015, The Royal Society of Chemistry. **(c)** Representation of the optimized structure of the MoS_2 nanosheets (top view) showing **(i)** pristine, **(ii)** single P-doped, and **(iii)** double P-doped configurations. **(d)** Optimized adsorption patterns (top and side views) for **(i)** O_2-adsorbed P-MoS_2, **(ii)** O_2-adsorbed single P-MoS_2, and **(iii)** 2O-adsorbed double 2P-MoS_2 (Hirshfeld charge values are also provided for the corresponding atoms). **(e)** Optimized structure patterns of the product (1–4), intermediates, reactant, and consistent reaction mechanisms for the ORR on a 2P-MoS_2 sheet (alkaline media). Adapted from Ref. [99] Copyright 2028 Springer Nature Limited.

3.1. Strategies

3.1.1. Defect engineering

Introducing defects into 2D structures in the HER alters their electronic and catalytic properties, leading to improved stability and activity. Significantly, the introduction of defects can be done employing numerous approaches including ion irradiation, chemical doping, or electrochemical treatment. By tuning the defect density and type, the efficiency of the HER process can be optimized. Moreover, 2D materials offer unique advantages for defect engineering, such as high surface area, facile integration with other materials, and the capability to control defect locations and densities. Therefore, defect engineering in 2D materials is a favorable route en route for boosting the progress of HER and other energy-related applications.

3.1.1.1. Size control and edge enrichment. The catalytic response might be importantly enhanced by dropping lateral size of monolayers, which can significantly increase the edge site density. Lin et al. [56] described sulfur-depleted monolayered MoS_2 nanocrystals as a photocatalyst for dye-degradation and the HER, as illustrated in Fig. 8a. The fundamental pathways during the growth of Mo-S monolayers and their possible electronic structure were disclosed. Lin et al. also described a method for

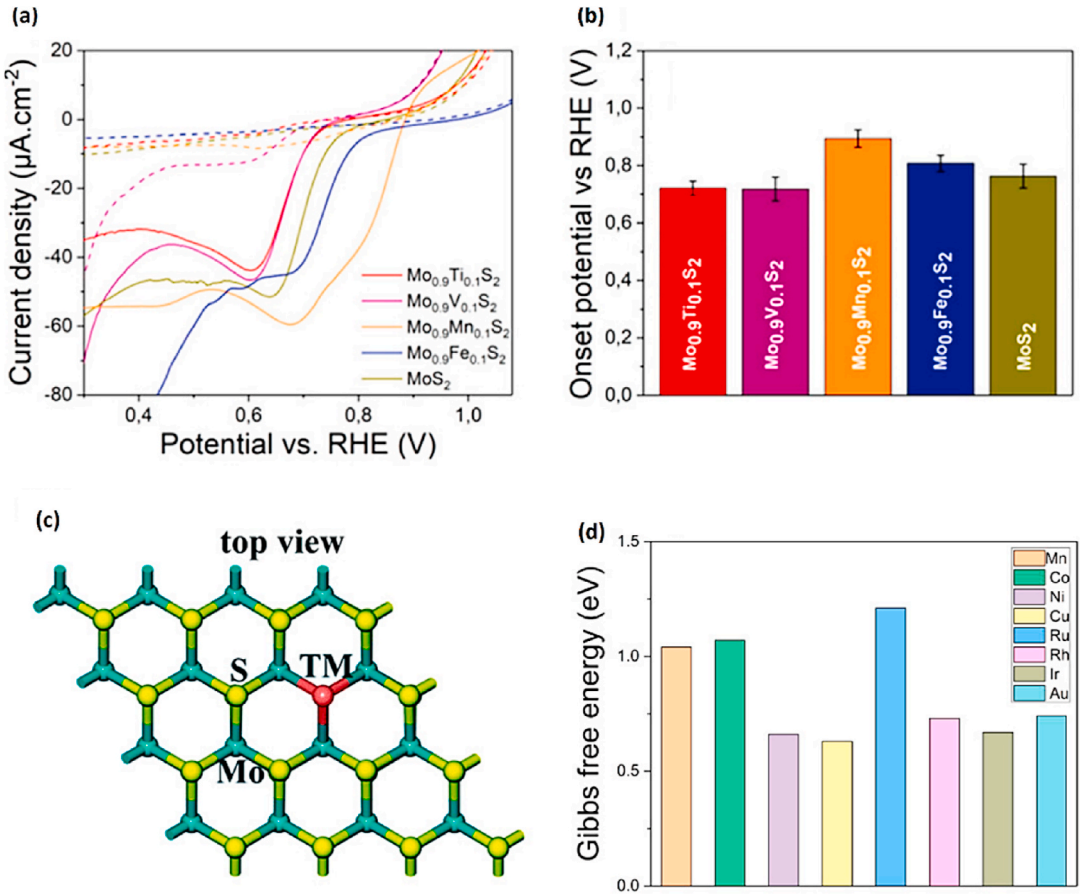

Fig. 7. (a) Typical LSV curves for ORR, **(b)** Consistent standards of onset potentials. Adapted from Ref. [105] Copyright 2020, American Chemical Society. **(c)** Representation of transition atom implants in S-vacancy, **(d)** Gibbs free energy towards ORR on many transitions metal implanted MoS_2 single layers through OOH association pathway Adapted from Ref. [107] Copyright 2017, The Royal Society of Chemistry.

creating monolayer 1H MoS_2 nanocrystals (lateral size of ~ 12.5 nm), as shown in Fig. 8b and c [137]. High yield (31 wt%), high crystallinity, and an average width of 12.9 nm (Fig. 8d) were obtained in monolayered 2H-MoS_2 nanocrystals (over 90 %) having a thickness of 0.9 nm, which is typical of monolayers. In Fig. 8e, the FFT (Fast Fourier Transform) pattern reveals the formation of an underlying 2H crystal structure. Furthermore, theoretical simulation revealed that prepared nanocrystals also possess a metallic border layer, which encloses the semiconducting core, resulting in improved charge transfer at the catalytic sites (Fig. 8f and g). Fig. 8h Moreover, the super electrochemical reaction of monolayered MoS_2 nanocrystals with reduced sulfur contents is shown in Fig. 8h For [137]. Quantitatively, the onset overpotential for the proposed nanocrystals (using a glassy carbon electrode) ranged from 120 to 140 mV, whereas the Tafel slope (51 mV dec^{-1}), illustrated in Fig. 8i and j. This signifies an improvement over the 1H MoS_2 monolayer (using an Au foil electrode) [138] and alike with 1T WS_2 monolayer nanosheet (with similar glassy carbon electrode) [139]. Additionally, the density of catalytically active sites may increase when pores grow within larger monolayers. Likewise, the preparation of 1H monolayer MoS_2 triangles via the CVD approach was elucidated by Ajayan and co-workers [140]. The size of these 1H monolayers was up to 100 μm, they were well crystalline and were also determined to be approximately inactive for HER up to 500 mV potential and 342 mV dec^{-1} Tafel slope [140]. These prepared materials were activated for the HER by producing O_2 plasma pores, which resulted in 400 mV potential and 162–171 mV dec^{-1} Tafel slope. Inside edges of the newly proposed structure included S and Mo terminated compositions. Annealing monolayer MoS_2 under H_2 is an alternative method to create edges/pores inside monolayers. For these edge-rich monolayers, a 300 mV potential and Tafel slope (117 mV dec^{-1}) were acquired. Reducing the starting crystallite size (Range: 100–200 nm) enhances the HER performance, with an onset overpotential (120 mV) and a Tafel slope (50 mV dec^{-1}) [141]. Li et al. also developed O_2-plasma treated TaS_2 nanosheets to create pores within their interiors [118]. Chemical exfoliation was first used to create highly crystallized TaS_2 nanosheets that were approximately 15 m wide and 1–3 layers thick [118]. After the introduction of pores, both the onset overpotential (310 mV–225 mV) and Tafsel slope (215 mV dec^{-1} to 125–142 mV dec^{-1}) were reduced [118]. Additionally, for $MoSe_2$, the oxidation of H_2O_2 using the standard liquid exfoliation method can be adapted to incorporate chemically assisted pores [142,143]. The technique produced high-density pores by oxidizing and etching thin exfoliated $MoSe_2$ nanosheets. These pores reduced the onset overpotential from 220 mV to 75 mV, while the Tafel slope measurements did not change (80 mV dec^{-1}) [143]. Nonetheless, superior HER progress was achieved for smaller lateral structures, even for multilayered systems (partial 1T phase). Edge creation and manufacturing of monolayered nanocrystals with slight lateral size (5–10 nm) are relatively advantageous approaches [144]. With recent progress in synthesis strategies [137,144,145], producing mono-layered TMDs nanocrystals is a promising approach for achieving the best HER response. As discussed above, phase engineering can enable effective size control and edge modification, although the strength of 1T/1T′ TMDs must be appropriately addressed.

Numerous determinations have been devoted to producing enhanced HER catalysts by means of defect engineering in TMDs, as edge regions can be considered additional defect sites caused by unsaturated sulfur atoms [146–148].In particular, a widely used strategy involves exposing new edges to create more active sites [148,149]. For instance, Xie et al.

Table 3
Hydrogen evolution reaction.

Electrocatalyst	Synthesis Method	Engineering Strategies	Electrolyte	Catalyst Loading (mg cm^2)	Onset Potential (mV)	Over Potential (mV@10 mA cm^2) (Unless Mentioned)	Tafel Slope (mV dec^1)	Diffusion Limited Current Density (mA cm^{-2})	Comment		Ref.
									Advantages	Disadvantages	
2D Porous MoP/Mo_2N	Polyethylene Glycol (Peg) Mediated Assembly Route	Phase Engineering	1 M KOH	–	–	89	78	>190	High efficiency; excellent pH universality	Complexity in synthesis	[115]
Co CoO/Ti_3C_2 MXene	Chemical Etching Method	Heterostructure Engineering	1 M KOH	2	–	8	47	50	Dual-active heterojunction with high performance	Possible scalability issues	[116]
MoS_2	Physical Etching Method	Defects (S-Vacancies)	0.5 M H_2SO_4	0.28	–	160	46	–	Highly active with lattice defects	Stability concerns in long-term operation	[117]
TaS_2	Chemical Etching Method	Edge Defects (Defective atomic Site)	0.5 M H_2SO_4	0.24	–	564	135	–	Atomic-sized pores enhance electrocatalysis	Atomic-sized pores enhance electrocatalysis	[118]
WSe_2	Solvothermal Method	Improved Edge Sites	0.5 M H_2SO_4	–	150	–	78	18.2	Stable and efficient for hydrogen evolution	Limited scalability	[119]
η MoC	Thermal Treatment Method	Doping	0.5 M H_2SO_4 1 M KOH	0.3	−28 −38	122 119	59 39	–	High activity with unconventional phases	Complexity in controlling phase composition	[120]
Mo_2N-Mo_2C/rGO	Chemical Etching Method	Heterojunctions/In Situ Catalytic Etching Strategy	0.5 M H_2SO_4 1 M KOH	0.337	11 18	157 154	55 68	6.2 × 10-2 4.97 × 10-1	Efficient HER with holey graphene oxide coupling	Requires precise synthesis control	[121]
DR-MoN	Salt Template Synthesis	Defect Engineering	0.5 M H_2SO_4 1 M KOH	0.285	10 –	125 139	51.15 67.82	15	Boosted HER activity due to defect-rich structure	Complexity in salt template synthesis	[122]
WS_2/CoS_2/CC	Facile Fabrication Process	Interface Engineering	0.5 M H_2SO_4, 1.0 M PBS 1.0 M KOH	2.0	–	146 175 122	64	–	Efficient at all pH values; rational heterostructure construction	Stability in long-term application	[123]
CeO_2/WS_2	SPSP	Interface Engineering (Oxygen Vacancies)	0.5 M H_2SO_4	4.5	–	128	60	–	Enhanced catalytic activity and stability	High synthesis complexity	[124]
WS_2/WSe_2	Solvothermal Treatment	Heterojunction Engineering	0.5 M H_2SO_4	5	–	121	74.08	=	Boosted HER with heterostructured catalyst	Detailed synthesis control required	[125]
MXene@Pt/SWCNTs	SPS	Heterostructure Engineering	0.5 M H_2SO_4	–	–	−62	419	–	Ultrastable nanocatalysts; high HER efficiency	High cost due to platinum usage	[126]
N Mo_2C	CVD Method	Nonmetal Doping	0.5 M H_2SO_4	0.357	−48.3	99	44.5	0.1	Efficient due to exposed active sites from N-doping	Complexity in CVD synthesis	[127]
Partially crystallized 1T $MoSe_2$	Hydrothermal Synthesis	Phase Engineering	0.5 M H_2SO_4	0.14	–	152	52	–	Enhanced HER from phase engineering	Potential challenges in hydrothermal synthesis	[128]
Ru/MoO_{2-x}	Hydrothermal Process	Phase Engineering*	1 M KOH	5	–	29	22	–	Low overpotential and high activity	Ru incorporation increases complexity and cost	[129]
Co_3S_4	Physical Etching Method	Defect Engineering	1.0 M KOH	0.28	18	63	58	–	High activity with sulfur defects	Long-term stability needs verification	[130]
N rich Mo_5N_6	Growth Method	Phase Engineering	1.0 M KOH	0.4	–	94	66	–	Efficient in seawater splitting; nitrogen-rich for enhanced activity	Limited information on real-world applications	[131]
Ru/C MoO_2	SPR Strategy	Nonmetal Doping	0.5 M H_2SO_4, 1 M PBS	0.28	–	36 46	32 69	5.11	High efficiency with carbon doping	Complexity in synthesis with SPR strategy	[132]
Ni Co A (A = P, Se, O)	Chemical Etching Method	Interface Engineering	1.0 M KOH	1.0	–	150 85 260	57 122 127	–	Dual tuning for enhanced HER	Engineering adds to synthesis complexity	[133]
WS_2–CoS_2 @CP	CVD Method	Interface Engineering	0.5 M H_2SO_4		550	45 mV @ 100 mA cm^2	270	440	Synergistic effect in heterostructure for HER	High overpotential and complexity in CVD synthesis	[134]
P MoS_2	Exfoliation Method	Heteroatom Doping	0.5 M H_2SO_4	0.28	30	65 mV @ 10 mA cm^2	48	–	Enhanced activity from heteroatom doping	Stability and scalability concerns	[135]
Dual native vacancy $MoSe_2$	CVD Method	Defect Engineering	0.5 M H_2SO_4	–	–	126 mV @ 100 mA cm^2	38	–	High-efficiency from dual-native vacancy activation	Complex CVD synthesis process	[136]

Abbreviations: Reduced Graphene Oxide = rGO; Defect-Rich = DR; Single Walled Carbon Nanotubes = SWCNTs; Chemical Vapor Deposition = CVD; Solid Phase Sulfurization Process = SPSP; Solution Processing Strategy = SPS; Solid Phase Reaction = SPR; *One Stone "Two Birds" Strategy.

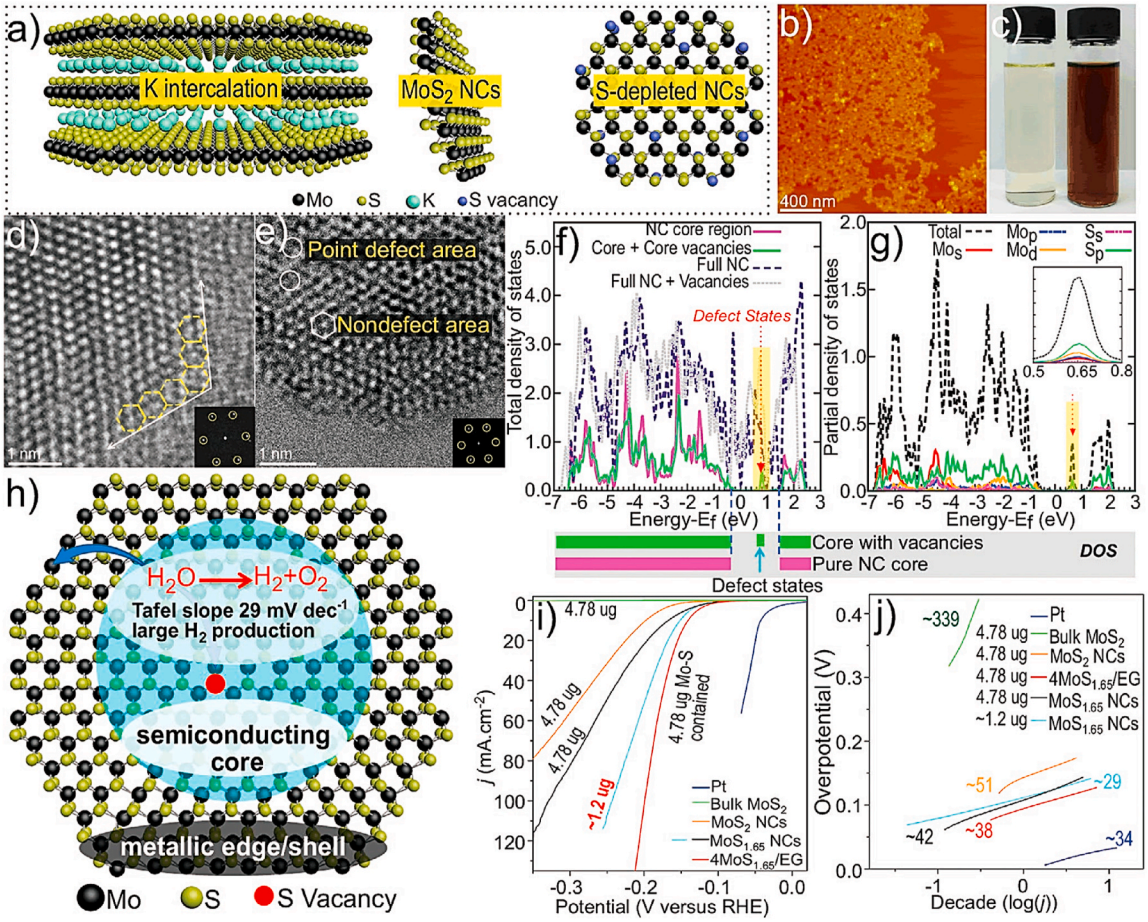

Fig. 8. (a) Preparation of monolayered MoS_2 nanocrystals. Adapted from Ref. [145] Copyright 2017, Elsevier B.V. **(b)** AFM image of the prepared material. **(c)** Optical photograph of monolayer Mo-S nanocrystals before (transparent located on the left) after S-depletion (black, placed on the right). TEM photographs of Mo-S nanocrystals: **(d)** Before S-depletion and **(e)** After S-depletion (related FFT patterns are shown in the inset). **(f)** The calculated density of states for MoS_2 in entire nanocrystal, core, and edge regions. **(g)** Total density of states decomposition of MoS_2 in the core using S-vacancies (S depletion) and edge sites into density of states of the Mo and S orbitals. **(h)** Visualization of metallic edge, near-edge sections, and semiconducting core of MoS_2 nanocrystals. **(i)** Polarization curves and **(j)** Tafel plots in 0.5 m H_2SO_4 for different catalysts. Adapted from Ref. [137] Copyright 2016, American Chemical Society.

[148] described the formation of a two-dimensional MoS_2 nanowall catalyst with a unique structural arrangement that emphasized edge site exposure. This synthesized nanowall catalyst exhibited exceptional activity, with 85 mV potential, 310.6 mA/cm^2 catalytic current density at 300 mV overpotential, and the need for a very low overpotential (95 mV) to initiate a catalytic current of 10 mA/cm^2 (Fig. 9a and b). Vertical MoS_2 nanosheets with edge defects produced through a stepped surface structure are excellent HER electrocatalysts (Fig. 9c). This electrocatalyst exhibits higher stability, an exchange current density of 0.2 mA/cm^2, and 104 mV overpotential at 10 mA/cm^2 [149]. Strategically exposing more catalytically active edges can increase the MoS_2 activity; however, the basal planes and inert S edges (inert) still limit the activity of 2H-MoS_2. Thus, numerous approaches have been implemented to activate basal planes and S edges [147,150]. For instance, DFT studies show that adding Co reduces ΔG_{H^*} (Gibbs free energy for adsorbing hydrogen atom) for the S edge without disrupting the Mo edge; therefore, adding Co as a heteroatom increases the active sites number in MoS_2 catalysts by promoting S-edge formation [151]. Moreover, $MoS_{2(1-x)}P_x$ (where x ranges from 0 to 1) with enhanced HER activity was produced by directly mixing $MoS_{0.94}P_{0.53}$ with 20 % carbon black. This results in overpotentials of 120 and 135 mV for catalytic current densities of 10 mA/cm^2 and 20 mA/cm^2, respectively [150]. Furthermore, P-doping in MoS_2 substantially reduces the ΔG_{H^*} for nearby S atoms, as indicated by DFT measurements. This resulted in the activation of the basal planes of MoS_2 (Fig. 9d). According to Huang et al., P-doped MoS_2 produced [147] yielded superior electrochemical performance with ~ 130 mV overpotential and a smaller of ~ 49 mVdec^{-1} Tafel slope compared to pure 2H-MoS_2. Additionally, this confirms the activation of the S edge and basal planes (previously inert) following P-doping (Fig. 9e). Similar to MoS_2, WS_2 is a promising HER catalyst. In their earlier work, the authors created $WS_2/WO_{2.9}$/C hybrid nanostructures on graphite foils using a simple spin-coating process, followed by successive thermal treatments (Fig. 9f–h) [55].

Utilizing the highly coupled 2D WS_2 nanostructures with S-vacancies, 1D $WO_{2.9}$ with O vacancies, and rapid electrons transport in a carbon matrix, the hybrid membranes exhibited exceptional HER performance holding slighter Tafel slope (36 mVdec^{-1}), comparable to generally utilized Pt catalyst. Enhanced HER progress of $WS_{2(1-x)}P_{2x}$ nanorods was reported by Shifa et al. [152], with an overpotential of 98 mV vs. RHE at 10 mA/cm^2 catalytic current density and 71 mVdec^{-1} Tafel slope. This accelerated electrochemical efficacy can be attributed to the incorporation of P dopants, which led to the creation of defects and enhanced H-atom adsorption. However, catalysts based on disulfides of transition metals often exhibit reduced electrical conductivity. Additionally, graphene-based materials have garnered significant attention for their improved long-term stability, exceptional electrical conductivity, and tailored chemical properties as metal-free catalysts for HER. However, graphene materials are often electrochemically inactive and are considered unfavorable for the HER [153]. Defect engineering can be included in electrocatalytic experiments to enhance the figure of

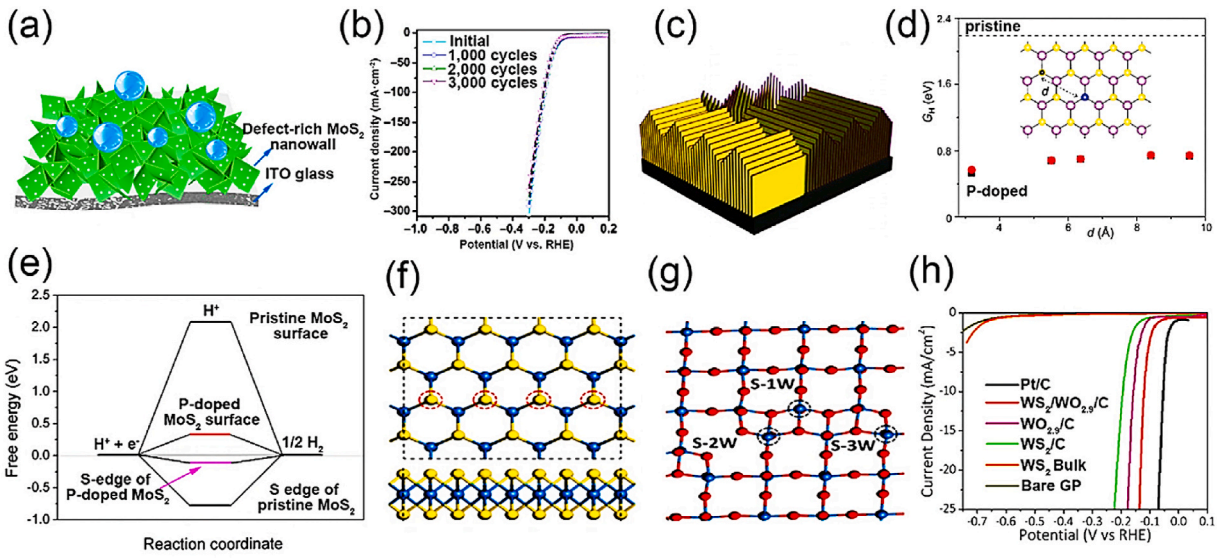

Fig. 9. Defect-rich MoS_2 nanowalls as HER catalysts: **(a)** structural representation and **(b)** LSV curves. Adapted from Ref. [148] Copyright 2017 Springer Nature Switzerland AG and Tsinghua University Press. **(c)** Visualization of stepped-site surface-terminated MoS_2 arrays. Adapted from Ref. [149] Copyright 2017, The Royal Society of Chemistry. **(d)** ΔG_{H^*} on pristine and P-alloyed MoS_2 surfaces (represented by dashed lines and dots, respectively), showing the in-plane distance between P and H. Adapted from Ref. [150] Copyright 2016. John Wiley & Sons. **(e)** The ΔG_{H^*} of pure and doped MoS_2 using a Pt reference. Adapted from Ref. [147] Copyright 2017, John Wiley & Sons. **(f)** Representation of the WS_2 monolayer (top and side); the red circles indicate potential S-vacancies. **(g)** Top view of the $WO_{2.9}$ (100) surface with three adsorption sites (S-1W, S-2W, and S-3W). **(h)** LSV curves for the HER of different samples on graphite paper (50 mm), bulk WS_2, and 10 % Pt/C. Adapted from Ref. [55] Copyright 2017, John Wiley & Sons.

merit. Recent studies have shown that introducing heteroatoms into graphene (i.e., P, N, S, and B) can be a useful strategy for enhancing the catalytic process by controlling its physicochemical features and growing the number of active sites [153].

In contrast, N-doped graphene is a remarkable material developed to enhance the graphene characteristics for many applications [154,155]. A highly effective HER catalyst, 3D N-doped plasma-etched graphene (3DNG-P), was proposed by integrating the benefits of a 3D porous architecture (freestanding), plasma-induced defects, and high-level N doping (metal-free) [155]. The proposed material revealed superior HER activity and a decreased overpotential (128 mV) compared to RHE at a current density (10 mA/cm^2) using acidic media. The synthesis procedure of N-doped graphene microtubes was explained by Zhang et al. [154] using larger inner cavities (1–2 μm) and thin walls (1–4 nm). Furthermore, N-dopants provide additional active sites for the HER experiment, leading to overpotentials of 0.464 V (0.1 M KOH solution) on the other hand 0.426 V (6 M KOH) vs. RHE at a current density (10 mA/cm^2). In addition to N doping, other heteroatoms (such as P, S, and B) have also been utilized to modify graphene to enhance its HER response. Jiao et al. synthesized and analyzed chains of heteroatom-doped (B, S, O, P, and N) graphene [156]. The performance was confirmed via experimental and theoretical measurements. The results revealed that adding graphitic carbon to the assembly of pure graphene yielded the maximum ΔG_{H^*} value, resulting in weak hydrogen bonds between the catalyst and hydrogen, thereby restricting the rate of the entire HER reaction. Furthermore, the B-doped sample exhibited a lower ΔG_{H^*} value, whereas the P-doped sample displayed higher activity. Additionally, the analysis of the experimental parameters demonstrated a reduction in the overpotential of graphene, bringing it closer to that of MoS_2. To accelerate HER performance, tuning graphene through dual or triple heteroatom doping has recently garnered significant attention [153]. Owing to synergistic effects, this specific double/triple doping can lead to diverse electron donor behaviors. For instance, coupling N- and S-dopants through geometric defects in the lattice-atom of the graphene creates a synergistic effect that alters the ΔG_{H^*} value and results in an exceptional HER response [157]. The resulting structured product demonstrates HER responses by an onset potential of 0.13 V vs. RHE, 80.5 $mVdec^{-1}$ a Teflon slope, and 0.28 V overpotential against RHE at 10 mA/cm^2 current density. Furthermore, F- and N- co-doped porous graphene, through pyridinic N arrangements, exhibits excellent HER response, featuring an initial 150 mV overpotential, 87 $mVdec^{-1}$ Tafel slope and enhanced stability, and the polarization curve remains unaffected even after 5000 cycles comparable to the primary scans [158].

3.1.1.2. Defects and strains. To harness the TMDs catalytic potential, phase engineering is considered a powerful implement. However, there is a noteworthy advantage in exploring and optimizing thermodynamically stable TMDs (1H/2H) for the HER. A main assumption is that, as mentioned before, the 1H/2H TMDs basal plane is comparatively inactive for the HER despite constituting a significant portion of the surface area. Wang et al. postulated that various sulfur vacancies can stimulate the HER on the basal plane of MoS_2. Moreover, recently discovered S-depleted sites have shown promise for the Tafel and Heyrovsky reactions. This insight was obtained by measuring the ΔG_{H^*} value in corresponding Volmer reaction [159]. Although it is a great encounter to precisely regulate S-vacancies, several studies have suggested that MoS_2 monolayers can generate specific beneficial S-vacancies for the HER [160–162]. In 2016, researchers employed monolayered MoS_2 nanocrystals for the HER [137] and more recently produced a method to develop monolayered 1H MoS_2 nanocrystals through a lateral size of approximately 12.5 nm. These S-depleted nanocrystals displayed significantly improved HER catalytic response compared to MoS_2 nanocrystals, with 29 $mVdec^{-1}$ Tafel slope and a low onset 60–75 mV overpotential. Furthermore, they demonstrated a high j_o of 4.13×10^{-3} mA cm^{-2} [137]. These promising outcomes can be attributed to the Volmer-Tafel pathway reaction of the Mo-S Nanocrystals, supported by their low Tafel slope (approximately 30 mV dec^{-1}). These robust Mo-S-based catalysts are extremely promising for use in HER applications. DFT measurements showed the impact of defect creation, along with increased exceptional electronic states along with lattice strain under CB, synergistically improves electron transport facility that turns into amplified HER activity. Creating controlled S-depletion and the corresponding HER catalytic response are crucial for driving further

innovations.

Zheng et al. extensively elucidated the relation between MoS_2 (S-vacancies) and HER catalytic responses at defective sites (Fig. 10a) [163]. Without surface S depletion on the basal plane, the expected ΔG_{H^*} was approximately 2 eV. With the surface S-depletion of 3.12 %, this value diminishes to 0.18 eV as demonstrated in Fig. 10b; and approaches 0.08 eV with 9.38–18.75 % S-vacancies. Compared to the best-configured edge sites, a nuanced arrangement of S-vacancies can lead to a more suitable ΔG_{H^*} approaching thermoneutrality. Achieving more efficient adsorption of hydrogen atoms occurs when ΔG_{H^*} on the basal plane becomes negative and close to 0 eV during the Volmer process (Fig. 10b). Owing to the stronger hydrogen binding caused by strain on the basal plane, the catalytic efficiency of the HER is improved [164,165]. Further modeling was conducted to determine ΔG_{H^*} of the MoS_2 single layers under uniaxial elastic strain. ΔG_{H^*} decreased with increasing strain at each investigated S-vacancy concentration, as shown in Fig. 10c. This finding is valuable because the stability of MoS_2 monolayers reduces with an increase in the number of S-vacancies. A small amount of applied strain enhances the stability while reducing the number of S-depletions, ultimately improving the HER performance. Simulated electronic structures revealed that S-depletion leads to the emergence of a defect level within the energy gap just below the conduction band minimum [145,163,166].

A monolayer of 1H MoS_2 behaves as an n-type semiconductor example with the Fermi level positioned near the conduction band [145]. With increased S-vacancies, the bands shifted towards the Fermi level, resulting in a rational explanation for the gradual enhancement of hydrogen binding (Fig. 10b and c). Tensile strain also affects the gap states, further improving the hydrogen bonds [139,163,165]. Zheng and his colleagues successfully created a robust 1H MoS_2 sheet using the smallest possible edge ratio, aligning with the theoretical insights discussed earlier [163]. They fabricated both strained MoS_2 monolayers (1.35 ± 0.15 %) and unstrained MoS_2 single layers by controlling the amounts of S-vacancies (e.g., 21.88 %, 18.75 %, 12.50 %, 8.00 %, and 6.25 %, relative to the total number of S atoms) [163]. Additionally, theoretical simulations showed that single-layered MoS_2 strained (1.35 ± 0.15 %) using 12.5 % S-vacancies revealed the finest accorded ΔG_{H^*} value approaching 0 eV [163]. In strain-free MoS_2 sheets, weak HER catalytic response was observed, with an initial overpotential exceeding 350 mV (as examined through the current density at 10 mV cm^{-2}) and a Tafel slope (90 mV dec^{-1}). The TEM image of the MoS_2 monolayer (4 × 4 nm) with approximately 43 S-vacancies (≈11.3 % S-vacancy) revealed Mo atoms, two S atoms (2S, one S atom above and the other below the Mo plane), single S atoms (1S, only one S below the Mo plane), and zero S atoms (0S, both above and below the Mo plane were depleted), as depicted in Fig. 10d.

This HER performance outperformed that of MoS_2 without strain (e.g., 98 mV dec^{-1} Tafel slope). The onset overpotential and Tafel slope of MoS_2 monolayer abridged upon S-depletion were 250 mV and 82 mV dec^{-1} (12.5 % S-vacancies) respectively. Further addition of strains (1.35 ± 0.15 %) resulted in dropped values (170 mV and 60 mV dec^{-1}) respectively as visualized in Fig. 10e and f. While the catalytic reaction for the HER might be insignificant compared to the previously discussed phase-engineering and edge-enriched TMDs [139,167,168], the efficiency improvement achieved through S-depletion and strain presents a promising potential for HER optimization. For the basal planes of the 1H and 1T 2D-TMDs, the ΔG_{H^*} values consistently exceeded 0 eV. Surface chalcogen vacancies can enhance H binding and reduce ΔG_{H^*}, potentially leading to a thermodynamically neutral state. Previous studies have demonstrated this enhancement in 2D $MoSe_2$ and $MoSSe_2$ Nanocrystals with Se vacancies [144]. Therefore, it's significant to remember that the stability of TMDs is compromised by surface vacancies and strain, which can limit the broader application of these approaches. Other methods, for example, surface doping can be explored to mitigate this issue and stabilize the structure while achieving the desired ΔG_{H^*}.

3.1.2. *Phase engineering*

As mentioned previously, TMDs are distinctive layered composites. Three different phases of 2D TMDs monolayered building blocks arise as 1H, 1T, and 1T as represented in Fig. 1. Entire phases displayed intensely unique catalytic and electronic properties. MoS_2, WS_2, MoS_2 Se, and WS_2 Se exist in the most thermodynamically stable form, known as 1H. (or 2H). Because 1H and 2H are semiconducting for all these materials, they have extremely low electrical conductivities. These materials can

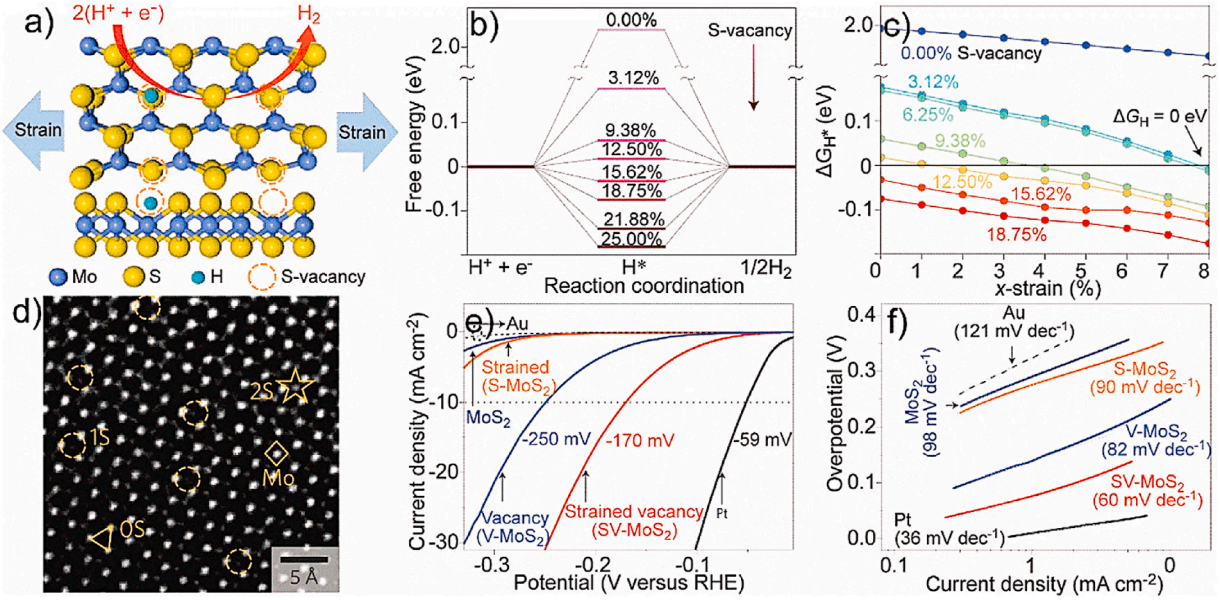

Fig. 10. (a) Visualization of top and bottom sights on basal plane of MoS_2 using strained S-depletion (S-vacancies) on the basal plane. Theoretical assessment of ΔG_{H^*} versus **(b)** HER coordination by introducing S-vacancies and **(c)** x strain with S-vacancies. **(d)** Aberration-corrected TEM photograph of the MoS_2 monolayer [4 × 4 nm and 43 S-vacancies (~11.3 %)]. **(e, f)** Polarization curves and respective Tafel plots of certain species (S-MoS_2, V-MoS_2, and SV-MoS_2 are the MoS_2 monolayer with 0 % S-vacancy, 12.5 ± 2.5 % S-vacancies, and both the 1.35 ± 0.15 % strain and 12.5 ± 2.5 % S-vacancies, respectively). Adapted from Ref. [163] Copyright 2016 Springer Nature Limited.

be manipulated to create 1T metallic TMDs, each with unique catalytically active regions and considerably enhanced electron-transport performance. Moreover, theoretical simulations have shown that the basal planes of several 1T TMDs, for instance, MoS_2, TaS_2, NbS_2, WS_2, VS_2, and TiS_2, are catalytically active for HER; on the other hand, basal planes of 1H/2H phases are commonly inert because of the high ΔG_{H^*} [169,170]. The fundamental limiting factors of 1T TMD monolayers are their stability and low-cost synthesis. The HER progress of WS_2 monolayers (chemically exfoliated) was described by Chhowalla et al. combining 1H and 1T phases (Fig. 11) [139]. When the 1H WS_2 thin films were analyzed, the results showed an onset over potential 150–200 mV with 110 mV dec^{-1} Tafel slope Growing the concentration of 1T WS_2 while reducing the ratio of 1H WS_2 increased the HER performance (Fig. 11a–d) [139]. The catalyst showed 55 mV/dec Tafel slope (without iR correction, 60 mV/dec), 80 mV–100 mV potential, and current density (j_o) of 2×10^5 A cm^{-2} [139]. The catalyst was applied to a glassy carbon electrode with greater than five monolayer thicknesses; therefore, it is feasible that the HER activity of WS_2 monolayers, essentially 1H monolayers, was overstated [139]. To maintain quick electron transfer between the electrode and catalyst in 1H semiconducting monolayers, the catalyst on the electrode should ideally have a thickness comparable to that of the monolayer itself. Re-stacking the monolayers deteriorates their HER performance [137]. Therefore, the relation between the catalytic efficiency and Mo-S loading value on a glassy carbon electrode is essential [137]. Upon increasing the catalyst loading, the double-layer capacitance, also called C_{dl} (which indicates the active surface area of the total sites), gradually decreased [137]. When the mass density exceeded 100 μg cm^{-2}, C_{dl} decreased upon

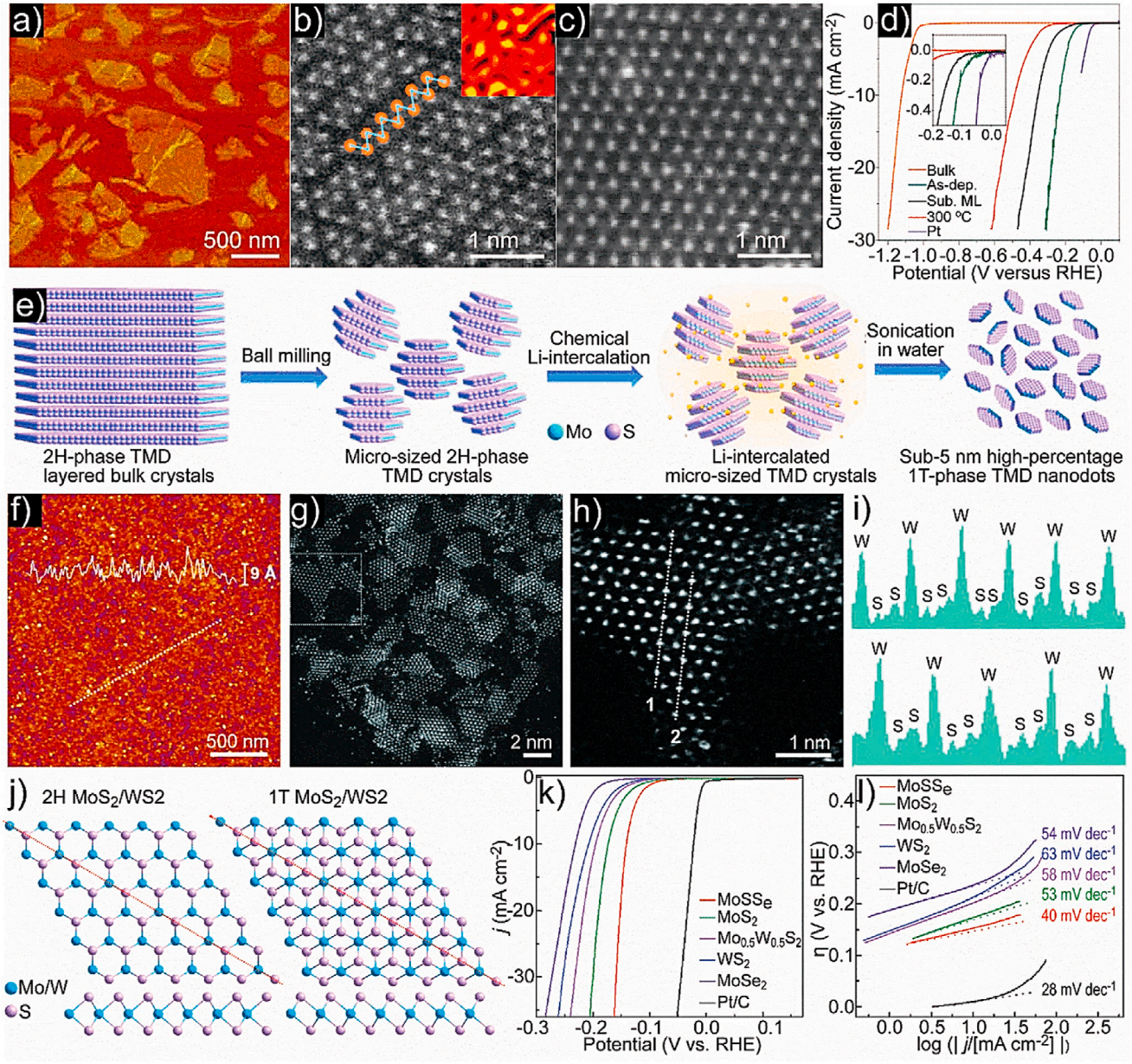

Fig. 11. (a) AFM images of WS_2 monolayers. HAADF-STEM image of the WS_2 monolayer with deformed **(b)** 1T and **(c)** 1H patterns. **(d)** Polarization diagrams for bulk and WS_2 monolayers (including 1H and 1T phases), sub-monolayer WS_2, and Pt nanoparticles. Adapted from Ref. [139] Copyright 2013 Springer Nature Limited. **(e)** Graphical representation of the method used to create monolayer 1T TMDs from their bulk counterparts. **(f)** AFM image of as-fabricated monolayer WS_2 nanocrystals and **(g)** HAADF-STEM images. **(h)** Equivalent filtered image of two dimensional-WF-ABSF (**g**). **(i)** Brightness designs with dotted lines (from **h**) (line 1: top; line 2: bottom). **(j)** Structures of 1H/2H and 1T TMDs for specific nanocrystals, (**k**, **l**) polarization curves, and the resulting Tafel graphs are shown. Adapted from Ref. [144] Copyright 2018, John Wiley and Sons, Ltd.

increasing the catalyst content. Owing to all the factors mentioned earlier, re-stacking or agglomeration of single-layer nanocrystals can drastically reduce the catalytic performance; more specifically, the slope of the Tafel plot becomes less favorable [137]. The HER efficiency of 1H WS_2 single layers with varying sizes (edge lengths of 400–800 nm) has also been studied [171]. The single layers on the gold foil were produced using the CVD method, and these single layers were then immediately utilized for the HER. These monolayers had Tafel slopes ranging from 102 to 104 mV/dec and current density values ranging 6.31 from 17.78 μA cm^{-2}.

The exchange current density is analogous to that of 1T WS_2 nanosheets at 2×10^{-5} A cm^{-2} because of the reaction between the Au foil and WS_2 [139,171]. For instance, 1H MoS_2 single layers grown on Au foils exhibit 61 mV dec^{-1} Tafel slope and j_o of 38.1 A cm^{-2}, which is substantially better than WS_2 with a reduced size [138]. The lateral dimension of 1T MoS_2 nanosheets synthesized by $LiBH_4$ exfoliation could be as small as 1 μm, and their 1T content can reach 80 % [164,172]. The increment in Tafel slope was observed from 40 to 75–85 mV dec^{-1} when the 1T nanosheets were annealed, resulting in an onset overpotential. The robust HER proficiency of 1T MoS_2 sheets might be ascribed to the low value of ΔG_{H^*} (about 0.12 eV) at the basal plane, which is comparable to the ΔG_{H^*} value of 0.08 eV of 1H/2H MoS_2 sheets at the edge [169,170,173]. Moreover, it is also possible to produce 1T MoS_2 monolayers for the HER with smaller dimensions by combining phase engineering with edge enrichment. MoS_2 exfoliated by intercalation of n-butyllithium was reported by Li et al., in 2017 [174]. Post-processing involving ultrasonication (100–200 nm lateral size, >70 % phase content) results in exfoliated nanosheets and converts few-layered MoS_2 into 1T MoS_2 nanosheets. The as-synthesized nanosheets of 1T MoS_2 revealed an onset overpotential (156 mV) and a Tafel slope (42.7 mV/dec). Because of the smaller ratio of 1T:1H phases and the frequent presence of multilayered sheets in the sample, the 1T MoS_2 sheets described here exhibited inferior performance compared to the 1T MoS_2 sheets discussed previously [174]. MoS_2 monolayers demonstrate significantly improved performance compared with many 1H-MoS_2 monolayers [137,138,141]. To utilize and expose the maximum possible number of surface active edges, He et al. produced a solvothermal technique for the fabrication of 1T WS_2 vertically aligned nanosheets using a lateral dimension of several micrometers with a phase composition of approximately 70 % 1T [175]. The Vertically aligned 1T WS_2 nanosheets had Tafel slope (43 mV/dec) and overpotential (118 mV) at 10 mA cm^{-2} current density.

In contrast, the Tafel slope and initial overpotential of the flat 1T WS_2 sheets on a glassy carbon electrode were only 52 and 230 mV, respectively. This improvement can be attributed to boost in the 1T basal plane exposure. Exposing the basal planes in 1T TMDs is important for efficient HER. Recently, monolayered 1T TMDs nanocrystals have also been described by Zhang and co-workers in 2018 [144]. Ball milling was

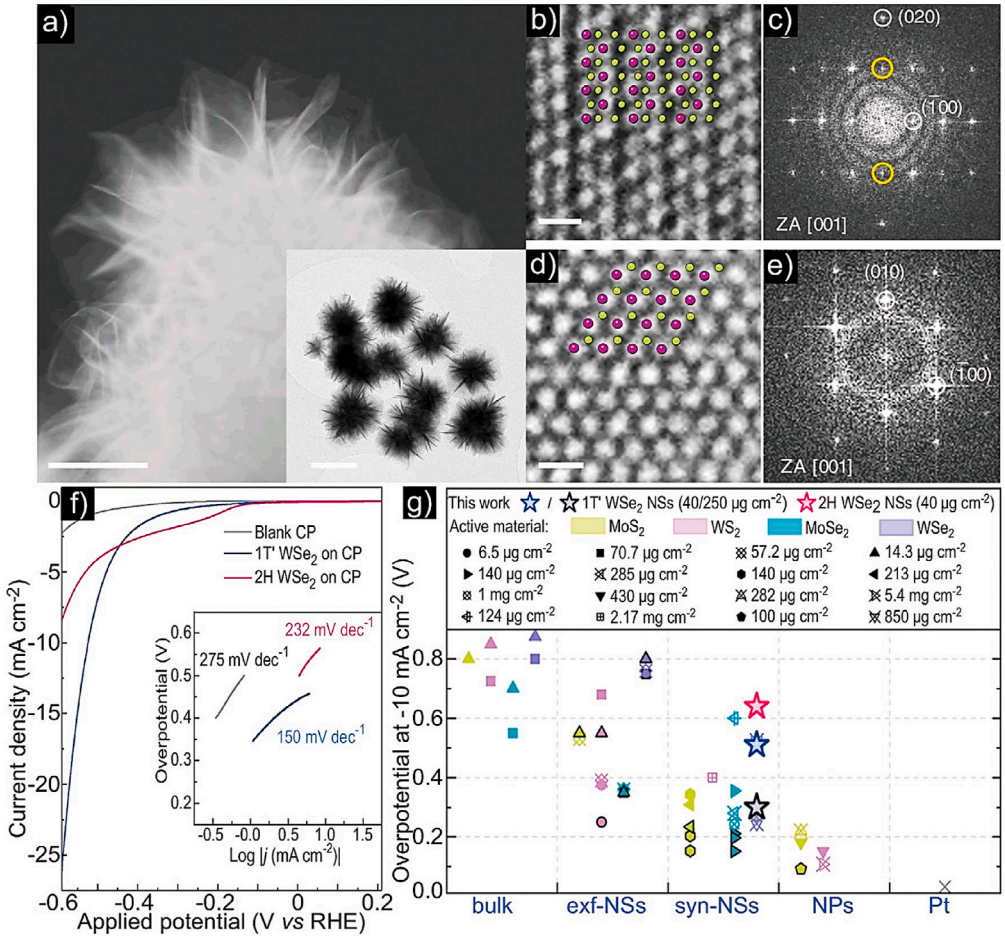

Fig. 12. (a) TEM photograph of WSe_2 branched nanoflowers (100 nm scale bar), with the inset showing a cluster of WSe_2 nanoflowers in an overview image (200 nm scale bar). **(b)** An enlarged image (scale bar: 0.5 nm) is presented, featuring a superimposed crystal model depicting the zigzag chains of tungsten atoms in the 1T′ phase of WSe_2. **(c)** Utilizing FF, the pattern of the region depicted in c was generated, with yellow circles emphasizing kinematically forbidden (010) reflections. **(d)** An enlarged image (scale bar: 0.5 nm) is presented, featuring a superimposed crystal model illustrating the uniformly spaced hexagonal lattice of the 2H WSe_2 phase. **(e)** An FFT pattern is generated, highlighting overlaid crystal models. **(f)** Polarization curves of 2H and 1T′ WSe_2 nanosheets were created on carbon paper, with the inset ascribing to parallel Tafel plots. **(g)** Evaluation plot for the reported TMD group VI for HER employing electrocatalysts (synthesized nanosheets (syn-SNs) and exfoliated nanosheets (exf-nanosheets)). Adapted from Ref. [176] Copyright 2019 Springer Nature Limited.

utilized to initially reduce bulk TMDs (approximately tens of micrometers in size) into micro-sized particles (approximately 1 μm in size), which were then intercalated by n-butyl lithium to generate a variety of monolayered TMD nanodots includes, MoS_2, WS_2, $MoSe_2$, $Mo_{0.5}W_{0.5}S_2$, and MoS_2Se with an adequately high percentage (67–80 %) of the 1T phase. These nanodots were smaller than 5 nm, as shown in Fig. 11e–j, and the Tafel slope ranged from 40 to 63 mV dec^{-1} (Fig. 11k and l). The MoSSe dots likely have the lowest Tafel slope owing to the creation of Se-depleted sites during preparation [144]. The 1T MoS_2 nanocrystals had a lower Tafel slope than the 1H single-layered nanocrystals and 1T single-layered sheets [137,168], but a fundamental explanation is lacking thus far (arrangements and distillations of the 1T nanocrystals still require further improvement). While performing phase engineering on TMDs, a vital consideration is the ambiguity between the 1T and 1T′ phases, both of which have distinctive electrical characteristics and distinct HER pathways. Recent research by Sokolikova et al. [169] has elucidated the aqueous-phase synthesis of kinetically stabilized 1T'WSe_2 on arbitrary substrates (Fig. 12a–e). At an extremely low 40 μg cm^{-2} mass loading, the Tafel slope of 1T′ WSe_2 was 150 mV/dec; however, after thermal conversion to 1H/2H WSe_2, it significantly increased to 232 mV/dec (Fig. 12f). Although the Tafel slope showed improved performance at 10 mA cm^{-2} comparable to the already optimized TMDs (Fig. 12f and g), this technique illustrates how phase engineering can enhance catalysis when performed appropriately. Additional approaches have also been suggested to improve the productivity of the catalytic process, which will be addressed in more detail below.

3.1.3. *Interface engineering*

Interface engineering is an essential technique for fabricating high-performance electrocatalysts. The interfacial interactions between the two materials lead to simultaneous modifications in both the electrochemical properties, significantly affecting the electrocatalytic performance. This has been confirmed through numerous experiments [177–179]. Interface engineering can be broadly classified into two subfields: synergistic interaction and heterostructure engineering. These subfields are intertwined and often interact with one another. Although heterostructure engineering usually involves complex chemical interactions between distinct nanomaterials, a synergistic interface involves direct interactions with minimal electron transit [177]. The interface engineering approach can be used to synthesize highly active electrocatalysts through specific physiochemical properties. For instance, Zheng et al. created an extremely thin nanosheet (Fig. 13a) via in situ hybridization of g-C_3N_4 and N-graphene [177]. The XAS spectra indicated the formation of out-of-plane orientated C-N bonds, resulting from the robust interfacial contact between the layers of g-C_3N_4 and N-graphene (Fig. 13b). These interlayer bonds can alter the electrical state of the composite, facilitating electron transfer from the N-graphene layer to g-C_3N_4 (Fig. 13c). Consequently, the hybridized C_3N_4/NG (NG: N-doped graphene) exhibited superior HER activity compared to that of the physically mixed sample (Fig. 13d). Several DFT simulations suggest that this improvement arises from the synergistic contact between the chemical and electrical couplings, which improves the proton adsorption kinetics and reduces the surface of C_3N_4@NG (Fig. 13e) [177]. This activity pattern demonstrates the DFT model's applicability beyond metals. The significant discovery here is that metal-free materials with rational design offer large potential for extremely effective electrocatalytic HER, comparable to precious metals (Fig. 13f).

Furthermore, Duan et al. constructed a 3D freestanding hybrid film consisting of N-graphene and g-C_3N_4, further confirming these concepts. The performance of this film paralleled that of the 2D heterostructured C_3N_4@NG hybrid [177,180], offering a promising technique for creating 3D porous films that might be applied to various 2D materials [51,167,181]. Two factors can be responsible for the efficiency of the film-like electrode: (1) the exposed catalytic active sites optimized by the 3D porous structure and (2) hierarchical intra- and interlayer pores produced in the films, enhancing the surface area and mass transfer rate in

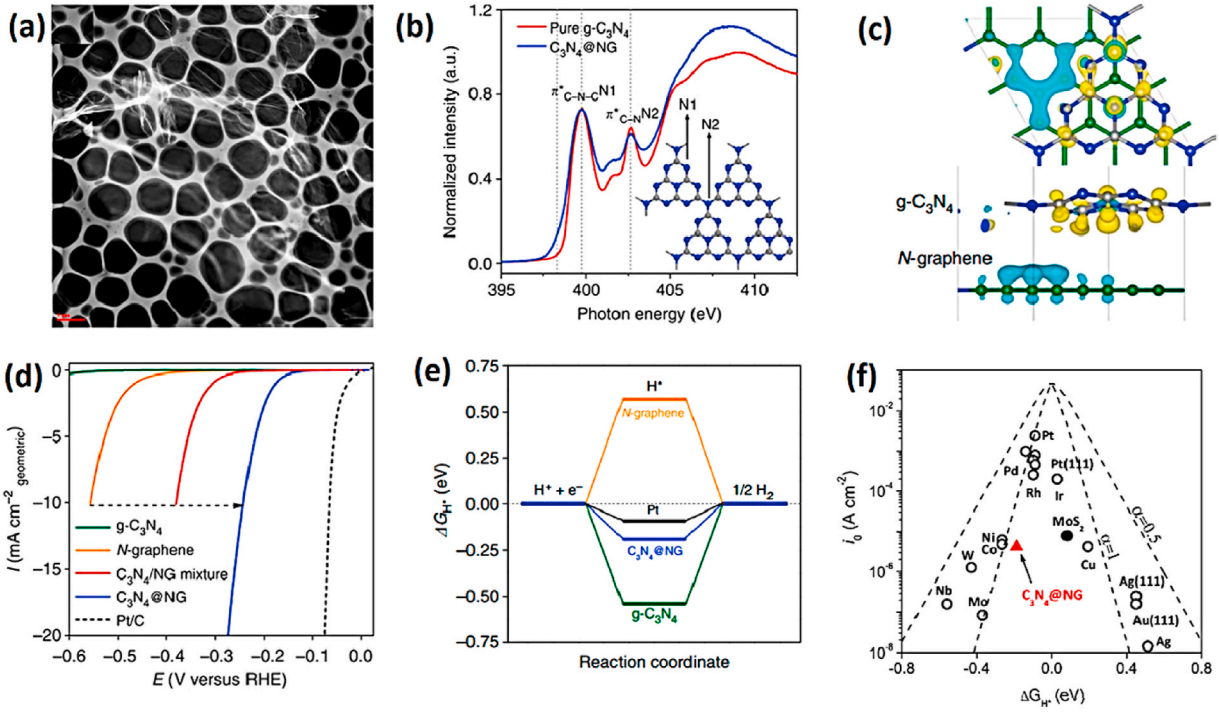

Fig. 13. (a) HAADF-STEM images of C_3N_4@NG nanosheets. **(b)** Inset shows two nitrogen species in the g-C_3N_4 network in the nitrogen K-edge NEXAFS different catalysts spectra. **(c)** Interfacial electron transferring in C_3N_4@NG. Electron accumulation is shown in yellow and cyan isosurfaces denote electron depletion. **(d)** HER polarization curves of different electrocatalysts in an acidic medium. **(e)** A schematic showing the free energy for the HER of the three metal-free catalysts at equilibrium. **(f)** Volcano plot of i_0 vs. ΔG_{H^*} for freshly prepared C_3N_4@NG and common metal-based catalysts. Adapted from Ref. [177] Copyright 2014 Springer Nature Limited.

the electrocatalytic phenomenon. In addition to metal-free heterostructures, 2D TMDs have contributed to diverse structural realizations. Hybrid structures such as $MoS_2/CoSe_2$, featuring an interface heterojunction, exhibit significantly higher catalytic performance than MoS_2 and $CoSe_2$ alone [182]. Notably, the $MoS_2/CoSe_2$ hybrid displayed long-term stability compared with MoS_2, demonstrating the successful integration of MoS_2 stability with $CoSe_2$'s catalytic activity. Similar behavior was perceived for amorphous Co-Mo-S_x chalcogens [183]. Combining the more reliable MoS_x units with the more energetic CoS_x building blocks resulted in increased HER activity. Researchers have speculated that both morphological and electrical effects including substrate-adsorbate binding energies contribute to the stability and activity of TMD materials [183]. Various hybrid systems e.g., rGO/WS_2 [184], MoS_2/Au [185], and rGO/MoS_2 have also been created using same approaches [186]. The strategy for creating heterostructures in two-dimensional electrocatalysts sis often influenced by the following factors: (1) at least one of the 2D nanocomposites should exhibit significant catalytic behavior for the chosen electrocatalytic procedure; (2) the hybrids must possess electrical solid conductivity for efficient electron transportation for reactive intermediates; and (3) the strengths of single material should reimburse for the weaknesses of the other, i.e., low conductivity or intermediate absorption energy.

3.1.4. Heteroatoms doping

Incorporating heteroatoms is a helpful technique that is extensively used to stimulate the HER efficiency of TMD electrocatalysts [187]. Doped heteroatoms efficiently alter the electronic structure, primarily the d-band of TMD-based catalysts, and reduce the ΔG_{H^*} value of electrocatalysts, thereby facilitating the HER process. It can partially replace silicon or metal sites in TMDs [114,188,189] or nonmetal sites [112,190,191] to boost the HER proficiency. This unlocks new possibilities for modifying the fundamental characteristics of host materials.

3.1.4.1. Metal doping. Various metals, including Vanadium, Fe, Co, Cu, Ni, and Zn, have been successfully incorporated into TMD-based electrocatalysts. Doping can generally catalyze the HER by enhancing the catalytic sites [167,192], improving conductivity [193], and/or improving the electronic structure [114]. The HER activity of TMD electrocatalysts is influenced differently by various dopants, making it crucial to carefully select doping elements. For instance, to accelerate the MoS_2 efficiency for HER, doping with Ni and Co is commonly employed [192,194]. These two materials can minimize the ΔG_{H^*} and enhance the density of active edges, thereby enhancing HER activity. The development of a single-step hydrothermal technique to synthesize Co-doped MoS_2 was done by Xiong et al. [195], which demonstrated improved HER activity compared to pristine MoS_2 (Fig. 14a). Co-MoS_2-0.5 (with a co-doping concentration of 0.5 mmol) displayed the highest HER activity in alkaline conditions, by a potential difference of approximately 90 mV. This improvement can be attributed to the reduction in ΔG_{H^*} (Fig. 14b) and the controlled electronic structure resulting from cobalt doping. Xi et al. observed that MoS_2 nanosheets' conductivity accelerated with the doping of V atoms, but there were no significant improvements in the active sites. In contrast, Co and Ni doping increases the density of active sites (Fig. 14c) [193].

3.1.4.2. Nonmetal doping. Nonmetal-doped TMDs exist in various forms, each exhibiting distinctive characteristics and exceptional HER efficiency. Compared to metal doping, non-metal doping increases ΔG_{H^*} and deforms the crystals or creates an amorphous structure, resulting in numerous active sites [191,196,197]. Xie et al. hydrothermally synthesized O_2-doped MoS_2 nanosheets hydrothermally [96]. Owing to the low synthesis temperature, only a few Mo-O bonds were formed naturally in the MoS_2 nanosheets. DFT results indicated that the bandgap of the O_2-inserted MoS_2 reduced to 1.30 eV from the 1.75 eV of 2H MoS_2. O_2 absorption leads to a contracted bandgap, an increased carrier density, and enhanced conductivity. Consequently, the MoS_2 catalyst with oxygen integration displayed a notably elevated catalytic activity for HER, achieving a η of 120 mV (at 1 mA cm^{-2}) and a Tafel slope of 55 mV dec^{-1}. Fu et al. studied $WS_{2(1-x)}Se_{2x}$ single-layer nanosheet and examined the effect of Se doping [191]. Introducing a larger Se atom into WS_2 induces crystal distortion, generating a polarized electric field that accelerates H_2O splitting. The replacement of S atoms with Se atoms

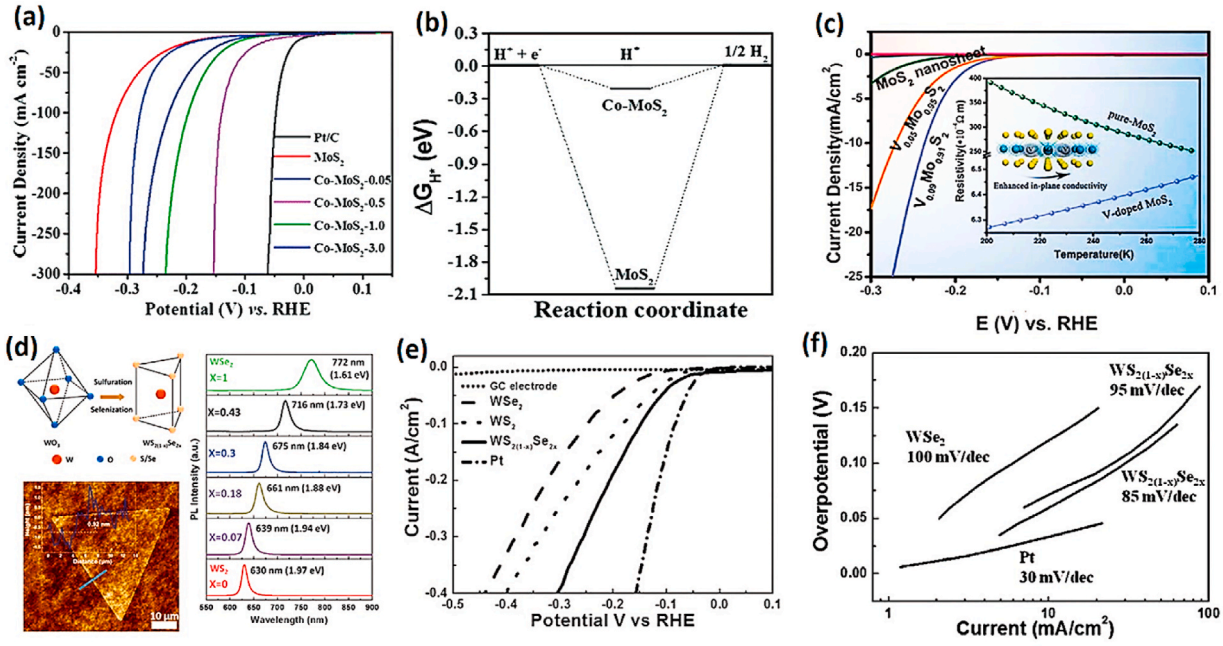

Fig. 14. (a) Demonstration of LSV curves for HER and **(b)** estimated ΔG_{H^*} for pristine and Co-doped MoS_2. Adapted from Ref. [195] Copyright 2018, The Royal Society of Chemistry. **(c)** LSV curves of pristine and V-doped MoS_2 nanosheets. Adapted from Ref. [193] Copyright 2014: The Royal Society of Chemistry. **(d)** h-$WS_{2(1-x)}Se_{2x}$ growth via synchronized selenization and sulfurization of monoclinic WO_3. AFM image and equivalent PL spectra (at room temperature) for the grown $WS_{2(1-x)}Se_{2x}$ nanosheet. **(e)** Assessment of the HER experimental findings for monolayer WS_2, WSe_2, Pt, glassy carbon, and $WS_{2(1-x)}Se_{2x}$ (x = 0.43). **(f)** Consistent Tafel slope values. Adapted from Ref. [191] Copyright 2015, John Wiley and Sons, Ltd.

initiated this process. In this manner, single-layer $WS_{2(1-x)}Se_{2x}$ nanosheets demonstrated a comparatively reduced η of 80 mV for achieving 10 mA cm^{-2}, whereas WSe_2 and WS_2 nanosheets required 150 and 100 mV, respectively, to reach the same level (as depicted in Fig. 14d–f). Jin et al. discovered that adding chlorine (Cl) to MoS_2 and $MoSe_2$ catalysts notably increased their HER efficacy and altered the electronic features of amorphous $MoSe_2$ and MoS_2.

The MoS_2 and $MoSe_2$ catalysts exhibit similar behaviors (Fig. 15a and b) [198,199]. The HER performances of MoS_xCl_y and $MoSe_xCl_y$ were further enhanced owing to their optimal electrical structure and ample active sites (Fig. 15c and d) [198]. Moreover, amorphous MoQ_xCl_y (Q = S and Se) and micropyramids (MPs) were created on the n^+pp^+ Si substrate to form a highly effective photoelectrochemical reaction (PEC-HER) photocathode (Fig. 15e). These PEC-HER photocathodes displayed HER efficiencies of 43 and 38.8 mA cm^{-2} at 0 V against RHE for MoS_xCl_y/Si and MoS_xCl_y/Si, respectively, outperforming n Pt/Si photocathodes (Fig. 15f). In general, there are two ways in which the addition of heteroatoms can increase the HER effectiveness of TMD catalysts: (i) introducing a new element can cause changes in the crystal structure and increase the number of catalytic sites; (ii) different dopants can significantly alter the electrical configuration of the catalysts owing to the different electron configurations. Depending on the scenario, this might result in the optimization of ΔG_{H^*} or the corresponding energy levels. However, dopant selection requires caution, as different atoms can impact catalytic activity differently, and incorrect choices might even have a negative impact on the whole performance. The HER activity can show varied outcomes, sometimes opposite to expectations, even with the same dopants. This is another perplexing discovery [187,192]. This complexity may result from different preparation methods and doping levels.

3.1.4.3. Increase in electronic conductivity. The coupling of TMD electrocatalysts using conductive materials i.e., graphene [184,200–202], carbon paper [203,204], and metal substrate [205–207] is a common plan employed to accelerate the HER activities of TMDs. This approach creates a conductive framework with multiple pathways for electron transfer and increases the effective electron capture surface area (ECSA) and active edges for the HER mechanism. For instance, Dai et al. successfully employed a solvothermal method to synthesize a composite electrocatalyst of rGO and MoS_2 nanosheets [186]. Incorporating TMD-based electrocatalysts with conductive substrates enhances the effective ECSA and active sites for the HER process. These electrocatalysts establish a conductive framework with several internal electron pathways, and the movement of charge carriers from MoS_2 to the electrodes is expedited owing to their interaction with the graphene network. The utilization of 3D conductive metal substrates (i.e., Fe, Ni, Cu, and Ti foams) provides a larger surface area than combinations of TMDs along with supplementary carbon materials for instance carbon nanotubes, rGO, and carbon nanofibers leading to significant improvements [208–210]. Conductive scaffold coupling, which enhances electron transport between substrates and catalysts while increasing the catalytic surface area, can notably reinforce these effects. Importantly, the catalyst's intrinsic property often remains unchanged after the optimization process is complete [37,211]. Yan et al. [210] designed hierarchical nanoassembly of $MoS_2/Co_9S_8/Ni_3S_2$/Ni, tiered structure endows high performance toward HER and OER over a very broad pH range (Fig. 16a and b). The obtained C_{dl} value for CoMoNiS-NF-31 is 60.9 mF cm^{-2} (Fig. 16c and d), which is the largest among the control samples. Besides, as seen in Fig. 16e, by controlling the ratio of Co and Mo precursors, the C_{dl} values increase from 15 mF cm^{-2} for Co_9S_8/-Ni_3S_2/NF to 30.9 mF cm^{-2} for CoMoNiS-NF-41 and climb to the maximum value of 60.9 mF cm^{-2} for CoMoNiS-NF-31, and then the C_{dl} decreases to 10 mF cm^{-2} for MoS_2/Ni_3S_2/NF. Fig. 16f reveals DFT analysis of prepared catalyst.

3.1.4.4. Optimization of kinetics. Heterostructures possess a fundamental property in semiconductor physics, enabling the directional acceleration of electrons through appropriately matched band structures in combined materials [212]. The HER is an electrochemical surface reaction that relies significantly on the tendency of the catalyst to interact with hydrogen in the electrolyte [213,214]. A critical parameter in determining the viability of an HER catalyst is the Gibbs free energy for the hydrogen atoms' adsorption. The design of heterostructure catalysts directly contributes to the effective optimization of reactive

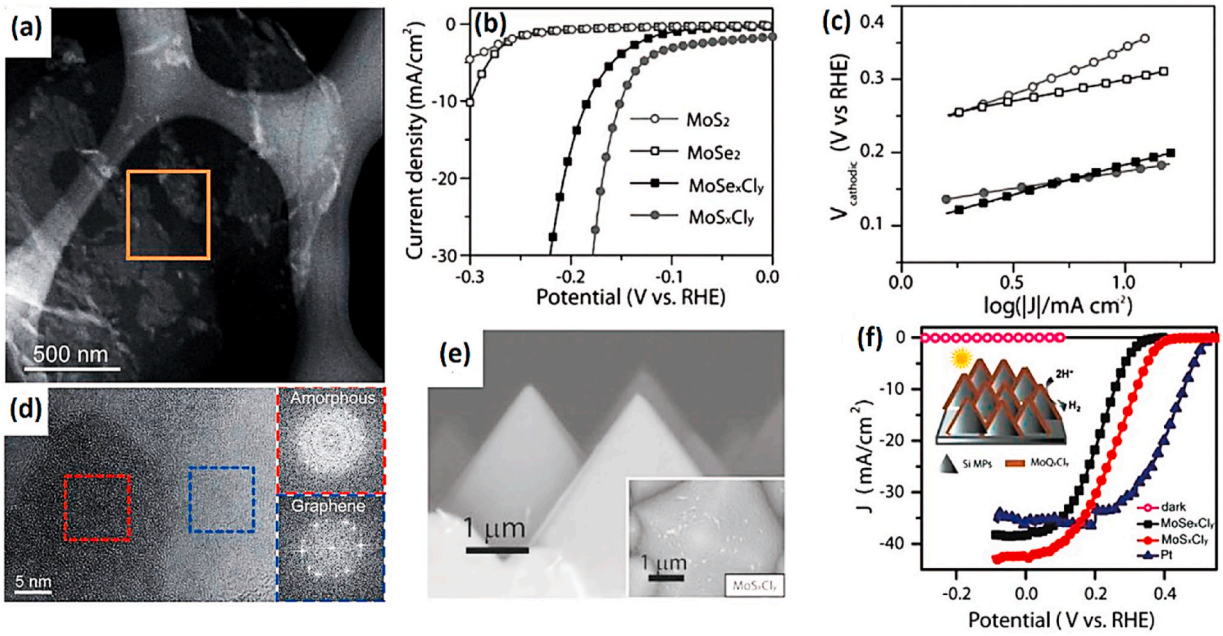

Fig. 15. (a) HRTEM photographs and corresponding local FFT pictures of the MoS_xCl_y-VG (vertical graphene) sheet. Adapted from Ref. [199] Copyright 2015, The Royal Society of Chemistry. **(b)** HER performance and **(c)** Tafel plots of MoS_xCl_y, $MoSe_xCl_y$, MoS_2, and $MoSe_2$. **(d)** HRTEM and local FFT images of a MoS_xCl_y-VG sheet. **(e)** Top-down SEM image of MoQ_xCl_y/Si. **(f)** PEC-HER performance of $MoSe_xCl_y$/Si MPs (squares), MoS_xCl_y/Si MPs (circles), and Pt/Si MPs (triangles) photocathodes. Trials were conceded in H_2SO_4 (0.5 M) under 1 sun irradiation. Adapted from Ref. [198] Copyright 2015, John Wiley and Sons, Ltd.

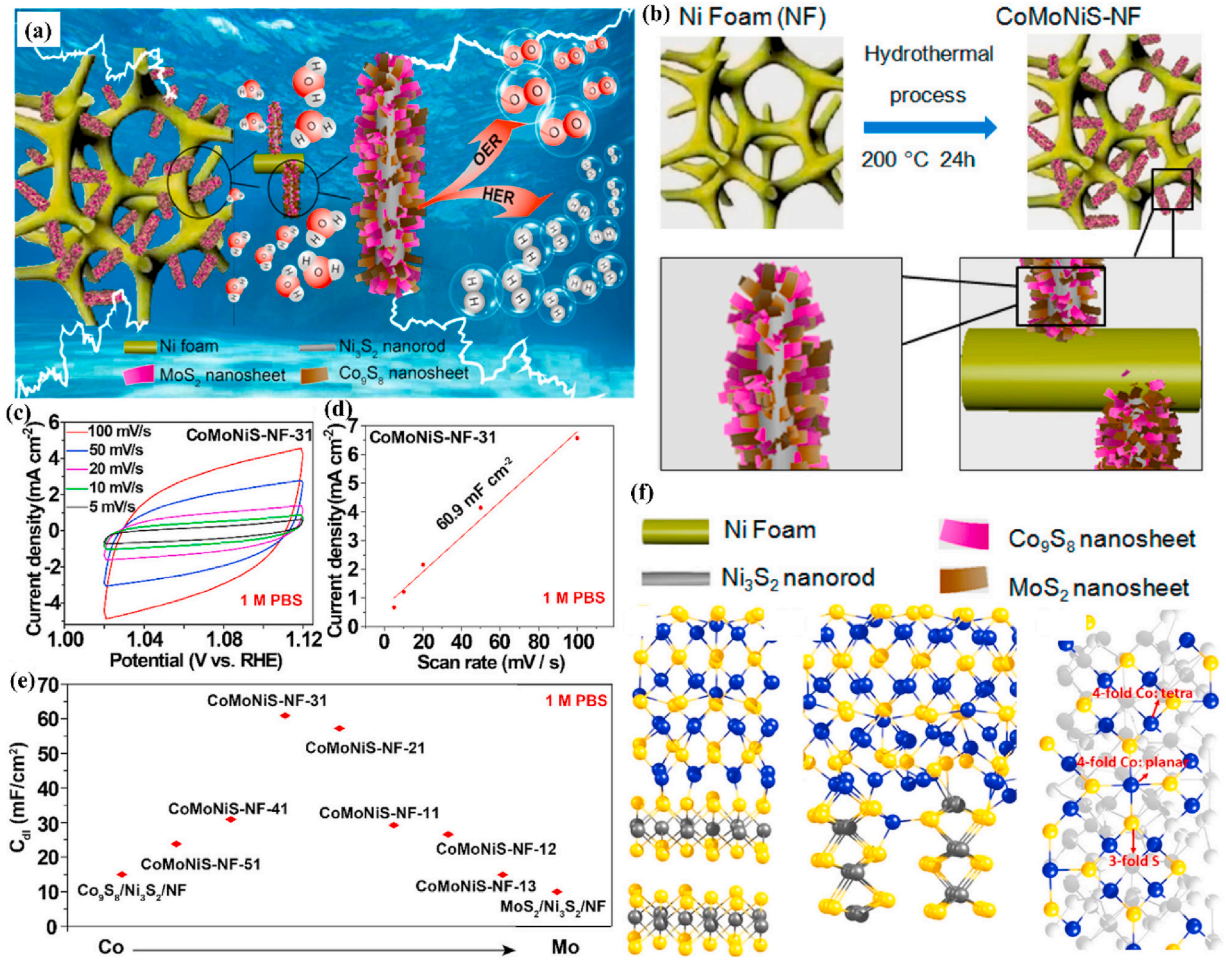

Fig. 16. Schematics of hierarchical nanoassembly of $MoS_2/Co_9S_8/Ni_3S_2/Ni$; (b) Synthesis and growth of hierarchical CoMoNiS-NF-xy composites via a one-pot hydrothermal method; (c) CV curves at different scan rates of CoMoNiS-NF; (d) Plots of current density as a function of scan rate for CoMoNiS-NF; (e) Influence of Co/Mo ratio on the double layer capacitance (C_{dl}) for CoMoNiS-NF-xy; **(f)** DFT-optimized structures of MoS_2/Co_9S_8 interfaces. Adapted from Ref. [210] Copyright 2019, American Chemical Society.

kinetic processes. Yu et al. fabricated a $MoS_2/CoSe_2$ heterostructure using a simple hydrothermal procedure (Fig. 17a) [182]. This hybrid electrocatalyst exhibited a threshold voltage of 75 mV in its as-prepared state, with a 36 mV dec^{-1} Tafel slope to achieve 10 mA cm^{-2}. Individually, MoS_2 and $CoSe_2$ showed weak responses and performed similarly to a typical Pt/C electrocatalyst (Fig. 17b). In this research, the $MoS_2/CoSe_2$ heterostructure served two crucial functions for enhancing catalytic activity. First, the formation of MoS_2 and $CoSe_2$ interfaces generates numerous sites with high catalytic rates. Second, the heterostructure effectively optimized ΔG_{H^*} (Fig. 17c), bringing its value closer to that of Pt (111) [215]. This moderate ΔG_{H^*} successfully lowered the reaction barrier, making it easier for the H_2 molecules to form H atoms.

Moreover, H_2 molecules exhibited adsorption energy of as low as 0.5 eV, which facilitated their release from the active edges and accelerated the HER procedure Chlor-alkali electrolysis, extensively used in industrial settings for hydrogen production [217,218], results in slower HER kinetics in alkaline media compared to acidic medium. This was primarily due to the sluggish kinetic rate of water dissociation [219]. Efficient research on HER alkaline catalysts is crucial for reducing energy consumption in the chlor-alkali industry. In alkaline electrolytes, the HER process is initiated by water dissociation; the absence of H^+ ions necessitate an extra amount of energy source to create protons. The fabrication of heterostructure catalysts using many functional sites offers a practical methodology for accelerating the entire process.

4. CO_2 reduction reactions

The use of two-dimensional materials for CO_2 reduction reactions holds promise in the realm of renewable energy and sustainable chemistry. To enhance the efficiency of this process, several strategies have been devised, each targeting specific facets of the reaction mechanism. In the following sections, we explore these strategies in greater detail, including the utilization of tailored catalyst design, precise control of surface defects, modulation of electronic structure, and advances in reactor engineering. By synergistically implementing these strategies, researchers aim to unlock the full potential of 2D materials in CO_2 reduction, offering a pathway toward more effective and sustainable CO_2 conversion technologies with the potential to combat climate change. Table 4 contains the latest accomplishments in CO_2 reduction reactions.

4.1. Strategies

4.1.1. Surface modification

High levels of exposed low-coordination atoms on the surfaces of 2D nanosheets make them prone to modification by metallic and nonmetallic species. Alloying with various metals may increase the binding energies of molecules i.e., CO, and disrupt the scaling relationships between similarly adsorbed intermediates, thereby reducing the reaction potential [235]. For example, *CO tends to bind to metals solely through

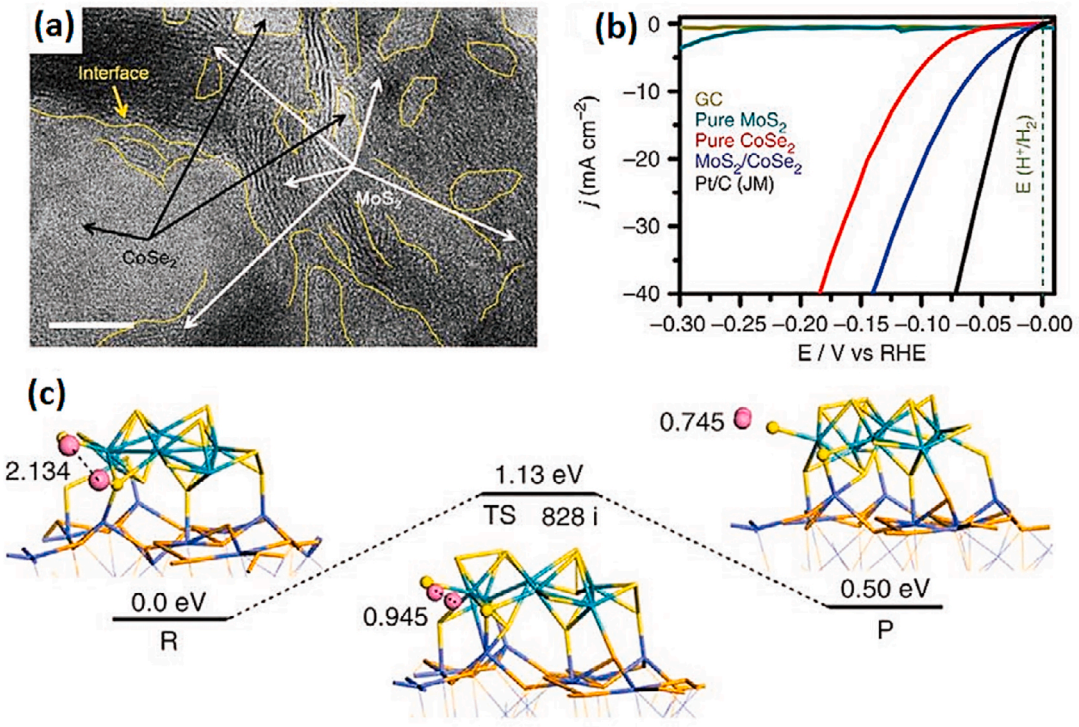

Fig. 17. (a) HRTEM image of $MoS_2/CoSe_2$ after stability assessment (scale bar = 10 nm). **(b)** HER experimental results for pure MoS_2, $CoSe_2$, and Glassy carbon electrodes, these electrodes enhanced with $MoS_2/CoSe_2$ hybrid and Pt/C catalyst. **(c)** Calculated energy barrier and corresponding mechanisms for the HER on the $MoS_2/CoSe_2$ hybrid surface, illustrating the Volmer-Tafel pathways. In Fig. (c) orange, yellow, blue, azure, and pink spheres represent Se, S, Co, Mo, and H atoms, respectively. Adapted from Ref. [216] Copyright 2015, The Royal Society of Chemistry.

the C atom; however, introducing an oxophilic atom on the surface may selectively fix *COOH and *CHO over *CO. Alternatively, modifying nanosheets through the introduction of adatoms (Co, Mn, Bi, As, Li, H, C, S, N, B, P, O, F, and I) can significantly modify their electronic and geometric characteristics. This modification has the potential to adjust the binding strengths of various intermediates and alter reaction energetics, consequently influencing the activity and selectivity of CO_2 conversion. Buxing et al. [236] recently demonstrated that doping Pd with Te makes it possible to electrocatalytically convert liquid CO_2 to CO in a selective way (Fig. 18). DFT studies indicated that Te atoms preferentially attach to the terrace sites of Pd, inhibiting hydrogen formation. In contrast, CO generation arises from CO_2 activation and adsorption on high-index Pd sites. Chemical doping of two-dimensional materials, especially those by controllable configurations and doping levels, remains a task. The activity and selectivity of chemical reactions are also influenced by surface functional groups, such as amines. Introducing a catalyst to amines locally increases CO_2 concentration on the electrode surface. Additionally, amine can stabilize CO_2^- through H-bond reaction, reducing the onset potential for lowering CO_2 to CO_2^- by producing a maintaining environment. This contributes to a more stable environment, thus decreasing the onset potential for CO_2 conversion to CO_2^-. Amine can also aid *CO bonding, assisting in CO reduction to methanol and the C-C coupling required for C_2 formation [7,236]. Doping through heteroatoms, e.g., B, N, and/or Nican, significantly reduces the CO_2 adsorption barriers and enhances the electrocatalytic CO_2 reduction efficiency. Even at a low doping level of 0.6 atom percent, quaternary N doping can considerably increase the carrier concentration to 2.6×10^{13} cm^{-2}, which is four times greater than that of unmodified graphene [237]. It is important to note that advanced research is necessary to know the electrochemical effect reduction of single- and co-doped graphene containing various p-block and d-block elements alongside B, N, and Ni.

4.1.2. *Surface-structure tuning*

Adjusting four critical factors, – surface defects, visible crystal lattice, surface porosity, and surface phase, is a critical approach for tuning the structural features of 2D nanosheets. Enhancing CO_2 absorption by metal oxides or hydroxides can be achieved by surface tuning involving oxygen vacancies. CO_2 molecules have a strong affinity for O_2 vacancies, and the presence of an oxygen atom from CO_2 attached to an O_2 vacancy defects reduces the energy gap for CO_2 activation [238]. Similarly, vacancies of chalcogen atoms on nanosheets can enhance the CO_2 adsorption rates, allowing selective CO_2 conversion to CO [7]. The vacancy or surface density can be adjusted by lowering the surface temperature or doping the material using a lower-valent foreign element. Forming hierarchical micro-, meso-, and macroporous structures on two-dimensional nanosheets can improve CO_2 adsorption, capture, and conversion efficiency. The reactants and products transferring and diffusion rate over the electrodes are facilitated by macropores (>50 nm), but mesopores (2–50 nm) and micropores (2 nm) offer a large number of active sites. The widths of the pores or channels can be altered to tailor the selectivity based on the sizes of the reactant or product molecules. Different surface facets exhibit varying polarizing powers and Lewis acidities, manipulating CO_2 adsorption and activation. Surface composition and order significantly affect the catalytic behavior and selectivity of TMDs and numerous metals. TMD's 1T phase of TMD exhibits weak intrinsic charge-transport resistance. Compared to the 2H phase, the strained lattice distortion leads to a significant density of active sites. Altering the ions absorbed near the surface can modify electrical properties and catalyst efficiency. Specifically, introducing equitably oxidized metal electrocatalysts to the surface, such as Sn, Bi, and Co, results in enhanced performance compared with pure metals because of the larger surface area [239].

Kang and colleagues [222], introduce a design concept for a three-component catalyst aimed at syngas production, providing insights into its operational mechanisms. The subsequent demonstration

Table 4
CO_2 reduction reaction.

Electrocatalyst	Synthesis Method	Engineering Strategies	Electrolyte	Selected Product	Catalyst Loading (mg cm $^{-2}$)	Onset Potential (mV)	Faradic Efficiency (Vs. RHE) (Unless Mentioned)	Tafel Slope (mV dec^{1})	Comments		Ref.
									Advantages	Disadvantages	
Cu CeO_2	Hydrothermal Method	Surface Modification	0.1 M $KHCO_3$	CH_4	5	–	58 % @ 1.80 V	-	Moderate Faradaic efficiency; potential for optimization.	Requires optimization for better performance.	[220]
ZIS/NDCC	Hydrothermal Method	Surface Modification	0.5 M $KHCO_3$	Ethanol	–	–	42 % @ 0.7 V	199	Reasonable efficiency for ethanol.	Efficiency might need improvement for practical applications	[221]
Co_3O_4 –C Dots C_3N_4	Hydrothermal Method	Surface Structure Tunning	0.5 M $KHCO_3$	CO	0.127	–	89 % @ 0.60 V	-	High Faradaic efficiency for CO	Detailed performance characteristics not provided.	[222]
g C_3N_4/MWCNT	Two Step Approach: Co Precipitation and Polycondensation	Surface Structure Tunning	0.1 M $KHCO_3$	CO	0.36	–	60 % @ 0.75 V	-	Potential for enhanced performance.	Moderate Faradaic efficiency for CO	[223]
Nb-doped MoS_2	CVD	Optimization of Electrolyte	50 vol % Ionic liquid	CO	–	31	12 %–82 % @ 0.16 to−0.8 V	-	Electrolyte optimization can lead to varied efficiency	Wide range in efficiency indicates inconsistency	[224]
WSe_2 nanoflakes	CVT Growth Technique	Optimization of Electrolyte	50 vol % EMIM BF4 in water	CO	–	54	24 % @ 0.164 V	-	–	Low Faradaic efficiency; improvement needed for practical use	[225]
SnO_2/CC	Hydrothermal + Calcination (Chemical Etching Method)	Surface Modification	0.5 M $NaHCO_3$	HCOOH	0.34	880	87 ± 2 % @ −1.6 V vs. Ag/AgCl	79	High Faradaic efficiency for formic acid.	High onset potential.	[226]
V_o rich Co_3O_4	Hydrothermal Synthesis	Surface Modification	0.1 M $KHCO_3$	HCOOH	–	780	87.6 % @ −0.87 V vs. SCE	37	High efficiency for formic acid.	Reduction in onset potential desirable.	[227]
SnS_2/rGO	Hydrothermal Method	Surface Structure Tunning	0.5 M $NaHCO_3$	HCOOH	2	680	84.5 % @ −1.40 V vs. Ag/AgCl	83	Good efficiency for formic acid.	Balance between loading and efficiency needed.	[228]
N-doped graphene	Pyrolysis	Surface Modification	0.5 M $KHCO_3$	KHCO3	0.2	−300	~73 % @ −0.84 V vs. Ag/AgCl	135		Moderate efficiency; improvement needed.	[229]
Metallic tin quantum sheets/ graphene	Reduction strategy	Surface Modification	0.1 M NaOH	Formate	–	−0.85 V	>89 % @ −1.8 V vs. SCE	83	High efficiency	Onset potential and stability need investigation.	[230]
Ni-N-Gr	Hummer's method-Ultrasonication	Surface Modification	0.1 M $KHCO_3$	CO	0.3	−0.5 V	90 % @ −0.7 to −0.9 V	90	High efficiency and good onset potential for CO	–	[231]
Ni–graphene nanosheets	Impregnation and reduction method	Surface Structure Tunning	0.5 M $KHCO_3$	CO	0.2	–	95 % @ −0.64V	110	Very high Faradaic efficiency for CO.	Stability and durability need assessment	[232]
NiN-GSs	Electrospinning	Surface Modification	0.1 M $KHCO_3$	CO	0.2	Less than 230 mV	93.2 % @ 0.7 V	138.5	High Faradaic efficiency (93.2 % at 0.7 V); promising onset potential (less than 230 mV).	The detailed long-term stability and scalability might need assessment.	[233]
CoPc/CNT (2.5 %)	Ultrasonication	Surface Structure Tunning	0.1 M $KHCO_3$	CO	0.4	–	92 % @ −0.63 V	–	Good Faradaic efficiency for CO (92 % at −0.63V); utilizes a potentially effective combination of cobalt phthalocyanine with carbon nanotubes	Specifics about Tafel slope and onset potential improvements for practical applications might be needed	[234]

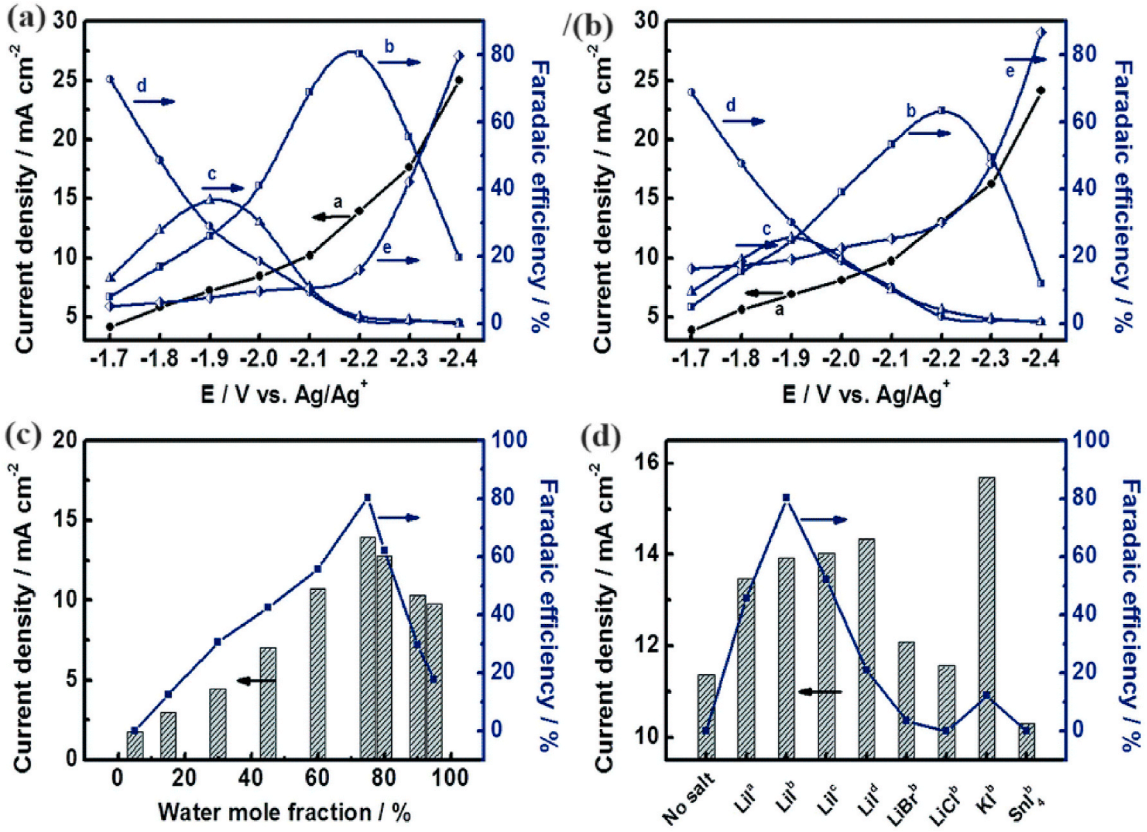

Fig. 18. Current density and Faradaic efficiency of the products at different applied potentials over **(a)** Cu 1/BN-C_{30} and **(b)** Cu 2/BN-C_{30} electrodes in an aqueous solution of 25 mol% [Emim]BF_4 and 75 mol% water in the presence of 0.01 M LiI at 1 atm CO_2 and room temperature with 5 h electrolysis. Curve (a) is the current density; curves (b)–(e) are the Faradaic efficiency of (b) acetic acid, (c) methanol, (d) formic acid, and (e) H_2. Current density and Faradaic efficiency of acetic acid at an applied potential of −2.2 V vs. Ag/Ag+ with **(c)** different water mole fractions and **(d)** different kinds of promoters (a: 5 mM; b: 10 mM; c: 20 mM; d: 30 mM). Adapted from Ref. [236] Copyright 2017 The Royal Society of Chemistry.

establishes the viability of this concept, confirming that Co_3O_4-C-Dots-C_3N_4 serves as an effective, adjustable, stable, selective, and cost-efficient electrocatalyst for syngas production. This catalyst facilitates the reduction of CO_2 to CO in aqueous solutions with a minimal overpotential (0.17 V vs. RHE). The total current density of H_2 and CO generation can potentially reach up to 15 mA/cm^2 at a potential of −1.0 V vs. RHE. Notably, the H_2/CO ratio of syngas generated by Co_3O_4-C-Dots-C_3N_4 is modifiable from 0.07:1 to 4:1 by regulating the applied potential. The catalytic mechanism of CO_3O_4-CDots-C_3N is presented in Fig. 19a. Furthermore, the mechanisms involving CO_2 reduction and H_2 evolution using the HER-CDots-C_3N_4 catalyst are discussed. Fig. 19b shows Pt-CDots-C_3N_4 investigated under the same conditions as CO_3O_4-CDots-C_3N_4, where only H_2 was detected with no CO_2 reduction as a product. Pt is the most effective electrocatalyst for accelerating the HER [222,240]. When used as a catalyst, Pt-CDots- C_3N_4 enhances the intensity of the effective HER channel, altering the balance between the HER and reduction towards H_2 production while systematically controlling the reduction of CO_2 to CO.

The MoS_2-CDots-C_3N_4 electrocatalyst remains highly active for HER, yielding nearly 90 % hydrogen production, albeit with a minor contribution of carbon monoxide (a few percent of the total current). The Faradaic efficiencies (FEs) of CO do not surpass 10 % for MoS_2-CDots-C_3N_4 (inset of Fig. 19c). Moving to the Au-CDots-C_3N_4 electrocatalyst (Fig. 19d), its HER activity remains superior to CO_2 reduction activity, yet the CO production is more significant compared to the MoS_2-CDots-C_3N_4 catalyst (CO production FE reaching 25 %, inset of Fig. 19d). Consequently, the ternary HER-CDots-C_3N_4 concept is demonstrated to be generalizable beyond Co_3O_4 catalysts, proving valid for different HER catalysts. To achieve a relatively higher CO/H_2 ratio, it is essential to employ a HER catalyst with moderate activity, tipping the balance toward CO_2 reduction. The extent of HER activity directly influences the relative amount of CO, with lower HER activity resulting in a larger proportion of CO. This conclusion is verified by reducing the amount of Au in the ternary Au-CDots-C_3N_4 electrocatalyst. Electrochemical tests (Fig. 19e) reveal that halving the amount of Au enables the generation of syngas with a CO to H_2 volume ratio greater than one. An exceptional characteristic of the h-Au-CDots-C_3N_4 catalyst is its remarkably high mass activity for syngas production, exceeding 700 A/gAu for both CO and H_2 production (~1500 A/gAu for total current) at −0.7 V for the catalyst depicted in Fig. 19e. This activity surpasses previous reports for efficient Au electrodes for CO production by two orders of magnitude [241,242].

Zhang et al. [226] created hierarchical mesoporous nanosheets of SnO_2 on carbon fibers, demonstrating a robust electrocatalyst for the reduction of CO_2 using significant efficiency and selectivity. The microstructures of SnS_2 and SnO_2 grown on CC (carbon cloth) were examined using SEM (Fig. 19f–i). Fig. 19j shows the potential versus the average current density for 1-h electrolysis. CO_2RR kinetics increases by applying potential went negatively from 0.95 V to 1.8 V (relative to Ag/AgCl (3 $_M$ KCl)); all subsequent possibilities are relative to this reference, as expected. In Fig. 19k, the relationship between FEs of the products and potential is depicted. The data reveals that formate, H_2, and CO collectively exhibit an FE of approximately 100 % across the entire potential range, with no detection of any other products via NMR or gas chromatography analysis. The Tafel analysis in Fig. 19l shows a Tafel slope of 79 mV dec^{-1} for SnO_2/CC, which is nearly the expected value of 59 mV for a fast electron transport step followed by a rate-limiting chemical reaction. The rate of formate synthesis was

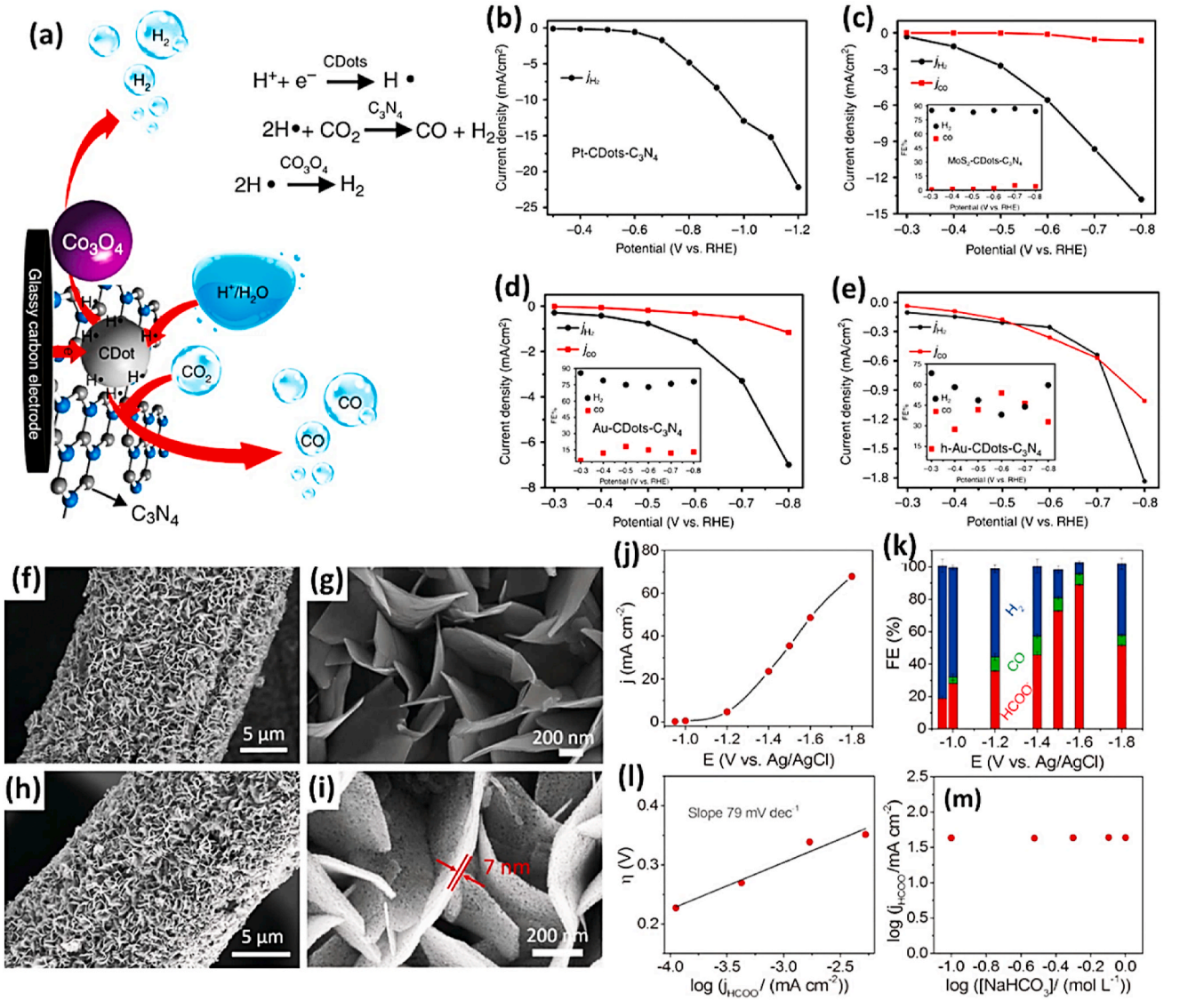

Fig. 19. (a) A visual illustration of the Co_3O_4-CDots-C_3N_4 reaction process showing the catalytic response of the proposed candidate using many HER catalysts: **(b)** Pt-CDots-C_3N_4 catalyzed HER current density vs. applied potential; **(c)** MoS_2-CDots-C_3N_4 catalyzed HER and CO_2 reduction current density, and FEs of H_2 and CO (inset) vs. applied potential in CO_2-saturated 0.5 M KHCO electrolyte; **(d)** Au-catalyzed HER and CO_2 reduction current densities and FEs of H_2 and CO (inset) vs. applied potential; **(e)** Au-CDots-C_3N_4 catalyzed HER and CO_2 reduction current densities and FEs of H_2 and CO (inset) vs. applied potential. All analyses were performed in a CO_2-saturated 0.5 M $KHCO_3$ electrolyte. Adapted from Ref. [222] Copyright 2017 Nature Publishing Group. **(f–i)** SEM images illustrating the SnS_2 nanosheets. **(j)** Current density of the SnO_2/CC electrode in CO_2-saturated 0.5 m $NaHCO_3$ solution at different applied potentials; **(k)** Corresponding FE for formate, CO, and H_2; (l) Tafel plot of the SnO_2/CC electrode; **(m)** Partial current density for formate vs. concentration of $NaHCO_3$. Adapted from Ref. [226] Copyright 2017, John Wiley and Sons, Ltd.

almost entirely independent of the $NaHCO_3$ concentration (Fig. 19m).

4.1.3. *Optimization of electrolyte and electrolyzer*

The quantity, concentration, and type of electrolyte significantly influence the CO_2 electrolysis [243]. Alkaline electrolytes, i.e., KOH, are beneficial for CO_2 reduction because they reduce the activation barriers for CO_2 reduction and CO-CO coupling, thereby mitigating undesired effects [244]. Ionic liquids are another potential electrolyte for enhancing the electrochemical effect reduction of CO_2. Previous studies have shown that employing Ionic liquid electrolytes with various electrodes can lead to CO_2 reduction [245–247]. It is hypothesized that forming a complex via ion pairing between the Ionic liquid cation and the CO_2 radical anion could decrease the activation overpotential [245]. However, some reports suggest that aqueous electrolytes can achieve only approximately ten times higher than those of Ionic liquids [246]. Notably, Ionic liquids exhibit 100 times greater CO_2 solubility than water, facilitating a higher CO_2 concentration at the electrode-electrolyte interface.

Additionally, Ionic liquids have been found to effectively suppress hydrogen formation through interfacial adsorption. Thus, liquefied Ionic liquids using ion-pairing and HER-inhibiting capabilities are promising for minimizing CO_2 emissions in industrial processes [248]. However, a challenge arises, as Ionic liquids might prove unstable in high current density conditions mandatory for industrial-scale operations. A flow-cell electrolyzer with a gas diffusion electrode cathode has been developed to overcome the low solubility of CO_2 in electrolytes [249,250]. This setup established a triple-phase boundary by introducing gaseous carbon dioxide at the electrode-electrolyte interface, enabling rapid dioxide transformation. To ensure the stability and commercial viability of CO_2 electrolyzers, interface engineering should be employed to reduce issues such as flooding and salt build-up. Moreover, a robust electrode-electrolyte interface is essential to facilitate the ingress and

egress of gaseous CO_2 and its products within the gas diffusion electrode without compromising the electrical and ionic conductivities at elevated reaction sites.

5. Computational guidance for electrocatalysis by 2D materials

The advancement of novel characterization methodologies has led to a growing utilization of in situ tools for monitoring catalytic reactions, to precisely elucidate the catalytic mechanisms. Theoretical calculations serve as a crucial approach to reimburse limitations in experimental techniques by enabling the investigation of electronic-scale alterations occurring during catalytic reactions. Over recent decades, the application of theoretical simulations in the realm of defective electrocatalysis has significantly contributed to the analysis of catalytic mechanisms in emerging catalysts [251–253].

Nonetheless, pinpointing the precise active site and reaction intermediates in intricate catalytic reactions remains a daunting task solely through experimental inquiry. Particularly in the realm of CO2RR, where diverse reaction pathways can yield products such as carbon monoxide, formic acid, ethylene, or ethanol, discerning the actual reaction routes, intermediates, and the interplay between carbon-carbon coupling reactions and the HER poses a difficult challenge, impeding elucidation via experimental means [254]. For instance, the potential of Dual-Atom Catalysts (DACs) as facilitators of C2 product generation is underlined by their capacity to deliver two metal sites that bolster *CO coverage on surfaces. Nevertheless, experimental observations often reveal DACs to exhibit elevated Faradic efficiency for CO, with limited incidence of multi-carbon product formation [255,256]. Li et al. employed Density Functional Theory (DFT) calculations and extracted evidence suggesting that C−C coupling predominantly transpires away from the metal-top sites [257].

The significance of theoretical calculations in understanding the correlation between structures and performance is evident. By constructing a reaction model, researchers can delve into the fundamental reaction pathways, identify pivotal steps to measure reaction rates, and subsequently refine chemical reaction conditions. The efficacy of theoretical calculations extends to interpreting the underlying processes and reaction pathways of electrocatalysis at the atomic level. Moreover, DFT simulations serve as predictive tools, aiding in the design of catalysts and the controlled synthesis of desired structures. Theoretical modeling facilitates catalyst structure optimization, validates design outcomes, and complements experimental investigations [258].

5.1. Oxygen reduction and evolution reactions

One of the primary advantages of computational analysis lies in its capacity to inform the design and optimization of 2D materials tailored for specific electrocatalytic functions. This predictive capability is invaluable, enabling researchers to hypothesize and assess the impact of various modifications at a theoretical level, thereby mitigating the need for extensive and costly experimental trials. Furthermore, by elucidating key reaction mechanisms and potential catalyst sites, computational analysis assists in customizing materials to achieve enhanced catalytic efficiency and selectivity for ORR and OER. Essentially, computational analysis serves as both a predictive and diagnostic tool, augmenting our comprehension of electrocatalytic processes and propelling innovation in the development of more efficient and effective 2D material-based electrocatalysts [258]. For instance, Zhang et al. engineered atomically distributed Ni atoms onto an N-doped hollow carbon matrix (HCM@Ni-N) [259]. In alkaline conditions, the HCM@Ni-N exhibited an OER overpotential of only 304 mV to reach a current density of 10 mA cm^{-2}, significantly lower than that of RuO_2 (393 mV), indicative of excellent OER activity. Through calculated distributions of charge density, they observed a notable change in the electronic distribution of N-doped HCM after Ni decoration. Additionally, the d-band center of Ni in HCM@Ni-N displayed a leftward shift, with a downshift from −0.94 eV to −2.04 eV attributed to the Ni-N interaction. According to the d-band center theory, this alteration could facilitate adsorbate desorption and reduce energy barriers. Free energy pathways of the OER, calculated through DFT simulations, aligned well with experimental results. Similarly, Ouyang and colleagues developed a bifunctional electrocatalyst for the HER and OER in an alkaline electrolyte by encapsulating Co and β-Mo_2C into N-doped carbon nanotubes (Co/β-Mo_2C@N-CNT) [260]. Leveraging the heterointerface between Co and β-Mo_2C, the OER activity of β-Mo_2C was significantly enhanced. DFT calculations corroborated that the combined effect of N-CNTs, Co, and β-Mo_2C led to low energy barriers of intermediates, thereby greatly improving HER and OER kinetics.

Under the guidance of DFT calculations, Wang et al. achieved the successful synthesis of a series of topological carbon defects through a straightforward N-removing strategy. Among these defects, adjacent pentagons (A-C5) demonstrated the most promising catalytic performance for the ORR, while the edge divacancy defects (C585-2) exhibited favorability for the HER [261]. DFT calculations were instrumental in exploring the relationship between the original carbon structure, the type of N configuration obtained, and the corresponding defect structures. For instance, comparisons were made between perfect carbon network, graphitic-N, and C585 (Fig. 20a), as well as edge-rich hexagonal structure, pyridinic-N, and S-C5 (Fig. 20b), and edge-rich pentagon, pyrrolic-N, and A-C5 (Fig. 20c). Additionally, Jiang and colleagues employed a spontaneous gas-foaming method to fabricate a range of promising trifunctional electrocatalysts termed defect-rich N-doped ultrathin carbon nanosheets for HER, OER, and ORR [262]. Notably, the NCN-1000-5 variant exhibited remarkable characteristics in rechargeable Zn-air batteries, including high energy density (806 Wh/kg), low charge/recharge voltage gap (0.77 V), and exceptionally long cycle life (over 300 h). DFT calculations played a crucial role in identifying the intrinsic active sites for electrochemical reactions. By investigating the catalytic performance of various active sites for ORR and OER, the researchers generated a volcano plot (Fig. 20d), highlighting the armchair edge carbon atoms adjacent to the graphitic-N as possessing the lowest overpotential, thus positioning them as the optimal catalytic active centers for the specific electrocatalytic processes (Fig. 17e–g) [262].

5.2. Hydrogen evolution reaction

Computational analysis plays a pivotal role in understanding and optimizing the catalytic performance of 2D materials for the HER, which is central to hydrogen production in clean energy technologies. By employing computational tools, researchers can investigate atomic-level interactions, identify key active sites, and elucidate reaction pathways. This approach enables the tuning of electronic and surface properties of 2D materials, thereby enhancing their efficiency in catalyzing the HER process. Consequently, computational analysis serves as a cornerstone in the development of effective and sustainable methods for hydrogen production [258]. Ye and colleagues designed a novel Pt single-atom catalyst (Pt SAC) utilizing aniline-stacked graphene as the support material (Pt SASs/AG). This catalyst exhibited remarkable HER performance, with overpotentials (η) as low as 12 mV at 10 mA cm^{-2} and a mass current density of 22,400 A g^{-1} Pt at $\eta = 50$ mV, surpassing commercial Pt/C catalysts by 46 times [263].

With the assistance of DFT calculations, they found that the interaction between the atomical Pt and the nitrogen of aniline makes *d*-band center of Pt downshift to −2.465 eV, which is close to that of Pt (111) (−2.687 eV). Moreover, the DOS near the Fermi level of Pt in the Pt SASs/AG catalyst was comparable to that of Pt (111), ultimately enhancing HER activity. Furthermore, non-noble metals such as transition metals have emerged as efficient HER catalysts, with some metal-free catalysts exhibiting excellent performance. For instance, Fung et al. screened 3D, 4D, and 5D transition metal SACs in N-doped 2D graphene and nanographene of various sizes using first-principles DFT calculations [264]. They observed a downshift in the d-band center of

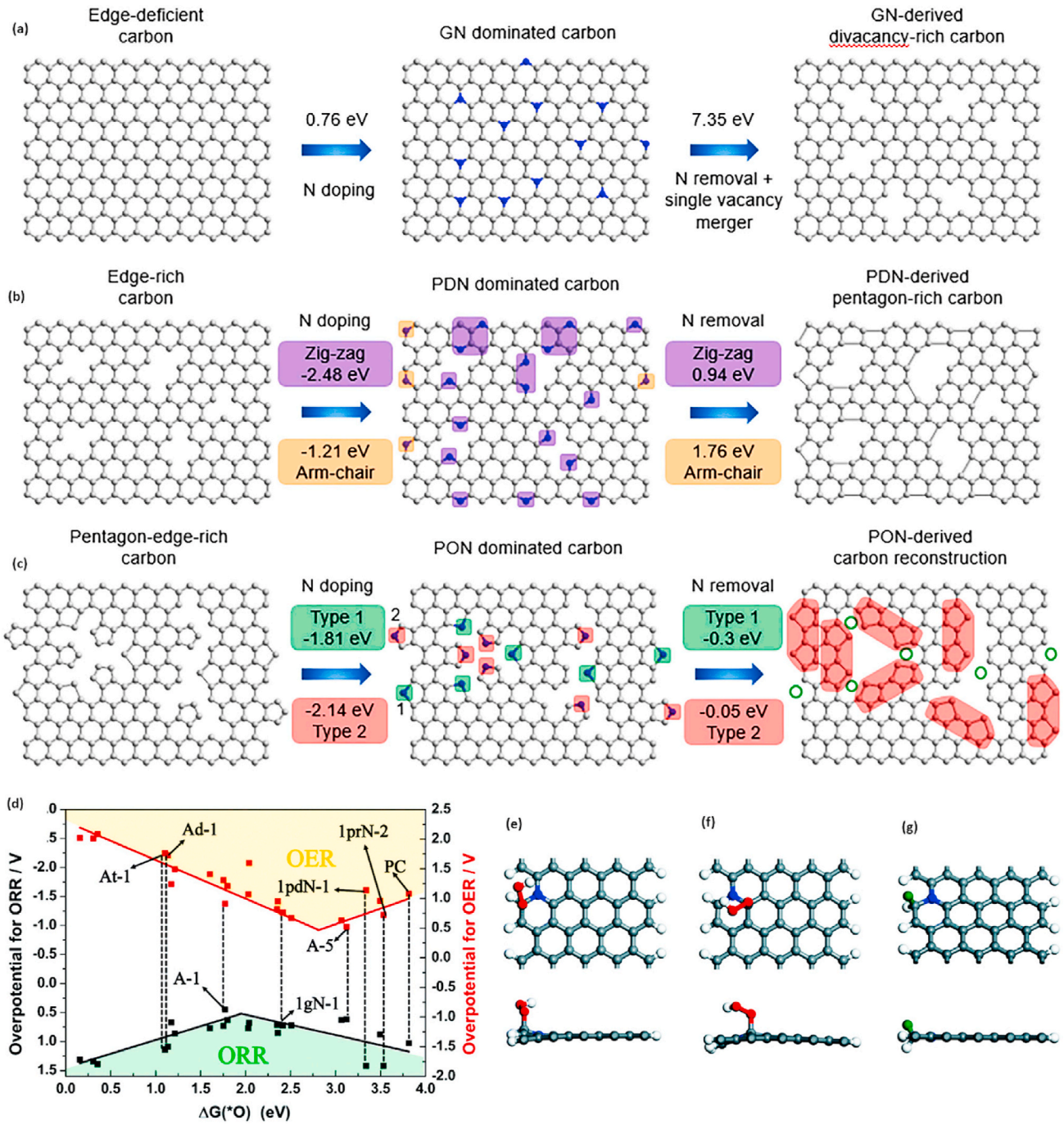

Fig. 20. Computational simulation of specific N-doping and removing process in different carbon models; **(a)** Schematic and formation energy calculation of transformation from edge-deficient carbon to GN-dominated carbon and then to divacancy-rich carbon; **(b)** Schematic and formation energy calculations of transformation from edge-rich carbon to PDN-dominated carbon and then to pentagon-rich carbon; **(c)** Schematic and formation energy calculations of transformation from pentagon-edge-rich carbon to PON-dominated carbon and then to special carbon reconstruction. Adapted from Ref. [261] Copyright 2020, Elsevier B. V. **(d)** The volcano plot for the ORR and OER by plotting the overpotential as a function of ΔG(*O) at various possible active sites. The top and side views of the active site **(e)** A-1 for the ORR, **(f)** A-3 for the OER with OOH adsorbed, and **(g)** A-1 for the HER; the green ball represents the adsorbed H (θ = 2.27 %). Adapted from Ref. [262] Copyright 2019, The Royal Society of Chemistry.

most SACs when transitioning from graphene to nanographene, indicating tunable hydrogen adsorption on metal SACs by adjusting substrate size and dimension. Notably, V, Rh, and Ir embedded in N-doped nanographene exhibited superior HER activity compared to those on extended 2D graphene (Fig. 21a–d) [264]. Additionally, topological defect-based and complex defect-based carbon materials have shown promise as electrocatalysts. Yao and co-workers synthesized defective carbons via a facile nitrogen removal procedure from N-doped graphene, with the edge-defect model termed 7557-4 demonstrating outstanding HER performance with a low calculated free energy of 0.187 eV (Fig. 21e and f) [264]. DFT calculations provided insights into the underlying catalytic mechanisms, revealing that the catalytic activity of edge atoms correlates with their contribution to the highest occupied molecular orbital (HOMO) and lowest unoccupied molecular orbital (LUMO), critical for catalytic reactions (Fig. 21g and h).

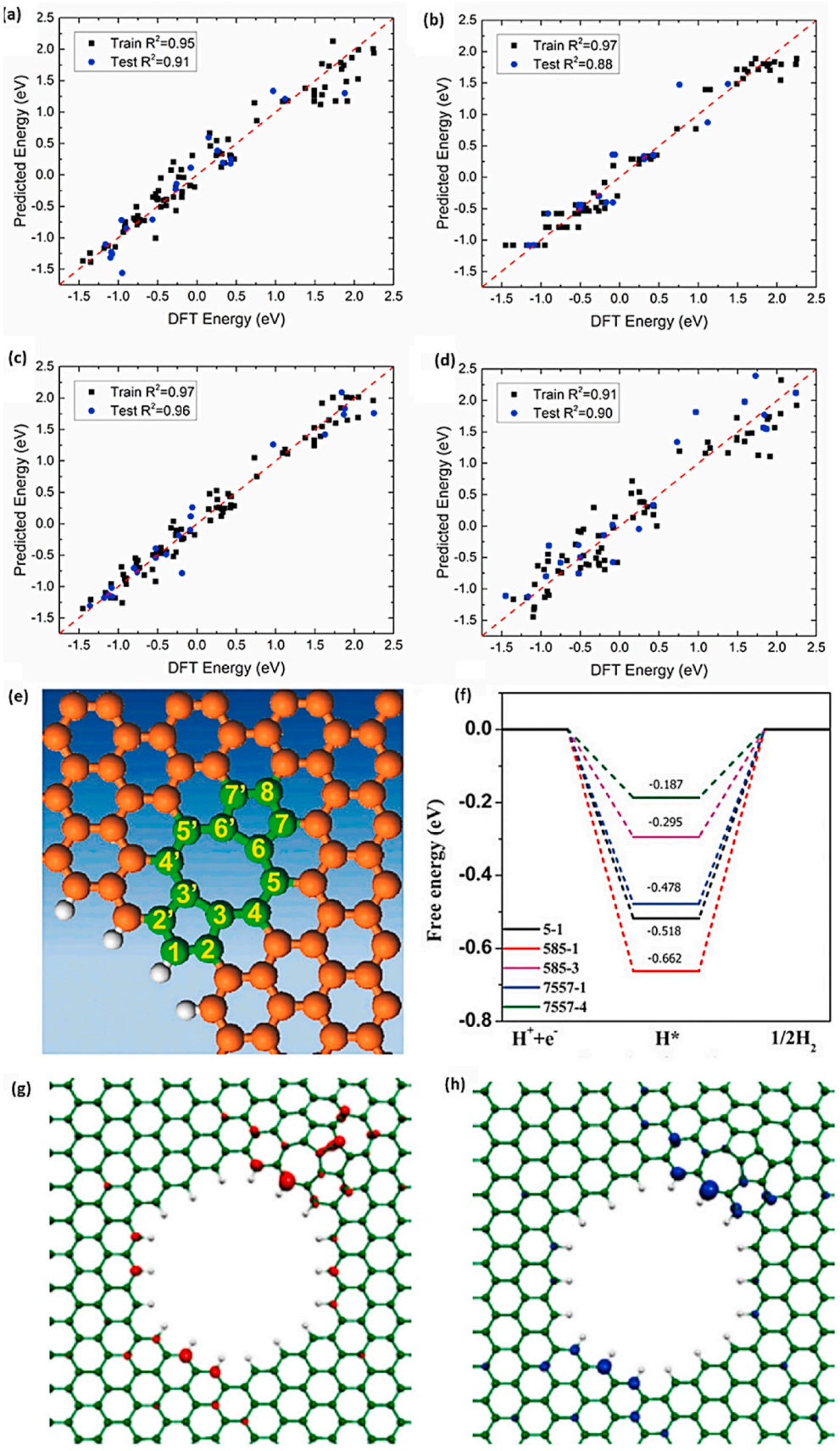

Fig. 21. Comparison of DFT-calculated versus machine learning-predicted ΔGH using: **(a)** kernel ridge regression; **(b)** random forest regression; **(c)** neural network regression, and **(d)** SISSO regression. Adapted from Ref. [264] Copyright 2020, American Chemical Society. **(e)** Mechanism study model of 7557 defects; **(f)** Schematic energy profiles for the HER pathway; **(g)** HOMO and **(h)** LUMO orbitals for 7557 defects. Adapted from Ref. [265] Copyright 2016, John Wiley & Sons, Ltd.

5.3. CO_2 reduction reaction

The initial step in the CO_2RR involves CO_2 adsorption, a pivotal stage in determining the efficiency of CO_2 conversion. Zhu et al. conducted a systematic investigation into CO_2 adsorption on the g-C_3N_4 surface using DFT calculations [266]. By analyzing electronic properties such as band gap, density of states, work function, HOMO, and LUMO, they identified that the two coordinated nitrogen atoms, contributing to both valence and conduction band edges, exhibited the most negative adsorption energy (−0.4181 eV) for CO_2 molecules. This suggests effective capture and activation of CO_2 on Si due to electron acceptance and back-donation between Si dopants and CO_2 molecules. Building on this understanding, Mao and collaborators designed an experimentally synthesizable electrocatalyst termed silicon-doped graphene edges (Si chain@G) [267]. They thoroughly investigated the catalytic performance of Si@ZZG (Si atoms doped into the zigzag edge of graphene) and Si@ACG (Si atoms doped into the armchair edge of graphene) through DFT calculations (Fig. 22a). Both configurations demonstrated efficient CO_2 capture and activation, with binding energies of −0.65 eV and −0.83 eV at the zigzag and armchair edges, respectively. Notably, when Si@ACG served as the active site, effective conversion of CO_2 to CH_3OH was observed. Moreover, Si chain@G with multiple Si active sites, conducive to producing multiple-carbon products, was also investigated. The Si chain@ZZG exhibited high selectivity in converting CO_2 to C_2H_5OH, with an extremely low limiting potential of −0.6 V under the optimal theoretical reaction pathway (Fig. 22b and c).

Transition metal atoms have emerged as promising active centers for the CO_2RR. Guo et al. developed calculation models featuring single Fe, Co, and Ni atoms embedded onto graphitic carbon nitride (Fe/Co/Ni-C_3N_4) and conducted a comprehensive investigation into the structures of the electrocatalysts, CO_2 adsorption configurations, and reduction mechanisms [268]. Utilizing g-C_3N_4 with sixfold cavities as the substrate, the study positioned Ni, Co, and Fe atoms from the corner to the center of the cavity. Analysis of Partial Density of States (PDOS) revealed that CO_2 could undergo chemical adsorption on Co-C_3N_4 and Fe-C_3N_4, whereas it was physically adsorbed on Ni-C_3N_4. Further probing into the reaction pathway and mechanism of various C1 products, Guo et al. calculated the limiting potentials for the production of CO, HCOOH, CH_3OH, and CH_4. They observed that Co-C_3N_4 exhibited superior CO_2RR activity and selectivity for CH_3OH production. Additionally, Cu has emerged as a highly effective catalyst for achieving high activity in reducing CO_2 to hydrocarbons due to its ability to effectively collect *CO_2 and *COOH [269]. Other metals such as Pb, Hg, Cd, and Bi have also demonstrated good catalytic performance in producing formate through the hydration of non-adsorbing CO_2 molecules [270]. However, transition metals like Ni, Fe, Pd, and Ti exhibit low CO_2RR selectivity due to the more favorable HER owing to strong H-bonding [271].

6. Optimizing the objective of energy conversion

6.1. Cost of material production

Graphene: While CVD methods for material synthesis are expensive, exploring alternative approaches, such as the reduction of graphene oxide or employing mechanical exfoliation techniques, might offer a more cost-effective solution [272,273].

MoS_2: The production expenses are influenced by factors such as the desired purity level and volume of production. While hydrothermal synthesis is an economical option for large-scale manufacturing, it may not achieve the same quality level as that produced by CVD [274].

Hexagonal boron nitride: The method of synthesizing this material is similar to that of graphene. Although it does not function as a catalyst independently, it serves as a foundation for the catalytic actions of

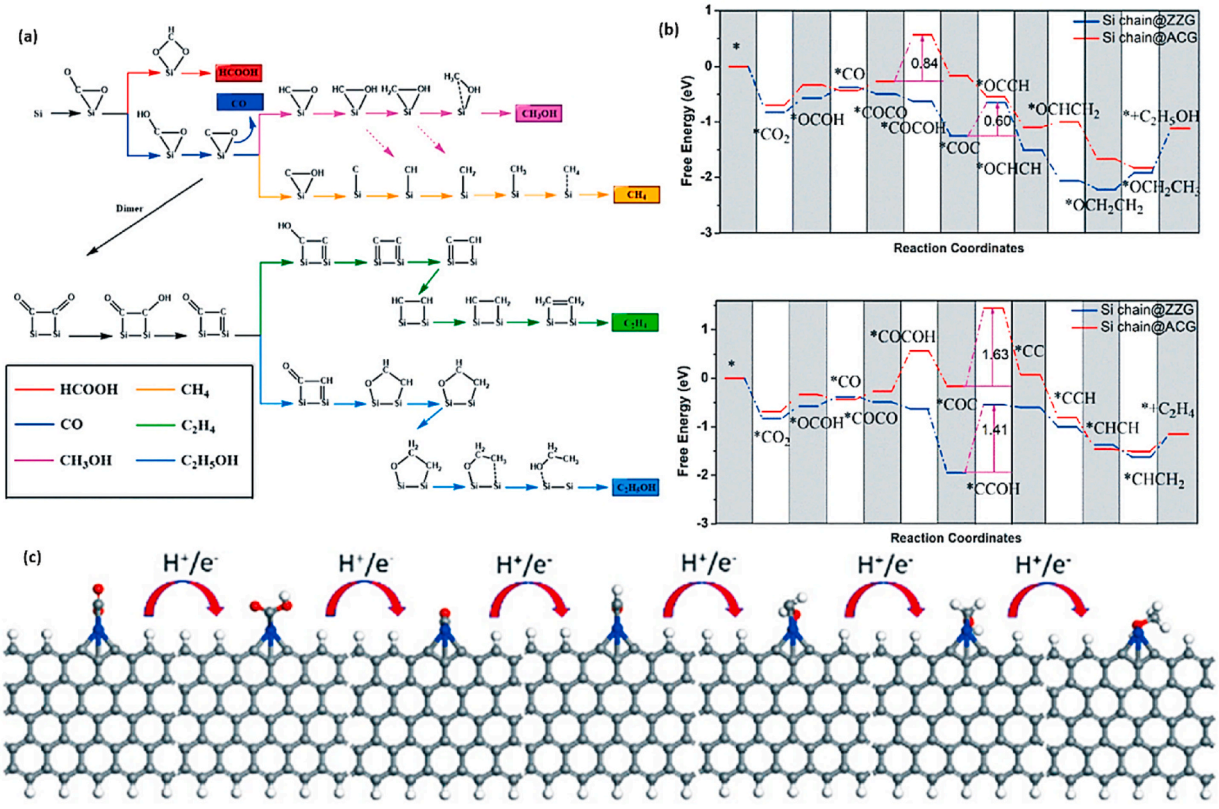

Fig. 22. (a) Possible reaction pathways for the electrocatalytic reduction of CO_2 to six different products; **(b)** Gibbs free energy diagrams of CO_2 reduction reactions to CH_3OH and C_2H_4 on Si chain@ZZG and Si chain@ACG; **(c)** The optimized structures for CO_2 reduction to CH_3OH on the zigzag edge. Adapted from Ref. [267] Copyright 2019, The Royal Society of Chemistry.

metallic nanoparticles. The cost of this approach depends on the performance efficiency of the nanoparticle-enhanced catalyst system [275].

Transition Metal Dichalcogenides: While materials such as WS_2 or WSe_2 can be synthesized using techniques similar to MoS_2, they might be more expensive owing to the relative scarcity of their raw materials [276].

6.2. Performance efficiency

Phosphorene (Black Phosphorus) demonstrates notable potential in the ORR, OER, and HER, owing to its distinct puckered structural arrangement. However, its rapid degradation under normal environmental conditions poses a significant challenge for its industrial use. The development of effective stabilization methods is crucial for overcoming this limitation [8,277].

TMDs: The catalytic effectiveness of TMDs varies among different types. For instance, WS_2 may exhibit superior performance compared with MoS_2 for specific applications. A thorough economic analysis would entail evaluating cost-effectiveness based on the specific catalytic activity of each material [278].

6.3. Energy requirements

TMDs: These materials commonly require reduced overpotentials for the HER when juxtaposed with platinum, indicating a potential decrease in the energy required for hydrogen generation. However, to confirm these efficiencies, their operational stability must be demonstrated effectively at an industrial scale [279].

6.4. Market demand

There is an increasing market demand for advanced energy storage and conversion solutions, underscoring the necessity for effective and durable catalysts. 2D materials, notably TMDs and MXenes, are gaining attention for their potential applications beyond electrocatalysis, including in lithium-ion batteries and supercapacitors [280].

MXenes: MXenes stand out with their impressive conductivity and customizable surface attributes, positioning them for unique electrocatalytic applications. However, their long-term stability remains a subject of ongoing research, which is crucial for their commercial viability.

6.5. Regulatory and environmental considerations

In the realm of materials production, those that exhibit a minimal carbon footprint or contribute to the generation of clean energy may garner support and incentives from governmental and regulatory entities. This scenario could favor certain 2D materials, particularly if they align with environmental sustainability criteria set by these bodies.

6.6. Competing technologies

MXenes' performance in electrocatalysis shows promise of exceeding that of existing 2D materials in terms of efficiency. Nevertheless, a significant challenge lies in their elevated production costs. To position MXenes as a competitive option in the market, advancements in synthesis techniques are necessary to reduce these costs. In contrast, TMDs may offer distinct advantages over graphene for certain electrocatalytic processes. This is attributed to their inherent semiconducting qualities, which could prove more advantageous for specific types of redox reactions.

6.7. Investment and ROI

The valuation of the return on investment (ROI) for 2D materials in the field of electrocatalysis should include an analysis of financial benefits arising from increased catalyst durability, lower frequency of maintenance requirements, and reduced operational downtime. Specifically, MXenes could offer substantial value over traditional catalysts used in industrial settings by demonstrating superior longevity, thereby potentially offsetting their greater initial costs. Furthermore, a comprehensive economic evaluation of these 2D materials must account for their capability to facilitate innovative electrochemical processes or enhance existing ones. This could lead to the emergence of new market opportunities or expansion within current market segments. Critical factors such as unique cost structures, scalability prospects, performance indices, and specific market demands for each 2D material must be thoroughly examined to ascertain their financial feasibility for industrial application purposes.

7. Summary and future prospects

In summary, this review highlights the promising capabilities of 2D materials as proficient electrocatalysts for OER, HER, and CO_2RR. The exploration of various strategies highlights the pivotal role of defect engineering in tailoring the 2D materials' electronic and catalytic properties, thereby boosting their overall electrocatalytic performance. Furthermore, nonmetal and metal doping have emerged as viable approaches for enhancing catalytic performance, opening exciting avenues for future research and development. In the context of the OER and HER, phase and interface engineering show significant potential for optimizing the active sites and reaction kinetics of 2D materials. Heteroatom doping offers potential improvements in hydrogen evolution efficiency and selectivity. Concerning RR, strategies involving surface modification and surface-structure tuning demonstrate remarkable potential in governing the reaction selectivity and activity, yielding carbon dioxide conversion into valuable products. Similarly, the successful optimization of the electrolyte composition and electrolyzer design has emerged as a crucial factor in achieving overall CO_2RR efficiency, motivating further exploration of advanced catalytic systems. *In principle*, this review highlights the significant potential of 2D materials as robust electrocatalysts for diverse energy-conversion reactions. By leveraging innovative strategies and capitalizing on their unique properties, two-dimensional materials are anticipated to play a pivotal role in shaping a sustainable and clean energy future.

Looking ahead, electrocatalysis using two-dimensional materials holds great promise and numerous opportunities for further exploration. Researchers should aim to develop a fundamental consideration of structure-activity relationships, permitting the precise model of 2D materials with adapted properties for actual electrocatalytic applications.

(i) ***Advanced Characterization Techniques*:** Developing sophisticated characterization approaches, e.g., in situ spectroscopy and microscopy, will be crucial in unraveling intricate electrocatalytic processes at the nanoscale. These techniques provide real-time insights into active sites, reaction intermediates, and surface interactions, enabling researchers to optimize the design of two-dimensional materials with enhanced catalytic properties.

(ii) ***Tailored Heterostructures:*** The exploration of tailored heterostructures comprising different 2D materials has immense potential for synergistically combining their unique properties to achieve superior catalytic activity. Researchers should investigate novel synthetic methods and carefully engineer interfaces to maximize the performance of such heterostructures in electrocatalytic reactions.

(iii) ***Beyond Single-Element Doping:*** While nonmetal and metal doping has shown promise in enhancing catalytic activity, future research should investigate more complex doping strategies involving multiple elements. This approach can lead to new catalysts with finely tuned electronic structures, affording higher efficiency and selectivity in energy-conversion processes.

(iv) ***The Role of Defects:*** Further investigations into the role of defects in 2D materials are essential, as their controlled introduction or elimination can significantly impact electrocatalytic performance. Understanding defect-engineering mechanisms will enable the precise tuning of defect concentrations for optimal catalytic activity.

(v) ***Integration into Commercial Devices:*** Bridging the gap among fundamental research and real applications is vital for the widely adopting two dimensional material-based electrocatalysts. Collaboration between industry partners and engineers should be encouraged to develop scalable and commercially viable electrochemical devices that influence the benefits of 2D materials.

(vi) ***Environmental Impact and Cost-effectiveness:*** As field progresses, researchers should be mindful of the ecological impact of synthesizing 2D materials and the scalability of production methods. Sustainable and cost-effective synthetic routes should be pursued to ensure the widespread applicability of these materials.

(vii) ***Incorporating two-dimensional Materials into Renewable Energy Systems:*** The integration of 2D materials into renewable energy sources, i.e., solar cells, batteries, and supercapacitors, should be explored to leverage their unique properties for more effective and feasible energy storing and conversion.

(viii) ***Multifunctional Catalytic Systems:*** Investigating multifunctional catalytic systems that simultaneously perform multiple electrocatalytic reactions, e.g., the OER, HER, and CO_2RR, could lead to more versatile and energy-efficient electrochemical devices.

(ix) ***Beyond Water Splitting and CO_2 Reduction:*** While water splitting and CO_2 reduction are essential for sustainable energy conversion, researchers should explore the potential of two-dimensional materials in other electrocatalytic reactions, such as nitrogen fixation, to address a broader range of environmental and energy challenges.

(x) ***Cross-disciplinary Collaboration:*** Encouraging cross-disciplinary collaborations with researchers from diverse fields, including materials science, chemistry, physics, engineering, and environmental science, will foster innovative ideas and accelerate progress in developing efficient two-dimensional material-based electrocatalysts.

In summary, the future of 2D materials in electrocatalysis is promising, with exciting possibilities for addressing global energy and environmental tasks. By focusing on advanced characterization techniques, tailored heterostructures, and innovative doping strategies, researchers can unlock the potential of 2D materials in sustainable energy-conversion technologies. Collaborative efforts with industry and a strong emphasis on environmental sustainability and cost-effectiveness are vital in driving the transition from laboratory discoveries to practical applications in the real world (see Fig. 23).

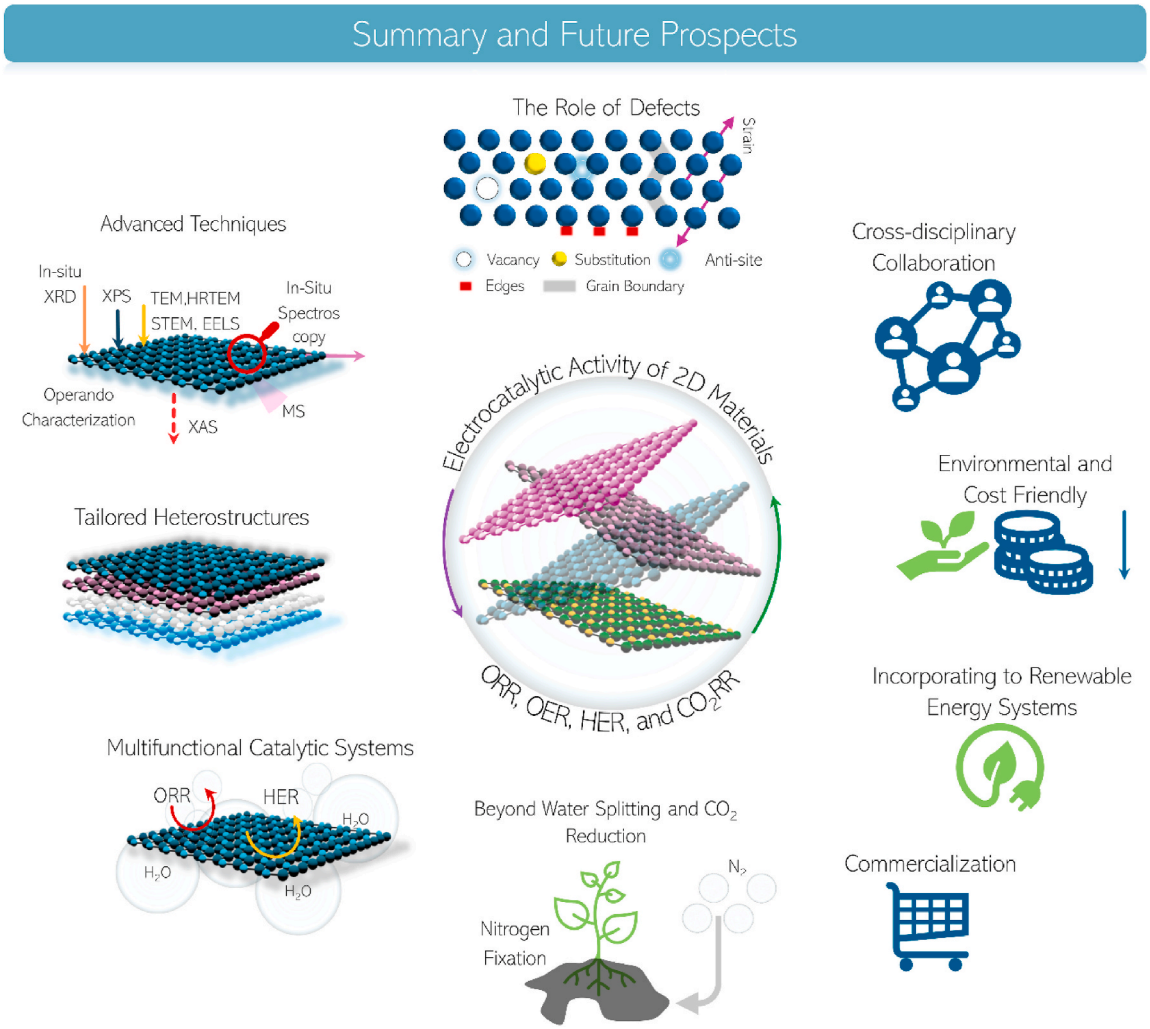

Fig. 23. Pictorial representation of summary and future prospects.

CRediT authorship contribution statement

Ali Raza: Data curation, Conceptualization. **Jahan Zeb Hassan:** Resources, Methodology. **Usman Qumar:** Formal analysis. **Ayesha Zaheer:** Validation. **Zaheer Ud Din Babar:** Writing – original draft. **Vincenzo Iannotti:** Writing – review & editing. **Antonio Cassinese:** Writing – review & editing.

Declaration of competing interest

The authors declare that they have no known competing financial interests or personal relationships that could have appeared to influence the work reported in this paper.

Data availability

No data was used for the research described in the article.

Acknowledgment

The authors are thankful to all individuals and organizations who provided permission to republish their figures and other relevant information.

References

[1] H. Wang, X. Liu, P. Niu, S. Wang, J. Shi, L. Li, Porous two-dimensional materials for photocatalytic and electrocatalytic applications, Matter 2 (2020) 1377–1413.
[2] H. Zhang, Introduction: 2D materials chemistry, Chem. Rev. 118 (2018) 6089–6090.
[3] X. Cai, Y. Luo, B. Liu, H.-M. Cheng, Preparation of 2D material dispersions and their applications, Chem. Soc. Rev. 47 (2018) 6224–6266.
[4] A. Carella, M. Franzini, S. Fusco, R. Centore, M. Barra, F. Chiarella, A. Cassinese, M. Bonomo, S. Nejrotti, M. Carbone, L. Gontrani, Isoindigo dyes functionalized with terminal electron-withdrawing groups: computational, optical and electrical characterization, Dyes Pigments 208 (2023) 110866.
[5] F. Chianese, A. Candini, S. Lumetti, N. Mishra, C. Coletti, M. Affronte, A. Cassinese, Evaluating the use of graphene electrodes in sub-micrometric, high-frequency n-type organic transistors, Synth. Met. 273 (2021) 116683.
[6] V. Preziosi, M. Barra, V.R. Villella, S. Esposito, P. D'Angelo, S.L. Marasso, M. Cocuzza, A. Cassinese, S. Guido, Immuno-Sensing at ultra-low concentration of TG2 protein by organic electrochemical transistors, in: Biosensors, 2023.
[7] Z. Sun, T. Ma, H. Tao, Q. Fan, B. Han, Fundamentals and challenges of electrochemical CO2 reduction using two-dimensional materials, Chem 3 (2017) 560–587.
[8] X. Chia, M. Pumera, Characteristics and performance of two-dimensional materials for electrocatalysis, Nat. Catal. 1 (2018) 909–921.
[9] X. Bai, J. Guan, MXenes for electrocatalysis applications: modification and hybridization, Chin. J. Catal. 43 (2022) 2057–2090.
[10] F. Banhart, J. Kotakoski, A.V. Krasheninnikov, Structural defects in graphene, ACS Nano 5 (2011) 26–41.
[11] H. Li, C. Tsai, A.L. Koh, L. Cai, A.W. Contryman, A.H. Fragapane, J. Zhao, H. S. Han, H.C. Manoharan, F. Abild-Pedersen, J.K. Nørskov, X. Zheng, Activating and optimizing MoS2 basal planes for hydrogen evolution through the formation of strained sulphur vacancies, Nat. Mater. 15 (2016) 48–53.
[12] X. Wang, X. Li, L. Zhang, Y. Yoon, P.K. Weber, H. Wang, J. Guo, H. Dai, N-doping of graphene through electrothermal reactions with ammonia, Science 324 (2009) 768–771.
[13] X. Zhao, J. Shi, Y. Ji, Y. Liu, The electronic structure underlying electrocatalysis of two-dimensional materials, WIREs Comput. Molec. Sci. 9 (2019) e1418.
[14] M. Chhowalla, H.S. Shin, G. Eda, L.-J. Li, K.P. Loh, H. Zhang, The chemistry of two-dimensional layered transition metal dichalcogenide nanosheets, Nat. Chem. 5 (2013) 263–275.
[15] Z. Li, X. Zhang, H. Cheng, J. Liu, M. Shao, M. Wei, D.G. Evans, H. Zhang, X. Duan, Confined synthesis of 2D nanostructured materials toward electrocatalysis, Adv. Energy Mater. 10 (2020) 1900486.
[16] Q. Shi, X. Wei, A. Raza, G. Li, Recent advances in aerobic photo-oxidation of methanol to valuable chemicals, ChemCatChem 13 (2021) 3381–3395.
[17] T. Sun, G. Zhang, D. Xu, X. Lian, H. Li, W. Chen, C. Su, Defect chemistry in 2D materials for electrocatalysis, Mater. Today Energy 12 (2019) 215–238.
[18] X. Wu, S. Xiao, Y. Long, T. Ma, W. Shao, S. Cao, X. Xiang, L. Ma, L. Qiu, C. Cheng, C. Zhao, Emerging 2D materials for electrocatalytic applications: synthesis, multifaceted nanostructures, and catalytic center design, Small 18 (2022) 2105831.
[19] T. Wu, C. Dong, D. Sun, F. Huang, Enhancing electrocatalytic water splitting by surface defect engineering in two-dimensional electrocatalysts, Nanoscale 13 (2021) 1581–1595.
[20] S. Ali, A. Raza, A.M. Afzal, M.W. Iqbal, M. Hussain, M. Imran, M.A. Assiri, Recent advances in 2D-MXene based nanocomposites for optoelectronics, Adv. Mater. Interfac. 9 (2022) 2200556.
[21] A. Raza, M. Ikram, S. Guo, A. Baiker, G. Li, Green synthesis of dimethyl carbonate from CO2 and methanol: new strategies and industrial perspective, Adv. Sustain. Syst. 6 (2022) 2200087.
[22] A. Raza, X. Zhang, S. Ali, C. Cao, A.A. Rafi, G. Li, Photoelectrochemical energy conversion over 2D materials, in: Photochem, 2022, pp. 272–298.
[23] S. Li, J. Sun, J. Guan, Strategies to improve electrocatalytic and photocatalytic performance of two-dimensional materials for hydrogen evolution reaction, Chin. J. Catal. 42 (2021) 511–556.
[24] T. Tang, Z. Wang, J. Guan, A review of defect engineering in two-dimensional materials for electrocatalytic hydrogen evolution reaction, Chin. J. Catal. 43 (2022) 636–678.
[25] Z. Liu, T. He, Q. Jiang, W. Wang, J. Tang, A review of heteroatomic doped two-dimensional materials as electrocatalysts for hydrogen evolution reaction, Int. J. Hydrogen Energy 47 (2022) 29698–29729.
[26] S. Lu, F. Lou, Z. Yu, Recent progress in two-dimensional materials for electrocatalytic CO2 reduction, Catalysts (2022).
[27] J. Liu, C. Guo, A. Vasileff, S. Qiao, Nanostructured 2D materials: prospective catalysts for electrochemical CO2 reduction, Small Methods 1 (2017) 1600006.
[28] W. Zhai, Y. Chen, Y. Liu, T. Sakthivel, Y. Ma, Y. Qin, Y. Qu, Z. Dai, Enlarging the Ni–O bond polarizability in a phosphorene-hosted metal–organic framework for boosted water oxidation electrocatalysis, ACS Nano 17 (2023) 17254–17264.
[29] W. Zhai, Y. Chen, Y. Liu, T. Sakthivel, Y. Ma, S. Guo, Y. Qu, Z. Dai, Bimetal-incorporated black phosphorene with surface electron deficiency for efficient anti-reconstruction water electrolysis, Adv. Funct. Mater. 33 (2023) 2301565.
[30] J. Cheng, S. Ran, T. Li, M. Yan, J. Wu, S. Boles, B. Liu, H. Raza, S. Ullah, W. Zhang, G. Chen, G. Zheng, Achieving superior tensile performance in individual Metal−Organic framework crystals, Adv. Mater. 35 (2023) 2210829.
[31] J. Cheng, K. Liu, X. Li, L. Huang, J. Liang, G. Zheng, G. Shan, Nickel-metal-organic framework nanobelt based composite membranes for efficient Sr2+ removal from aqueous solution, Environ. Sci. Ecotechnol. 3 (2020) 100035.
[32] K.S. Novoselov, A.K. Geim, S.V. Morozov, D. Jiang, Y. Zhang, S.V. Dubonos, I. V. Grigorieva, A.A. Firsov, Electric field effect in atomically thin carbon films, Science 306 (2004) 666–669.
[33] J.Z. Hassan, A. Raza, Z.U. Din Babar, U. Qumar, N.T. Kaner, A. Cassinese, 2D material-based sensing devices: an update, J. Mater. Chem. A 11 (2023) 6016–6063.
[34] A. Raza, A. Rafiq, U. Qumar, J.Z. Hassan, 2D hybrid photocatalysts for solar energy harvesting, Sustain. Mater. Technol. 33 (2022) e00469.
[35] A.H. Khan, S. Ghosh, B. Pradhan, A. Dalui, L.K. Shrestha, S. Acharya, K. Ariga, Two-dimensional (2D) nanomaterials towards electrochemical nanoarchitectonics in energy-related applications, Bull. Chem. Soc. Jpn. 90 (2017) 627–648.
[36] Q. Yu, Y. Luo, A. Mahmood, B. Liu, H.-M. Cheng, Engineering two-dimensional materials and their heterostructures as high-performance electrocatalysts, Electrochem. Energy Rev. 2 (2019) 373–394.
[37] Z.W. Seh, J. Kibsgaard, C.F. Dickens, I. Chorkendorff, J.K. Nørskov, T. F. Jaramillo, Combining theory and experiment in electrocatalysis: insights into materials design, Science 355 (2017) eaad4998.
[38] D. Higgins, P. Zamani, A. Yu, Z. Chen, The application of graphene and its composites in oxygen reduction electrocatalysis: a perspective and review of recent progress, Energy Environ. Sci. 9 (2016) 357–390.
[39] M. Shao, Q. Chang, J.-P. Dodelet, R. Chenitz, Recent advances in electrocatalysts for oxygen reduction reaction, Chem. Rev. 116 (2016) 3594–3657.
[40] J. Stacy, Y.N. Regmi, B. Leonard, M. Fan, The recent progress and future of oxygen reduction reaction catalysis: a review, Renew. Sustain. Energy Rev. 69 (2017) 401–414.
[41] V.T.T. Ho, C.-J. Pan, J. Rick, W.-N. Su, B.-J. Hwang, Nanostructured Ti0.7Mo0.3O2 support enhances electron transfer to Pt: high-performance catalyst for oxygen reduction reaction, J. Am. Chem. Soc. 133 (2011) 11716–11724.
[42] H. Yu, L. Shang, T. Bian, R. Shi, G.I.N. Waterhouse, Y. Zhao, C. Zhou, L.-Z. Wu, C.-H. Tung, T. Zhang, Nitrogen-doped porous carbon nanosheets templated from g-C3N4 as metal-free electrocatalysts for efficient oxygen reduction reaction, Adv. Mater. 28 (2016) 5080–5086.
[43] Y. Liu, S. Shrestha, W.E. Mustain, Synthesis of nanosize tungsten oxide and its evaluation as an electrocatalyst support for oxygen reduction in acid media, ACS Catal. 2 (2012) 456–463.
[44] K. Zhao, W. Gu, L. Zhao, C. Zhang, W. Peng, Y. Xian, MoS2/Nitrogen-doped graphene as efficient electrocatalyst for oxygen reduction reaction, Electrochim. Acta 169 (2015) 142–149.
[45] S. Javaid, X. Xu, W. Chen, J. Chen, H.-Y. Hsu, S. Wang, X. Yang, Y. Li, Z. Shao, F. Jones, G. Jia, Ni2+/Co2+ doped Au-Fe7S8 nanoplatelets with exceptionally high oxygen evolution reaction activity, Nano Energy 89 (2021) 106463.
[46] H. Wang, W. Wang, H. Yu, Q. Mao, Y. Xu, X. Li, Z. Wang, L. Wang, Interface engineering of polyaniline-functionalized porous Pd metallene for alkaline oxygen reduction reaction, Appl. Catal. B Environ. 307 (2022) 121172.
[47] S. Mao, Z. Wen, T. Huang, Y. Hou, J. Chen, High-performance bi-functional electrocatalysts of 3D crumpled graphene–cobalt oxide nanohybrids for oxygen reduction and evolution reactions, Energy Environ. Sci. 7 (2014) 609–616.
[48] S. Chen, S.-Z. Qiao, Hierarchically porous nitrogen-doped graphene–NiCo2O4 hybrid paper as an advanced electrocatalytic water-splitting material, ACS Nano 7 (2013) 10190–10196.

[49] S. Chen, J. Duan, J. Ran, S.-Z. Qiao, Paper-based N-doped carbon films for enhanced oxygen evolution electrocatalysis, Adv. Sci. 2 (2015) 1400015.
[50] T.Y. Ma, S. Dai, M. Jaroniec, S.Z. Qiao, Graphitic carbon nitride nanosheet–carbon nanotube three-dimensional porous composites as high-performance oxygen evolution electrocatalysts, Angew. Chem. Int. Ed. 53 (2014) 7281–7285.
[51] S. Chen, J. Duan, M. Jaroniec, S.-Z. Qiao, Nitrogen and oxygen dual-doped carbon hydrogel film as a substrate-free electrode for highly efficient oxygen evolution reaction, Adv. Mater. 26 (2014) 2925–2930.
[52] M. Yu, J. Zheng, M. Guo, La-doped NiFe-LDH coupled with hierarchical vertically aligned MXene frameworks for efficient overall water splitting, J. Energy Chem. 70 (2022) 472–479.
[53] H. Sun, J.-G. Li, L. Lv, Z. Li, X. Ao, C. Xu, X. Xue, G. Hong, C. Wang, Engineering hierarchical CoSe/NiFe layered-double-hydroxide nanoarrays as high efficient bifunctional electrocatalyst for overall water splitting, J. Power Sources 425 (2019) 138–146.
[54] Y. Zhang, H. Jiang, Y. Lin, H. Liu, Q. He, C. Wu, T. Duan, L. Song, In situ growth of cobalt nanoparticles encapsulated nitrogen-doped carbon nanotubes among Ti3C2Tx (MXene) matrix for oxygen reduction and evolution, Adv. Mater. Interfac. 5 (2018) 1800392.
[55] Q. Wang, L. Shang, R. Shi, X. Zhang, Y. Zhao, G.I.N. Waterhouse, L.-Z. Wu, C.-H. Tung, T. Zhang, NiFe layered double hydroxide nanoparticles on Co,N-codoped carbon nanoframes as efficient bifunctional catalysts for rechargeable zinc–air batteries, Adv. Energy Mater. 7 (2017) 1700467.
[56] L. Zhao, B. Dong, S. Li, L. Zhou, L. Lai, Z. Wang, S. Zhao, M. Han, K. Gao, M. Lu, X. Xie, B. Chen, Z. Liu, X. Wang, H. Zhang, H. Li, J. Liu, H. Zhang, X. Huang, W. Huang, Interdiffusion reaction-assisted hybridization of two-dimensional metal–organic frameworks and Ti3C2Tx nanosheets for electrocatalytic oxygen evolution, ACS Nano 11 (2017) 5800–5807.
[57] L. Xiu, Z. Wang, M. Yu, X. Wu, J. Qiu, Aggregation-resistant 3D MXene-based architecture as efficient bifunctional electrocatalyst for overall water splitting, ACS Nano 12 (2018) 8017–8028.
[58] S.K. Bikkarolla, P. Papakonstantinou, CuCo2O4 nanoparticles on nitrogenated graphene as highly efficient oxygen evolution catalyst, J. Power Sources 281 (2015) 243–251.
[59] Y. Guo, J. Tang, H. Qian, Z. Wang, Y. Yamauchi, One-pot synthesis of zeolitic imidazolate framework 67-derived hollow Co3S4@MoS2 heterostructures as efficient bifunctional catalysts, Chem. Mater. 29 (2017) 5566–5573.
[60] C. Wang, L. Ma, L. Liao, S. Bai, R. Long, M. Zuo, Y. Xiong, A unique platinum-graphene hybrid structure for high activity and durability in oxygen reduction reaction, Sci. Rep. 3 (2013) 2580.
[61] T. Li, J. Liu, Y. Song, F. Wang, Photochemical solid-phase synthesis of platinum single atoms on nitrogen-doped carbon with high loading as bifunctional catalysts for hydrogen evolution and oxygen reduction reactions, ACS Catal. 8 (2018) 8450–8458.
[62] L. Liu, H. Su, F. Tang, X. Zhao, Q. Liu, Confined organometallic Au1Nx single-site as an efficient bifunctional oxygen electrocatalyst, Nano Energy 46 (2018) 110–116.
[63] J. Liu, M. Jiao, L. Lu, H.M. Barkholtz, Y. Li, Y. Wang, L. Jiang, Z. Wu, D.-j. Liu, L. Zhuang, C. Ma, J. Zeng, B. Zhang, D. Su, P. Song, W. Xing, W. Xu, Y. Wang, Z. Jiang, G. Sun, High performance platinum single atom electrocatalyst for oxygen reduction reaction, Nat. Commun. 8 (2017) 15938.
[64] C. Zhang, J. Sha, H. Fei, M. Liu, S. Yazdi, J. Zhang, Q. Zhong, X. Zou, N. Zhao, H. Yu, Z. Jiang, E. Ringe, B.I. Yakobson, J. Dong, D. Chen, J.M. Tour, Single-atomic ruthenium catalytic sites on nitrogen-doped graphene for oxygen reduction reaction in acidic medium, ACS Nano 11 (2017) 6930–6941.
[65] C. Delacôte, A. Bonakdarpour, C.M. Johnston, P. Zelenay, A. Wieckowski, Aqueous-based synthesis of ruthenium–selenium catalyst for oxygen reduction reaction, Faraday Discuss 140 (2009) 269–281.
[66] H.T. Chung, J.H. Won, P. Zelenay, Active and stable carbon nanotube/nanoparticle composite electrocatalyst for oxygen reduction, Nat. Commun. 4 (2013) 1922.
[67] K. Gong, F. Du, Z. Xia, M. Durstock, L. Dai, Nitrogen-Doped Carbon Nanotube Arrays with High Electrocatalytic Activity for Oxygen Reduction, vol. 323, 2009, pp. 760–764.
[68] M. Xiao, L. Gao, Y. Wang, X. Wang, J. Zhu, Z. Jin, C. Liu, H. Chen, G. Li, J. Ge, Q. He, Z. Wu, Z. Chen, W. Xing, Engineering energy level of metal center: Ru single-atom site for efficient and durable oxygen reduction catalysis, J. Am. Chem. Soc. 141 (2019) 19800–19806.
[69] M. Xiao, J. Zhu, G. Li, N. Li, S. Li, Z.P. Cano, L. Ma, P. Cui, P. Xu, G. Jiang, H. Jin, S. Wang, T. Wu, J. Lu, A. Yu, D. Su, Z. Chen, A Single-Atom Iridium Heterogeneous Catalyst in Oxygen Reduction Reaction, vol. 58, 2019, pp. 9640–9645.
[70] W. Ai, Z. Luo, J. Jiang, J. Zhu, Z. Du, Z. Fan, L. Xie, H. Zhang, W. Huang, T. Yu, Nitrogen and Sulfur Codoped Graphene: Multifunctional Electrode Materials for High-Performance Li-Ion Batteries and Oxygen Reduction Reaction, vol. 26, 2014, pp. 6186–6192.
[71] H. Fei, R. Ye, G. Ye, Y. Gong, Z. Peng, X. Fan, E.L.G. Samuel, P.M. Ajayan, J. M. Tour, Boron- and nitrogen-doped graphene quantum dots/graphene hybrid nanoplatelets as efficient electrocatalysts for oxygen reduction, ACS Nano 8 (2014) 10837–10843.
[72] W. Lei, Y.-P. Deng, G. Li, Z.P. Cano, X. Wang, D. Luo, Y. Liu, D. Wang, Z. Chen, Two-dimensional phosphorus-doped carbon nanosheets with tunable porosity for oxygen reactions in zinc-air batteries, ACS Catal. 8 (2018) 2464–2472.
[73] T. Sun, J. Wang, C. Qiu, X. Ling, B. Tian, W. Chen, C. Su, B, N codoped and defect-rich nanocarbon material as a metal-free bifunctional electrocatalyst for oxygen reduction and, Evol. Reactions 5 (2018) 1800036.
[74] J. Li, Y. Zhang, X. Zhang, J. Huang, J. Han, Z. Zhang, X. Han, P. Xu, B. Song, S, N dual-doped graphene-like carbon nanosheets as efficient oxygen reduction reaction electrocatalysts, ACS Appl. Mater. Interfaces 9 (2017) 398–405.
[75] P. Marbaniang, S. Ingavale, D. Catherin, N. Ramgir, A. Swami, B. Kakade, Forming a BB bond in boron carbon nitride composite: a way for metal free electrocatalyst for oxygen reduction reaction in alkaline medium, J. Catal. 378 (2019) 104–112.
[76] I.M. Patil, A. Swami, R. Chavan, M. Lokanathan, B. Kakade, Hexagonal boron nitride-supported crystalline manganese oxide nanorods/carbon: a tunable nanocomposite catalyst for dioxygen electroreduction, ACS Sustain. Chem. Eng. 6 (2018) 16886–16895.
[77] W. Wang, X. Wang, Y. Wang, B. Jiang, H. Song, Fabrication of Co, N-doping hierarchical porous graphene from metal organic framework for oxygen reduction reaction in microbial fuel cell, J. Electrochem. Soc. 169 (2022) 024501.
[78] R.G. González-Huerta, J.A. Chávez-Carvayar, O. Solorza-Feria, Electrocatalysis of oxygen reduction on carbon supported Ru-based catalysts in a polymer electrolyte fuel cell, J. Power Sources 153 (2006) 11–17.
[79] H. Zhang, R. Lv, Defect engineering of two-dimensional materials for efficient electrocatalysis, J. Materiom. 4 (2018) 95–107.
[80] J. Qi, W. Wang, Y. Li, Y. Sun, Z. Wu, K. Bao, L. Wang, R. Ye, M. Ding, Q. He, On-chip investigation of electrocatalytic oxygen reduction reaction of 2D materials, Small 18 (2022) 2204010.
[81] L. Lin, N. Miao, G.G. Wallace, J. Chen, D.A. Allwood, Engineering carbon materials for electrochemical oxygen reduction reactions, Adv. Energy Mater. 11 (2021) 2100695.
[82] S. Chen, Z. Kang, X. Hu, X. Zhang, H. Wang, J. Xie, X. Zheng, W. Yan, B. Pan, Y. Xie, Delocalized spin states in 2D atomic layers realizing enhanced electrocatalytic oxygen evolution, Adv. Mater. 29 (2017) 1701687.
[83] S. Du, Z. Ren, Y. Qu, J. Wu, W. Xi, J. Zhu, H. Fu, Co3O4 nanosheets as a high-performance catalyst for oxygen evolution proceeding via a double two-electron process, Chem. Commun. 52 (2016) 6705–6708.
[84] R. Gao, H. Zhang, D. Yan, Iron diselenide nanoplatelets: stable and efficient water-electrolysis catalysts, Nano Energy 31 (2017) 90–95.
[85] B. Weng, F. Xu, C. Wang, W. Meng, C.R. Grice, Y. Yan, A layered Na1−xNiyFe1−yO2 double oxide oxygen evolution reaction electrocatalyst for highly efficient water-splitting, Energy Environ. Sci. 10 (2017) 121–128.
[86] S.M. Pawar, B.S. Pawar, B. Hou, J. Kim, A.T. Aqueel Ahmed, H.S. Chavan, Y. Jo, S. Cho, A.I. Inamdar, J.L. Gunjakar, H. Kim, S. Cha, H. Im, Self-assembled two-dimensional copper oxide nanosheet bundles as an efficient oxygen evolution reaction (OER) electrocatalyst for water splitting applications, J. Mater. Chem. A 5 (2017) 12747–12751.
[87] Y. Xue, Z. Ren, Y. Xie, S. Du, J. Wu, H. Meng, H. Fu, CoSex nanocrystalline-dotted CoCo layered double hydroxide nanosheets: a synergetic engineering process for enhanced electrocatalytic water oxidation, Nanoscale 9 (2017) 16256–16263.
[88] X. Kong, Y. Huang, Q. Liu, Two-dimensional boron-doped graphyne nanosheet: a new metal-free catalyst for oxygen evolution reaction, Carbon 123 (2017) 558–564.
[89] S. Nandi, S.K. Singh, D. Mullangi, R. Illathvalappil, L. George, C.P. Vinod, S. Kurungot, R. Vaidhyanathan, Low band gap benzimidazole COF supported Ni3N as highly active OER catalyst, Adv. Energy Mater. 6 (2016) 1601189.
[90] V. Tripkovic, H.A. Hansen, T. Vegge, From 3D to 2D Co and Ni oxyhydroxide catalysts: elucidation of the active site and influence of doping on the oxygen evolution activity, ACS Catal. 7 (2017) 8558–8571.
[91] K. Liu, J. Wu, Mechanical properties of two-dimensional materials and heterostructures, J. Mater. Res. 31 (2016) 832–844.
[92] X. Li, P. Cui, W. Zhong, J. Li, X. Wang, Z. Wang, J. Jiang, Graphitic carbon nitride supported single-atom catalysts for efficient oxygen evolution reaction, Chem. Commun. 52 (2016) 13233–13236.
[93] X. Ren, J. Zhou, X. Qi, Y. Liu, Z. Huang, Z. Li, Y. Ge, S.C. Dhanabalan, J.S. Ponraj, S. Wang, J. Zhong, H. Zhang, Few-layer black phosphorus nanosheets as electrocatalysts for highly efficient oxygen evolution reaction, Adv. Energy Mater. 7 (2017) 1700396.
[94] P. Liu, J. Ran, B. Xia, S. Xi, D. Gao, J. Wang, Bifunctional oxygen electrocatalyst of mesoporous Ni/NiO nanosheets for flexible rechargeable Zn–air batteries, Nano-Micro Lett. 12 (2020) 68.
[95] H. Huang, X. Feng, C. Du, S. Wu, W. Song, Incorporated oxygen in MoS2 ultrathin nanosheets for efficient ORR catalysis, J. Mater. Chem. A 3 (2015) 16050–16056.
[96] J. Xie, J. Zhang, S. Li, F. Grote, X. Zhang, H. Zhang, R. Wang, Y. Lei, B. Pan, Y. Xie, Controllable disorder engineering in oxygen-incorporated MoS2 ultrathin nanosheets for efficient hydrogen evolution, J. Am. Chem. Soc. 135 (2013) 17881–17888.
[97] H. Huang, X. Feng, C. Du, W. Song, High-quality phosphorus-doped MoS2 ultrathin nanosheets with amenable ORR catalytic activity, Chem. Commun. 51 (2015) 7903–7906.
[98] L. Li, Z. Wei, S. Chen, X. Qi, W. Ding, M. Xia, R. Li, K. Xiong, Z. Deng, Y. Gao, A comparative DFT study of the catalytic activity of MnO2 (211) and (2-2-1) surfaces for an oxygen reduction reaction, Chem. Phys. Lett. 539–540 (2012) 89–93.
[99] C. Liu, H. Dong, Y. Ji, T. Hou, Y. Li, Origin of the catalytic activity of phosphorus doped MoS2 for oxygen reduction reaction (ORR) in alkaline solution: a theoretical study, Sci. Rep. 8 (2018) 13292.

[100] H. Zhang, Y. Tian, J. Zhao, Q. Cai, Z. Chen, Small dopants make big differences: enhanced electrocatalytic performance of MoS2 monolayer for oxygen reduction reaction (ORR) by N– and P–doping, Electrochim. Acta 225 (2017) 543–550.
[101] F. Chianese, F. Chiarella, M. Barra, A. Candini, M. Affronte, A. Cassinese, Suppression of the morphology mismatch at graphene/n-type organic semiconductor interfaces: a scanning Kelvin probe force microscopy investigation, J. Mater. Chem. C 8 (2020) 8145–8154.
[102] T. Taguchi, F. Chiarella, M. Barra, F. Chianese, Y. Kubozono, A. Cassinese, Balanced ambipolar charge transport in phenacene/perylene heterojunction-based organic field-effect transistors, ACS Appl. Mater. Interfaces 13 (2021) 8631–8642.
[103] V. Preziosi, M. Barra, G. Tomaiuolo, P. D'Angelo, S.L. Marasso, A. Verna, M. Cocuzza, A. Cassinese, S. Guido, Organic electrochemical transistors as novel biosensing platforms to study the electrical response of whole blood and plasma, J. Mater. Chem. B 10 (2022) 87–95.
[104] B.B. Xiao, P. Zhang, L.P. Han, Z. Wen, Functional MoS2 by the Co/Ni doping as the catalyst for oxygen reduction reaction, Appl. Surf. Sci. 354 (2015) 221–228.
[105] V. Urbanová, P. Lazar, N. Antonatos, Z. Sofer, M. Otyepka, M. Pumera, Positive and negative effects of dopants toward electrocatalytic activity of MoS2 and WS2: experiments and theory, ACS Appl. Mater. Interfaces 12 (2020) 20383–20392.
[106] J. Di, J. Xia, M.F. Chisholm, J. Zhong, C. Chen, X. Cao, F. Dong, Z. Chi, H. Chen, Y.-X. Weng, J. Xiong, S.-Z. Yang, H. Li, Z. Liu, S. Dai, Defect-tailoring mediated electron–hole separation in single-unit-cell Bi3O4Br nanosheets for boosting photocatalytic hydrogen evolution and nitrogen fixation, Adv. Mater. 31 (2019) 1807576.
[107] Z. Wang, J. Zhao, Q. Cai, F. Li, Computational screening for high-activity MoS2 monolayer-based catalysts for the oxygen reduction reaction via substitutional doping with transition metal, J. Mater. Chem. A 5 (2017) 9842–9851.
[108] Y. Yang, H. Fei, G. Ruan, Y. Li, J.M. Tour, Vertically aligned WS2 nanosheets for water splitting, Adv. Funct. Mater. 25 (2015) 6199–6204.
[109] J. Yang, A.R. Mohmad, Y. Wang, R. Fullon, X. Song, F. Zhao, I. Bozkurt, M. Augustin, E.J.G. Santos, H.S. Shin, W. Zhang, D. Voiry, H.Y. Jeong, M. Chhowalla, Ultrahigh-current-density niobium disulfide catalysts for hydrogen evolution, Nat. Mater. 18 (2019) 1309–1314.
[110] J. Si, Q. Zheng, H. Chen, C. Lei, Y. Suo, B. Yang, Z. Zhang, Z. Li, L. Lei, Y. Hou, K. Ostrikov, Scalable production of few-layer niobium disulfide nanosheets via electrochemical exfoliation for energy-efficient hydrogen evolution reaction, ACS Appl. Mater. Interfaces 11 (2019) 13205–13213.
[111] N.K. Oh, C. Kim, J. Lee, O. Kwon, Y. Choi, G.Y. Jung, H.Y. Lim, S.K. Kwak, G. Kim, H. Park, In-situ local phase-transitioned MoSe2 in La0.5Sr0.5CoO3-δ heterostructure and stable overall water electrolysis over 1000 hours, Nat. Commun. 10 (2019) 1723.
[112] R. Wang, X. Li, T. Gao, T. Yao, S. Liu, X. Wang, J. Han, P. Zhang, X. Cao, X. Zhang, Y. Zhang, B. Song, Beyond 1T-phase? Synergistic electronic structure and defects engineering in 2H-MoS2xSe2(1-x) nanosheets for enhanced hydrogen evolution reaction and sodium storage, ChemCatChem 11 (2019) 3200–3211.
[113] J. Lin, P. Wang, H. Wang, C. Li, X. Si, J. Qi, J. Cao, Z. Zhong, W. Fei, J. Feng, Defect-rich heterogeneous MoS2/NiS2 nanosheets electrocatalysts for efficient overall water splitting, Adv. Sci. 6 (2019) 1900246.
[114] Q. Xiong, Y. Wang, P.-F. Liu, L.-R. Zheng, G. Wang, H.-G. Yang, P.-K. Wong, H. Zhang, H. Zhao, Cobalt covalent doping in MoS2 to induce bifunctionality of overall water splitting, Adv. Mater. 30 (2018) 1801450.
[115] Y. Gu, A. Wu, Y. Jiao, H. Zheng, X. Wang, Y. Xie, L. Wang, C. Tian, H. Fu, Two-dimensional porous molybdenum phosphide/nitride heterojunction nanosheets for pH-universal hydrogen evolution reaction, Angew. Chem. Int. Ed. 60 (2021) 6673–6681.
[116] D. Guo, X. Li, Y. Jiao, H. Yan, A. Wu, G. Yang, Y. Wang, C. Tian, H. Fu, A dual-active Co-CoO heterojunction coupled with Ti3C2-MXene for highly-performance overall water splitting, Nano Res. 15 (2022) 238–247.
[117] Y. Li, K. Yin, L. Wang, X. Lu, Y. Zhang, Y. Liu, D. Yan, Y. Song, S. Luo, Engineering MoS2 nanomesh with holes and lattice defects for highly active hydrogen evolution reaction, Appl. Catal. B Environ. 239 (2018) 537–544.
[118] H. Li, Y. Tan, P. Liu, C. Guo, M. Luo, J. Han, T. Lin, F. Huang, M. Chen, Atomic-sized pores enhanced electrocatalysis of TaS2 nanosheets for hydrogen evolution, Adv. Mater. 28 (2016) 8945–8949.
[119] X. Wang, Y. Chen, B. Zheng, F. Qi, J. He, Q. Li, P. Li, W. Zhang, Graphene-like WSe2 nanosheets for efficient and stable hydrogen evolution, J. Alloys Compd. 691 (2017) 698–704.
[120] C. Tang, H. Zhang, K. Xu, Q. Zhang, J. Liu, C. He, L. Fan, T. Asefa, Unconventional molybdenum carbide phases with high electrocatalytic activity for hydrogen evolution reaction, J. Mater. Chem. A 7 (2019) 18030–18038.
[121] H. Yan, Y. Xie, Y. Jiao, A. Wu, C. Tian, X. Zhang, L. Wang, H. Fu, Holey reduced graphene oxide coupled with an Mo2N–Mo2C heterojunction for efficient hydrogen evolution, Adv. Mater. 30 (2018) 1704156.
[122] J. Xiong, W. Cai, W. Shi, X. Zhang, J. Li, Z. Yang, L. Feng, H. Cheng, Salt-templated synthesis of defect-rich Mon nanosheets for boosted hydrogen evolution reaction, J. Mater. Chem. A 5 (2017) 24193–24198.
[123] J. Wu, T. Chen, C. Zhu, J. Du, L. Huang, J. Yan, D. Cai, C. Guan, C. Pan, Rational construction of a WS2/CoS2 heterostructure electrocatalyst for efficient hydrogen evolution at all pH values, ACS Sustain. Chem. Eng. 8 (2020) 4474–4480.
[124] H. Chen, M. Hu, P. Jing, B. Liu, R. Gao, J. Zhang, Constructing heterostructure of CeO2/WS2 to enhance catalytic activity and stability toward hydrogen generation, J. Power Sources 521 (2022) 230948.
[125] L. Sun, H. Xu, Z. Cheng, D. Zheng, Q. Zhou, S. Yang, J. Lin, A heterostructured WS2/WSe2 catalyst by heterojunction engineering towards boosting hydrogen evolution reaction, Chem. Eng. J. 443 (2022) 136348.
[126] C. Cui, R. Cheng, H. Zhang, C. Zhang, Y. Ma, C. Shi, B. Fan, H. Wang, X. Wang, Ultrastable MXene@Pt/SWCNTs' nanocatalysts for hydrogen evolution reaction, Adv. Funct. Mater. 30 (2020) 2000693.
[127] J. Jia, T. Xiong, L. Zhao, F. Wang, H. Liu, R. Hu, J. Zhou, W. Zhou, S. Chen, Ultrathin N-doped Mo2C nanosheets with exposed active sites as efficient electrocatalyst for hydrogen evolution reactions, ACS Nano 11 (2017) 12509–12518.
[128] Y. Yin, Y. Zhang, T. Gao, T. Yao, X. Zhang, J. Han, X. Wang, Z. Zhang, P. Xu, P. Zhang, X. Cao, B. Song, S. Jin, Synergistic phase and disorder engineering in 1T-MoSe2 nanosheets for enhanced hydrogen-evolution reaction, Adv. Mater. 29 (2017) 1700311.
[129] C. Li, H. Jang, M.G. Kim, L. Hou, X. Liu, J. Cho, Ru-incorporated oxygen-vacancy-enriched MoO2 electrocatalysts for hydrogen evolution reaction, Appl. Catal. B Environ. 307 (2022) 121204.
[130] C. Zhang, Y. Shi, Y. Yu, Y. Du, B. Zhang, Engineering sulfur defects, atomic thickness, and porous structures into cobalt sulfide nanosheets for efficient electrocatalytic alkaline hydrogen evolution, ACS Catal. 8 (2018) 8077–8083.
[131] H. Jin, X. Liu, A. Vasileff, Y. Jiao, Y. Zhao, Y. Zheng, S.-Z. Qiao, Single-crystal nitrogen-rich two-dimensional Mo5N6 nanosheets for efficient and stable seawater splitting, ACS Nano 12 (2018) 12761–12769.
[132] J. Cai, J. Yang, X. Xie, J. Ding, L. Liu, W. Tian, Y. Liu, Z. Tang, B. Liu, S. Lu, Carbon doping triggered efficient electrochemical hydrogen evolution of cross-linked porous Ru-MoO2 via solid-phase reaction strategy, Energy Environ. Mater. 6 (2023) e12424.
[133] Z. Fang, L. Peng, Y. Qian, X. Zhang, Y. Xie, J.J. Cha, G. Yu, Dual tuning of Ni–Co–A (A = P, Se, O) nanosheets by anion substitution and holey engineering for efficient hydrogen evolution, J. Am. Chem. Soc. 140 (2018) 5241–5247.
[134] Y. Jing, X. Mu, C. Xie, H. Liu, R. Yan, H. Dai, C. Liu, X.-D. Zhang, Enhanced hydrogen evolution reaction of WS2–CoS2 heterostructure by synergistic effect, Int. J. Hydrogen Energy 44 (2019) 809–818.
[135] W. Wang, Y. Song, C. Ke, Y. Li, Y. Liu, C. Ma, Z. Wu, J. Qi, K. Bao, L. Wang, J. Wu, S. Jiang, J. Zhao, C.-S. Lee, Y. Chen, G. Luo, Q. He, R. Ye, Filling the gap between heteroatom doping and edge enrichment of 2D electrocatalysts for enhanced hydrogen evolution, ACS Nano 17 (2023) 1287–1297.
[136] D. Gao, B. Xia, Y. Wang, W. Xiao, P. Xi, D. Xue, J. Ding, Dual-native vacancy activated basal plane and conductivity of MoSe2 with high-efficiency hydrogen evolution reaction, Small 14 (2018) 1704150.
[137] L. Lin, N. Miao, Y. Wen, S. Zhang, P. Ghosez, Z. Sun, D.A. Allwood, Sulfur-depleted monolayered molybdenum disulfide nanocrystals for superelectrochemical hydrogen evolution reaction, ACS Nano 10 (2016) 8929–8937.
[138] J. Shi, D. Ma, G.-F. Han, Y. Zhang, Q. Ji, T. Gao, J. Sun, X. Song, C. Li, Y. Zhang, X.-Y. Lang, Y. Zhang, Z. Liu, Controllable growth and transfer of monolayer MoS2 on Au foils and its potential application in hydrogen evolution reaction, ACS Nano 8 (2014) 10196–10204.
[139] D. Voiry, H. Yamaguchi, J. Li, R. Silva, D.C.B. Alves, T. Fujita, M. Chen, T. Asefa, V.B. Shenoy, G. Eda, M. Chhowalla, Enhanced catalytic activity in strained chemically exfoliated WS2 nanosheets for hydrogen evolution, Nat. Mater. 12 (2013) 850–855.
[140] G. Ye, Y. Gong, J. Lin, B. Li, Y. He, S.T. Pantelides, W. Zhou, R. Vajtai, P. M. Ajayan, Defects engineered monolayer MoS2 for improved hydrogen evolution reaction, Nano Lett. 16 (2016) 1097–1103.
[141] J. Xie, H. Zhang, S. Li, R. Wang, X. Sun, M. Zhou, J. Zhou, X.W. Lou, Y. Xie, Defect-rich MoS2 ultrathin nanosheets with additional active edge sites for enhanced electrocatalytic hydrogen evolution, Adv. Mater. (Deerfield Beach, Fla.) 25 (2013) 5807–5813.
[142] J.N. Coleman, M. Lotya, A. O'Neill, S.D. Bergin, P.J. King, U. Khan, K. Young, A. Gaucher, S. De, R.J. Smith, I.V. Shvets, S.K. Arora, G. Stanton, H.-Y. Kim, K. Lee, G.T. Kim, G.S. Duesberg, T. Hallam, J.J. Boland, J.J. Wang, J.F. Donegan, J.C. Grunlan, G. Moriarty, A. Shmeliov, R.J. Nicholls, J.M. Perkins, E. M. Grieveson, K. Theuwissen, D.W. McComb, P.D. Nellist, V. Nicolosi, Two-dimensional nanosheets produced by liquid exfoliation of layered materials, Science 331 (2011) 568–571.
[143] Z. Lei, S. Xu, P. Wu, Ultra-thin and porous MoSe2 nanosheets: facile preparation and enhanced electrocatalytic activity towards the hydrogen evolution reaction, Phys. Chem. Chem. Phys. 18 (2016) 70–74.
[144] C. Tan, Z. Luo, A. Chaturvedi, Y. Cai, Y. Du, Y. Gong, Y. Huang, Z. Lai, X. Zhang, L. Zheng, X. Qi, M.H. Goh, J. Wang, S. Han, X.-J. Wu, L. Gu, C. Kloc, H. Zhang, Preparation of high-percentage 1T-phase transition metal dichalcogenide nanodots for electrochemical hydrogen evolution, Adv. Mater. 30 (2018) 1705509.
[145] L. Lin, N. Miao, J. Huang, S. Zhang, Y. Zhu, D.D. Horsell, P. Ghosez, Z. Sun, D. A. Allwood, A photocatalyst of sulphur depleted monolayered molybdenum sulfide nanocrystals for dye degradation and hydrogen evolution reaction, Nano Energy 38 (2017) 544–552.
[146] J. Deng, H. Li, J. Xiao, Y. Tu, D. Deng, H. Yang, H. Tian, J. Li, P. Ren, X. Bao, Triggering the electrocatalytic hydrogen evolution activity of the inert two-dimensional MoS2 surface via single-atom metal doping, Energy Environ. Sci. 8 (2015) 1594–1601.
[147] X. Huang, M. Leng, W. Xiao, M. Li, J. Ding, T.L. Tan, W.S.V. Lee, J. Xue, Activating basal planes and S-terminated edges of MoS2 toward more efficient hydrogen evolution, Adv. Funct. Mater. 27 (2017) 1604943.
[148] J. Xie, H. Qu, J. Xin, X. Zhang, G. Cui, X. Zhang, J. Bao, B. Tang, Y. Xie, Defect-rich MoS2 nanowall catalyst for efficient hydrogen evolution reaction, Nano Res. 10 (2017) 1178–1188.

[149] K. Sun, T. Cheng, L. Wu, Y. Hu, J. Zhou, A. Maclennan, Z. Jiang, Y. Gao, W. A. Goddard III, Z. Wang, Ultrahigh mass activity for carbon dioxide reduction enabled by gold–iron core–shell nanoparticles, J. Am. Chem. Soc. 139 (2017) 15608–15611.
[150] R. Ye, P. del Angel-Vicente, Y. Liu, M.J. Arellano-Jimenez, Z. Peng, T. Wang, Y. Li, B.I. Yakobson, S.-H. Wei, M.J. Yacaman, J.M. Tour, High-performance hydrogen evolution from MoS2(1–x)P x solid solution, Adv. Mater. 28 (2016) 1427–1432.
[151] D. Merki, H. Vrubel, L. Rovelli, S. Fierro, X. Hu, Fe, Co, and Ni ions promote the catalytic activity of amorphous molybdenum sulfide films for hydrogen evolution, Chem. Sci. 3 (2012) 2515–2525.
[152] T.A. Shifa, F. Wang, K. Liu, Z. Cheng, K. Xu, Z. Wang, X. Zhan, C. Jiang, J. He, Efficient catalysis of hydrogen evolution reaction from WS2(1−x)P2x nanoribbons, Small 13 (2017) 1603706.
[153] W. Zhou, J. Jia, J. Lu, L. Yang, D. Hou, G. Li, S. Chen, Recent developments of carbon-based electrocatalysts for hydrogen evolution reaction, Nano Energy 28 (2016) 29–43.
[154] B. Zhang, H.-H. Wang, H. Su, L.-B. Lv, T.-J. Zhao, J.-M. Ge, X. Wei, K.-X. Wang, X.-H. Li, J.-S. Chen, Nitrogen-doped graphene microtubes with opened inner voids: highly efficient metal-free electrocatalysts for alkaline hydrogen evolution reaction, Nano Res. 9 (2016) 2606–2615.
[155] Y. Tian, Y. Ye, X. Wang, S. Peng, Z. Wei, X. Zhang, W. Liu, Three-dimensional N-doped, plasma-etched graphene: highly active metal-free catalyst for hydrogen evolution reaction, Appl. Catal. Gen. 529 (2017) 127–133.
[156] Y. Jiao, Y. Zheng, K. Davey, S.-Z. Qiao, Activity origin and catalyst design principles for electrocatalytic hydrogen evolution on heteroatom-doped graphene, Nat. Energy 1 (2016) 16130.
[157] Y. Ito, W. Cong, T. Fujita, Z. Tang, M. Chen, High catalytic activity of nitrogen and sulfur Co-doped nanoporous graphene in the hydrogen evolution reaction, Angew. Chem. Int. Ed. 54 (2015) 2131–2136.
[158] X. Yue, S. Huang, Y. Jin, P.K. Shen, Nitrogen and fluorine dual-doped porous graphene-nanosheets as efficient metal-free electrocatalysts for hydrogen-evolution in acidic media, Catal. Sci. Technol. 7 (2017) 2228–2235.
[159] Y. Ouyang, C. Ling, Q. Chen, Z. Wang, L. Shi, J. Wang, Activating inert basal planes of MoS2 for hydrogen evolution reaction through the formation of different intrinsic defects, Chem. Mater. 28 (2016) 4390–4396.
[160] J. Hong, Z. Hu, M. Probert, K. Li, D. Lv, X. Yang, L. Gu, N. Mao, Q. Feng, L. Xie, J. Zhang, D. Wu, Z. Zhang, C. Jin, W. Ji, X. Zhang, J. Yuan, Z. Zhang, Exploring atomic defects in molybdenum disulphide monolayers, Nat. Commun. 6 (2015) 6293.
[161] S. Najmaei, Z. Liu, W. Zhou, X. Zou, G. Shi, S. Lei, B.I. Yakobson, J.-C. Idrobo, P. M. Ajayan, J. Lou, Vapour phase growth and grain boundary structure of molybdenum disulphide atomic layers, Nat. Mater. 12 (2013) 754–759.
[162] Q. Ma, P.M. Odenthal, J. Mann, D. Le, C.S. Wang, Y. Zhu, T. Chen, D. Sun, K. Yamaguchi, T. Tran, M. Wurch, J.L. McKinley, J. Wyrick, K. Magnone, T. F. Heinz, T.S. Rahman, R. Kawakami, L. Bartels, Controlled argon beam-induced desulfurization of monolayer molybdenum disulfide, J. Phys. Condens. Matter 25 (2013) 252201.
[163] T. Hu, M. Hu, Z. Li, H. Zhang, C. Zhang, J. Wang, X. Wang, Interlayer coupling in two-dimensional titanium carbide MXenes, Phys. Chem. Chem. Phys. 18 (2016) 20256–20260.
[164] D. Voiry, M. Salehi, R. Silva, T. Fujita, M. Chen, T. Asefa, V.B. Shenoy, G. Eda, M. Chhowalla, Conducting MoS2 nanosheets as catalysts for hydrogen evolution reaction, Nano Lett. 13 (2013) 6222–6227.
[165] B. Yildiz, "Stretching" the energy landscape of oxides—effects on electrocatalysis and diffusion, MRS Bull. 39 (2014) 147–156.
[166] W. Zhou, X. Zou, S. Najmaei, Z. Liu, Y. Shi, J. Kong, J. Lou, P.M. Ajayan, B. I. Yakobson, J.-C. Idrobo, Intrinsic structural defects in monolayer molybdenum disulfide, Nano Lett. 13 (2013) 2615–2622.
[167] H. Wang, Z. Lu, S. Xu, D. Kong, J.J. Cha, G. Zheng, P.-C. Hsu, K. Yan, D. Bradshaw, F.B. Prinz, Y. Cui, Electrochemical tuning of vertically aligned mos2 nanofilms and its application in improving hydrogen evolution reaction, Proc. National Acad. Sci. 110 (2013) 19701–19706.
[168] K. Chang, X. Hai, H. Pang, H. Zhang, L. Shi, G. Liu, H. Liu, G. Zhao, M. Li, J. Ye, Targeted synthesis of 2H- and 1T-phase MoS2 monolayers for catalytic hydrogen evolution, Adv. Mater. 28 (2016) 10033–10041.
[169] C. Tsai, K. Chan, F. Abild-Pedersen, J.K. Nørskov, Active edge sites in MoSe2 and WSe2 catalysts for the hydrogen evolution reaction: a density functional study, Phys. Chem. Chem. Phys. 16 (2014) 13156–13164.
[170] C. Tsai, F. Abild-Pedersen, J.K. Nørskov, Tuning the MoS2 edge-site activity for hydrogen evolution via support interactions, Nano Lett. 14 (2014) 1381–1387.
[171] Y. Zhang, J. Shi, G. Han, M. Li, Q. Ji, D. Ma, Y. Zhang, C. Li, X. Lang, Y. Zhang, Z. Liu, Chemical vapor deposition of monolayer WS2 nanosheets on Au foils toward direct application in hydrogen evolution, Nano Res. 8 (2015) 2881–2890.
[172] M. Acerce, D. Voiry, M. Chhowalla, Metallic 1T phase MoS2 nanosheets as supercapacitor electrode materials, Nat. Nanotechnol. 10 (2015) 313–318.
[173] B. Hinnemann, P.G. Moses, J. Bonde, K.P. Jørgensen, J.H. Nielsen, S. Horch, I. Chorkendorff, J.K. Nørskov, Biomimetic hydrogen evolution: MoS2 nanoparticles as catalyst for hydrogen evolution, J. Am. Chem. Soc. 127 (2005) 5308–5309.
[174] A. Jawaid, J. Che, L.F. Drummy, J. Bultman, A. Waite, M.-S. Hsiao, R.A. Vaia, Redox exfoliation of layered transition metal dichalcogenides, ACS Nano 11 (2017) 635–646.
[175] Q. He, L. Wang, K. Yin, S. Luo, Vertically aligned ultrathin 1T-WS2 nanosheets enhanced the electrocatalytic hydrogen evolution, Nanoscale Res. Lett. 13 (2018) 167.
[176] M.S. Sokolikova, P.C. Sherrell, P. Palczynski, V.L. Bemmer, C. Mattevi, Direct solution-phase synthesis of 1T' WSe2 nanosheets, Nat. Commun. 10 (2019) 712.
[177] Y. Zheng, Y. Jiao, Y. Zhu, L.H. Li, Y. Han, Y. Chen, A. Du, M. Jaroniec, S.Z. Qiao, Hydrogen evolution by a metal-free electrocatalyst, Nat. Commun. 5 (2014) 3783.
[178] K.S. Novoselov, A. Mishchenko, A. Carvalho, A.H. Castro Neto, 2D materials and van der Waals heterostructures, Science 353 (2016) aac9439.
[179] M. Gong, W. Zhou, M.-C. Tsai, J. Zhou, M. Guan, M.-C. Lin, B. Zhang, Y. Hu, D.-Y. Wang, J. Yang, S.J. Pennycook, B.-J. Hwang, H. Dai, Nanoscale nickel oxide/nickel heterostructures for active hydrogen evolution electrocatalysis, Nat. Commun. 5 (2014) 4695.
[180] J. Duan, S. Chen, M. Jaroniec, S.Z. Qiao, Porous C3N4 nanolayers@N-graphene films as catalyst electrodes for highly efficient hydrogen evolution, ACS Nano 9 (2015) 931–940.
[181] J. Duan, S. Chen, B.A. Chambers, G.G. Andersson, S.Z. Qiao, 3D WS2 Nanolayers@Heteroatom-doped graphene films as hydrogen evolution catalyst electrodes, Adv. Mater. 27 (2015) 4234–4241.
[182] M.-R. Gao, J.-X. Liang, Y.-R. Zheng, Y.-F. Xu, J. Jiang, Q. Gao, J. Li, S.-H. Yu, An efficient molybdenum disulfide/cobalt diselenide hybrid catalyst for electrochemical hydrogen generation, Nat. Commun. 6 (2015) 5982.
[183] J. Staszak-Jirkovský, Christos D. Malliakas, Pietro P. Lopes, N. Danilovic, Subrahmanyam S. Kota, K.-C. Chang, B. Genorio, D. Strmcnik, Vojislav R. Stamenkovic, M.G. Kanatzidis, N.M. Markovic, Design of active and stable Co–Mo–Sx chalcogels as pH-universal catalysts for the hydrogen evolution reaction, Nat. Mater. 15 (2016) 197–203.
[184] J. Yang, D. Voiry, S.J. Ahn, D. Kang, A.Y. Kim, M. Chhowalla, H.S. Shin, Two-dimensional hybrid nanosheets of tungsten disulfide and reduced graphene oxide as catalysts for enhanced hydrogen evolution, Angew. Chem. Int. Ed. 52 (2013) 13751–13754.
[185] X. Huang, Z. Zeng, S. Bao, M. Wang, X. Qi, Z. Fan, H. Zhang, Solution-phase epitaxial growth of noble metal nanostructures on dispersible single-layer molybdenum disulfide nanosheets, Nat. Commun. 4 (2013) 1444.
[186] Y. Li, H. Wang, L. Xie, Y. Liang, G. Hong, H. Dai, MoS2 nanoparticles grown on graphene: an advanced catalyst for the hydrogen evolution reaction, J. Am. Chem. Soc. 133 (2011) 7296–7299.
[187] X. Du, J. Huang, J. Zhang, Y. Yan, C. Wu, Y. Hu, C. Yan, T. Lei, W. Chen, C. Fan, J. Xiong, Modulating electronic structures of inorganic nanomaterials for efficient electrocatalytic water splitting, Angew. Chem. Int. Ed. 58 (2019) 4484–4502.
[188] Y. Shi, Y. Zhou, D.-R. Yang, W.-X. Xu, C. Wang, F.-B. Wang, J.-J. Xu, X.-H. Xia, H.-Y. Chen, Energy level engineering of MoS2 by transition-metal doping for accelerating hydrogen evolution reaction, J. Am. Chem. Soc. 139 (2017) 15479–15485.
[189] T.A. Shifa, F. Wang, K. Liu, K. Xu, Z. Wang, X. Zhan, C. Jiang, J. He, Engineering the electronic structure of 2D WS2 nanosheets using Co incorporation as CoxW(1-x)S2 for conspicuously enhanced hydrogen generation, Small 12 (2016) 3802–3809.
[190] Y. Gong, Z. Liu, A.R. Lupini, G. Shi, J. Lin, S. Najmaei, Z. Lin, A.L. Elías, A. Berkdemir, G. You, H. Terrones, M. Terrones, R. Vajtai, S.T. Pantelides, S. J. Pennycook, J. Lou, W. Zhou, P.M. Ajayan, Band gap engineering and layer-by-layer mapping of selenium-doped molybdenum disulfide, Nano Lett. 14 (2014) 442–449.
[191] Q. Fu, L. Yang, W. Wang, A. Han, J. Huang, P. Du, Z. Fan, J. Zhang, B. Xiang, Synthesis and enhanced electrochemical catalytic performance of monolayer WS2 (1–x)Se2x with a tunable band gap, Adv. Mater. 27 (2015) 4732–4738.
[192] K. Zhang, H.-J. Kim, J.-T. Lee, G.-W. Chang, X. Shi, W. Kim, M. Ma, K.-j. Kong, J.-M. Choi, M.-S. Song, J.H. Park, Unconventional pore and defect generation in molybdenum disulfide: application in high-rate lithium-ion batteries and the hydrogen evolution reaction, ChemSusChem 7 (2014) 2489–2495.
[193] X. Sun, J. Dai, Y. Guo, C. Wu, F. Hu, J. Zhao, X. Zeng, Y. Xie, Semimetallic molybdenum disulfide ultrathin nanosheets as an efficient electrocatalyst for hydrogen evolution, Nanoscale 6 (2014) 8359–8367.
[194] J. Bonde, P.G. Moses, T.F. Jaramillo, J.K. Nørskov, I. Chorkendorff, Hydrogen evolution on nano-particulate transition metal sulfides, Faraday Discuss 140 (2009) 219–231.
[195] Q. Xiong, X. Zhang, H. Wang, G. Liu, G. Wang, H. Zhang, H. Zhao, One-step synthesis of cobalt-doped MoS2 nanosheets as bifunctional electrocatalysts for overall water splitting under both acidic and alkaline conditions, Chem. Commun. 54 (2018) 3859–3862.
[196] G. Liu, Z. Cui, M. Han, S. Zhang, C. Zhao, C. Chen, G. Wang, H. Zhang, Ambient electrosynthesis of ammonia on a core–shell-structured Au@CeO2 catalyst: contribution of oxygen vacancies in CeO2, Chem. Eur J. 25 (2019) 5904–5911.
[197] L. Yang, Q. Fu, W. Wang, J. Huang, J. Huang, J. Zhang, B. Xiang, Large-area synthesis of monolayered MoS2(1−x)Se2x with a tunable band gap and its enhanced electrochemical catalytic activity, Nanoscale 7 (2015) 10490–10497.
[198] Q. Ding, J. Zhai, M. Cabán-Acevedo, M.J. Shearer, L. Li, H.-C. Chang, M.-L. Tsai, D. Ma, X. Zhang, R.J. Hamers, J.-H. He, S. Jin, Designing efficient solar-driven hydrogen evolution photocathodes using semitransparent MoQxCly (Q = S, Se) catalysts on Si micropyramids, Adv. Mater. 27 (2015) 6511–6518.
[199] X. Zhang, F. Meng, S. Mao, Q. Ding, M.J. Shearer, M.S. Faber, J. Chen, R. J. Hamers, S. Jin, Amorphous MoSxCly electrocatalyst supported by vertical graphene for efficient electrochemical and photoelectrochemical hydrogen generation, Energy Environ. Sci. 8 (2015) 862–868.
[200] Y. Sun, F. Alimohammadi, D. Zhang, G. Guo, Enabling colloidal synthesis of edge-oriented MoS2 with expanded interlayer spacing for enhanced HER catalysis, Nano Lett. 17 (2017) 1963–1969.

[201] P. Xiong, R. Ma, N. Sakai, L. Nurdiwijayanto, T. Sasaki, Unilamellar metallic MoS2/graphene superlattice for efficient sodium storage and hydrogen evolution, ACS Energy Lett. 3 (2018) 997–1005.
[202] H. Tang, K. Dou, C.-C. Kaun, Q. Kuang, S. Yang, MoSe2 nanosheets and their graphene hybrids: synthesis, characterization and hydrogen evolution reaction studies, J. Mater. Chem. A 2 (2014) 360–364.
[203] T.-N. Ye, L.-B. Lv, M. Xu, B. Zhang, K.-X. Wang, J. Su, X.-H. Li, J.-S. Chen, Hierarchical carbon nanopapers coupled with ultrathin MoS2 nanosheets: highly efficient large-area electrodes for hydrogen evolution, Nano Energy 15 (2015) 335–342.
[204] Z. Zhao, F. Qin, S. Kasiraju, L. Xie, M.K. Alam, S. Chen, D. Wang, Z. Ren, Z. Wang, L.C. Grabow, J. Bao, Vertically aligned MoS2/Mo2C hybrid nanosheets grown on carbon paper for efficient electrocatalytic hydrogen evolution, ACS Catal. 7 (2017) 7312–7318.
[205] J. Zhang, Y. Chen, M. Liu, K. Du, Y. Zhou, Y. Li, Z. Wang, J. Zhang, 1T@2H-MoSe2 nanosheets directly arrayed on Ti plate: an efficient electrocatalytic electrode for hydrogen evolution reaction, Nano Res. 11 (2018) 4587–4598.
[206] S. Yeo, D.K. Nandi, R. Rahul, T.H. Kim, B. Shong, Y. Jang, J.-S. Bae, J.W. Han, S.-H. Kim, H. Kim, Low-temperature direct synthesis of high quality WS2 thin films by plasma-enhanced atomic layer deposition for energy related applications, Appl. Surf. Sci. 459 (2018) 596–605.
[207] J. Cao, J. Zhou, Y. Zhang, Y. Wang, X. Liu, Dominating role of aligned MoS2/Ni3S2 nanoarrays supported on three-dimensional Ni foam with hydrophilic interface for highly enhanced hydrogen evolution reaction, ACS Appl. Mater. Interfaces 10 (2018) 1752–1760.
[208] H. Zhou, F. Yu, Y. Huang, J. Sun, Z. Zhu, R.J. Nielsen, R. He, J. Bao, W.A. Goddard Iii, S. Chen, Z. Ren, Efficient hydrogen evolution by ternary molybdenum sulfoselenide particles on self-standing porous nickel diselenide foam, Nat. Commun. 7 (2016) 12765.
[209] Y.-H. Chang, C.-T. Lin, T.-Y. Chen, C.-L. Hsu, Y.-H. Lee, W. Zhang, K.-H. Wei, L.-J. Li, Highly efficient electrocatalytic hydrogen production by MoSx grown on graphene-protected 3D Ni foams, Adv. Mater. 25 (2013) 756–760.
[210] Y. Yang, H. Yao, Z. Yu, S.M. Islam, H. He, M. Yuan, Y. Yue, K. Xu, W. Hao, G. Sun, H. Li, S. Ma, P. Zapol, M.G. Kanatzidis, Hierarchical nanoassembly of MoS2/Co9S8/Ni3S2/Ni as a highly efficient electrocatalyst for overall water splitting in a wide pH range, J. Am. Chem. Soc. 141 (2019) 10417–10430.
[211] Q. Ding, B. Song, P. Xu, S. Jin, Efficient electrocatalytic and photoelectrochemical hydrogen generation using MoS2 and related compounds, Chem 1 (2016) 699–726.
[212] G. Zhao, K. Rui, S.X. Dou, W. Sun, Heterostructures for electrochemical hydrogen evolution reaction: a review, Adv. Funct. Mater. 28 (2018) 1803291.
[213] P. Quaino, F. Juarez, E. Santos, W. Schmickler, Volcano plots in hydrogen electrocatalysis - uses and abuses, Beilstein J. Nanotechnol. 5 (2014) 846–854.
[214] R. Parsons, The rate of electrolytic hydrogen evolution and the heat of adsorption of hydrogen, Trans. Faraday Soc. 54 (1958) 1053–1063.
[215] E. Skúlason, V. Tripkovic, M.E. Björketun, S. Gudmundsdóttir, G. Karlberg, J. Rossmeisl, T. Bligaard, H. Jónsson, J.K. Nørskov, Modeling the electrochemical hydrogen oxidation and evolution reactions on the basis of density functional theory calculations, J. Phys. Chem. C 114 (2010) 18182–18197.
[216] S.-H. Lin, J.-L. Kuo, Activating and tuning basal planes of MoO2, MoS2, and MoSe2 for hydrogen evolution reaction, Phys. Chem. Chem. Phys. 17 (2015) 29305–29310.
[217] J. Wei, M. Zhou, A. Long, Y. Xue, H. Liao, C. Wei, Z.J. Xu, Heterostructured electrocatalysts for hydrogen evolution reaction under alkaline conditions, Nano-Micro Lett. 10 (2018) 75.
[218] L.-N. Zhang, Z.-L. Lang, Y.-H. Wang, H.-Q. Tan, H.-Y. Zang, Z.-H. Kang, Y.-G. Li, Cable-like Ru/WNO@C nanowires for simultaneous high-efficiency hydrogen evolution and low-energy consumption chlor-alkali electrolysis, Energy Environ. Sci. 12 (2019) 2569–2580.
[219] N. Danilovic, R. Subbaraman, D. Strmcnik, K.-C. Chang, A.P. Paulikas, V. R. Stamenkovic, N.M. Markovic, Enhancing the alkaline hydrogen evolution reaction activity through the bifunctionality of Ni(OH)2/Metal catalysts, Angew. Chem. Int. Ed. 51 (2012) 12495–12498.
[220] Y. Wang, Z. Chen, P. Han, Y. Du, Z. Gu, X. Xu, G. Zheng, Single-atomic Cu with multiple oxygen vacancies on ceria for electrocatalytic CO2 reduction to CH4, ACS Catal. 8 (2018) 7113–7119.
[221] F. Cai, X. Hu, F. Gou, Y. Chen, Y. Xu, C. Qi, D.-K. Ma, Ultrathin ZnIn2S4 nanosheet arrays activated by nitrogen-doped carbon for electrocatalytic CO2 reduction reaction toward ethanol, Appl. Surf. Sci. 611 (2023) 155696.
[222] S. Guo, S. Zhao, X. Wu, H. Li, Y. Zhou, C. Zhu, N. Yang, X. Jiang, J. Gao, L. Bai, Y. Liu, Y. Lifshitz, S.-T. Lee, Z. Kang, A Co3O4-CDots-C3N4 three component electrocatalyst design concept for efficient and tunable CO2 reduction to syngas, Nat. Commun. 8 (2017) 1828.
[223] X. Lu, T.H. Tan, Y.H. Ng, R. Amal, Highly selective and stable reduction of CO2 to CO by a graphitic carbon nitride/carbon nanotube composite electrocatalyst, Chem. Eur J. 22 (2016) 11991–11996.
[224] P. Abbasi, M. Asadi, C. Liu, S. Sharifi-Asl, B. Sayahpour, A. Behranginia, P. Zapol, R. Shahbazian-Yassar, L.A. Curtiss, A. Salehi-Khojin, Tailoring the edge structure of molybdenum disulfide toward electrocatalytic reduction of carbon dioxide, ACS Nano 11 (2017) 453–460.
[225] M. Asadi, K. Kim, C. Liu, A.V. Addepalli, P. Abbasi, P. Yasaei, P. Phillips, A. Behranginia, J.M. Cerrato, R. Haasch, P. Zapol, B. Kumar, R.F. Klie, J. Abiade, L.A. Curtiss, A. Salehi-Khojin, Nanostructured transition metal dichalcogenide electrocatalysts for CO2 reduction in ionic liquid, Science 353 (2016) 467–470.
[226] F. Li, L. Chen, G.P. Knowles, D.R. MacFarlane, J. Zhang, Hierarchical mesoporous SnO2 nanosheets on carbon cloth: a robust and flexible electrocatalyst for CO2 reduction with high efficiency and selectivity, Angew. Chem. Int. Ed. 56 (2017) 505–509.
[227] S. Gao, Z. Sun, W. Liu, X. Jiao, X. Zu, Q. Hu, Y. Sun, T. Yao, W. Zhang, S. Wei, Y. Xie, Atomic layer confined vacancies for atomic-level insights into carbon dioxide electroreduction, Nat. Commun. 8 (2017) 14503.
[228] F. Li, L. Chen, M. Xue, T. Williams, Y. Zhang, D.R. MacFarlane, J. Zhang, Towards a better Sn: efficient electrocatalytic reduction of CO2 to formate by Sn/SnS2 derived from SnS2 nanosheets, Nano Energy 31 (2017) 270–277.
[229] H. Wang, Y. Chen, X. Hou, C. Ma, T. Tan, Nitrogen-doped graphenes as efficient electrocatalysts for the selective reduction of carbon dioxide to formate in aqueous solution, Green Chem. 18 (2016) 3250–3256.
[230] F. Lei, W. Liu, Y. Sun, J. Xu, K. Liu, L. Liang, T. Yao, B. Pan, S. Wei, Y. Xie, Metallic tin quantum sheets confined in graphene toward high-efficiency carbon dioxide electroreduction, Nat. Commun. 7 (2016) 12697.
[231] P. Su, K. Iwase, S. Nakanishi, K. Hashimoto, K. Kamiya, Nickel-nitrogen-modified graphene: an efficient electrocatalyst for the reduction of carbon dioxide to carbon monoxide, Small 12 (2016) 6083–6089.
[232] K. Jiang, S. Siahrostami, T. Zheng, Y. Hu, S. Hwang, E. Stavitski, Y. Peng, J. Dynes, M. Gangisetty, D. Su, K. Attenkofer, H. Wang, Isolated Ni single atoms in graphene nanosheets for high-performance CO2 reduction, Energy Environ. Sci. 11 (2018) 893–903.
[233] K. Jiang, S. Siahrostami, A.J. Akey, Y. Li, Z. Lu, J. Lattimer, Y. Hu, C. Stokes, M. Gangishetty, G. Chen, Y. Zhou, W. Hill, W.-B. Cai, D. Bell, K. Chan, J. K. Nørskov, Y. Cui, H. Wang, Transition-metal single atoms in a graphene shell as active centers for highly efficient artificial photosynthesis, Chem 3 (2017) 950–960.
[234] X. Zhang, Z. Wu, X. Zhang, L. Li, Y. Li, H. Xu, X. Li, X. Yu, Z. Zhang, Y. Liang, H. Wang, Highly selective and active CO2 reduction electrocatalysts based on cobalt phthalocyanine/carbon nanotube hybrid structures, Nat. Commun. 8 (2017) 14675.
[235] Z.P. Jovanov, H.A. Hansen, A.S. Varela, P. Malacrida, A.A. Peterson, J.K. Nørskov, I.E.L. Stephens, I. Chorkendorff, Opportunities and challenges in the electrocatalysis of CO2 and CO reduction using bifunctional surfaces: a theoretical and experimental study of Au–Cd alloys, J. Catal. 343 (2016) 215–231.
[236] X. Sun, Q. Zhu, X. Kang, H. Liu, Q. Qian, J. Ma, Z. Zhang, G. Yang, B. Han, Design of a Cu(i)/C-doped boron nitride electrocatalyst for efficient conversion of CO2 into acetic acid, Green Chem. 19 (2017) 2086–2091.
[237] E. Velez-Fort, C. Mathieu, E. Pallecchi, M. Pigneur, M.G. Silly, R. Belkhou, M. Marangolo, A. Shukla, F. Sirotti, A. Ouerghi, Epitaxial graphene on 4H-SiC (0001) grown under nitrogen flux: evidence of low nitrogen doping and high charge transfer, ACS Nano 6 (2012) 10893–10900.
[238] X. Chang, T. Wang, J. Gong, CO2 photo-reduction: insights into CO2 activation and reaction on surfaces of photocatalysts, Energy Environ. Sci. 9 (2016) 2177–2196.
[239] S. Gao, Y. Lin, X. Jiao, Y. Sun, Q. Luo, W. Zhang, D. Li, J. Yang, Y. Xie, Partially oxidized atomic cobalt layers for carbon dioxide electroreduction to liquid fuel, Nature 529 (2016) 68–71.
[240] M.A. Abbas, J.H. Bang, Rising again: opportunities and challenges for platinum-free electrocatalysts, Chem. Mater. 27 (2015) 7218–7235.
[241] W. Zhu, R. Michalsky, Ö. Metin, H. Lv, S. Guo, C.J. Wright, X. Sun, A.A. Peterson, S. Sun, Monodisperse Au nanoparticles for selective electrocatalytic reduction of CO2 to CO, J. Am. Chem. Soc. 135 (2013) 16833–16836.
[242] W. Zhu, Y.-J. Zhang, H. Zhang, H. Lv, Q. Li, R. Michalsky, A.A. Peterson, S. Sun, Active and selective conversion of CO2 to CO on ultrathin Au nanowires, J. Am. Chem. Soc. 136 (2014) 16132–16135.
[243] Q. Fan, M. Zhang, M. Jia, S. Liu, J. Qiu, Z. Sun, Electrochemical CO2 reduction to C2+ species: heterogeneous electrocatalysts, reaction pathways, and optimization strategies, Mater. Today Energy 10 (2018) 280–301.
[244] C.-T. Dinh, T. Burdyny, M.G. Kibria, A. Seifitokaldani, C.M. Gabardo, F.P. García de Arquer, A. Kiani, J.P. Edwards, P. De Luna, O.S. Bushuyev, C. Zou, R. Quintero-Bermudez, Y. Pang, D. Sinton, E.H. Sargent, CO2 electroreduction to ethylene via hydroxide-mediated copper catalysis at an abrupt interface, Science 360 (2018) 783–787.
[245] B.A. Rosen, A. Salehi-Khojin, M.R. Thorson, W. Zhu, D.T. Whipple, P.J.A. Kenis, R.I. Masel, Ionic liquid–mediated selective conversion of CO2 to CO at low overpotentials, Science 334 (2011) 643–644.
[246] B. Kumar, M. Asadi, D. Pisasale, S. Sinha-Ray, B.A. Rosen, R. Haasch, J. Abiade, A. L. Yarin, A. Salehi-Khojin, Renewable and metal-free carbon nanofibre catalysts for carbon dioxide reduction, Nat. Commun. 4 (2013) 2819.
[247] M. Asadi, B. Kumar, A. Behranginia, B.A. Rosen, A. Baskin, N. Repnin, D. Pisasale, P. Phillips, W. Zhu, R. Haasch, R.F. Klie, P. Král, J. Abiade, A. Salehi-Khojin, Robust carbon dioxide reduction on molybdenum disulphide edges, Nat. Commun. 5 (2014) 4470.
[248] B.A. Rosen, I. Hod, Tunable molecular-scale materials for catalyzing the low-overpotential electrochemical conversion of CO2, Adv. Mater. 30 (2018) 1706238.
[249] C. Chen, J.F. Khosrowabadi Kotyk, S.W. Sheehan, Progress toward commercial application of electrochemical carbon dioxide reduction, Chem 4 (2018) 2571–2586.
[250] M. Jouny, W. Luc, F. Jiao, High-rate electroreduction of carbon monoxide to multi-carbon products, Nat. Catal. 1 (2018) 748–755.
[251] C. Hu, Y. Hu, C. Fan, L. Yang, Y. Zhang, H. Li, W. Xie, Surface-enhanced Raman spectroscopic evidence of key intermediate species and role of NiFe dual-catalytic center in water oxidation, Angew. Chem. Int. Ed. 60 (2021) 19774–19778.

[252] K. Khan, T. Liu, M. Arif, X. Yan, M.D. Hossain, F. Rehman, S. Zhou, J. Yang, C. Sun, S.-H. Bae, J. Kim, K. Amine, X. Pan, Z. Luo, Laser-irradiated holey graphene-supported single-atom catalyst towards hydrogen evolution and oxygen reduction, Adv. Energy Mater. 11 (2021) 2101619.
[253] A. Liu, Y. Yang, D. Kong, X. Ren, M. Gao, X. Liang, Q. Yang, J. Zhang, L. Gao, T. Ma, DFT study of the defective carbon materials with vacancy and heteroatom as catalyst for NRR, Appl. Surf. Sci. 536 (2021) 147851.
[254] N. Zhang, B. Yang, K. Liu, H. Li, G. Chen, X. Qiu, W. Li, J. Hu, J. Fu, Y. Jiang, M. Liu, J. Ye, Machine learning in screening high performance electrocatalysts for CO2 reduction, Small Methods 5 (2021) 2100987.
[255] Y.-N. Gong, C.-Y. Cao, W.-J. Shi, J.-H. Zhang, J.-H. Deng, T.-B. Lu, D.-C. Zhong, Modulating the electronic structures of dual-atom catalysts via coordination environment engineering for boosting CO2 electroreduction, Angew. Chem. Int. Ed. 61 (2022) e202215187.
[256] X. Zhao, K. Zhao, Y. Liu, Y. Su, S. Chen, H. Yu, X. Quan, Highly efficient electrochemical CO2 reduction on a precise homonuclear diatomic Fe–Fe catalyst, ACS Catal. 12 (2022) 11412–11420.
[257] W. Yang, Z. Jia, B. Zhou, L. Chen, X. Ding, L. Jiao, H. Zheng, Z. Gao, Q. Wang, H. Li, Why is C–C coupling in CO2 reduction still difficult on dual-atom electrocatalysts? ACS Catal. 13 (2023) 9695–9705.
[258] Y. Han, H. Xu, Q. Li, A. Du, X. Yan, DFT-assisted low-dimensional carbon-based electrocatalysts design and mechanism study: a review, Front. Chem. 11 (2023).
[259] H. Zhang, Y. Liu, T. Chen, J. Zhang, J. Zhang, X.W. Lou, Unveiling the activity origin of electrocatalytic oxygen evolution over isolated Ni atoms supported on a N-doped carbon matrix, Adv. Mater. 31 (2019) 1904548.
[260] T. Ouyang, Y.-Q. Ye, C.-Y. Wu, K. Xiao, Z.-Q. Liu, Heterostructures composed of N-doped carbon nanotubes encapsulating cobalt and β-Mo2C nanoparticles as bifunctional electrodes for water splitting, Angew. Chem. Int. Ed. 58 (2019) 4923–4928.
[261] X. Wang, Y. Jia, X. Mao, L. Zhang, D. Liu, L. Song, X. Yan, J. Chen, D. Yang, J. Zhou, K. Wang, A. Du, X. Yao, A directional synthesis for topological defect in carbon, Chem 6 (2020) 2009–2023.
[262] H. Jiang, J. Gu, X. Zheng, M. Liu, X. Qiu, L. Wang, W. Li, Z. Chen, X. Ji, J. Li, Defect-rich and ultrathin N doped carbon nanosheets as advanced trifunctional metal-free electrocatalysts for the ORR, OER and HER, Energy Environ. Sci. 12 (2019) 322–333.
[263] S. Ye, F. Luo, Q. Zhang, P. Zhang, T. Xu, Q. Wang, D. He, L. Guo, Y. Zhang, C. He, X. Ouyang, M. Gu, J. Liu, X. Sun, Highly stable single Pt atomic sites anchored on aniline-stacked graphene for hydrogen evolution reaction, Energy Environ. Sci. 12 (2019) 1000–1007.
[264] V. Fung, G. Hu, Z. Wu, D.-e. Jiang, Descriptors for hydrogen evolution on single atom catalysts in nitrogen-doped graphene, J. Phys. Chem. C 124 (2020) 19571–19578.
[265] Y. Jia, L. Zhang, A. Du, G. Gao, J. Chen, X. Yan, C.L. Brown, X. Yao, Defect graphene as a trifunctional catalyst for electrochemical reactions, Adv. Mater. 28 (2016) 9532–9538.
[266] B. Zhu, L. Zhang, D. Xu, B. Cheng, J. Yu, Adsorption investigation of CO2 on g-C3N4 surface by DFT calculation, J. CO2 Util. 21 (2017) 327–335.
[267] X. Mao, S. Zhou, C. Yan, Z. Zhu, A. Du, A single boron atom doped boron nitride edge as a metal-free catalyst for N2 fixation, Phys. Chem. Chem. Phys. 21 (2019) 1110–1116.
[268] X. Guo, S. Lin, J. Gu, S. Zhang, Z. Chen, S. Huang, Simultaneously achieving high activity and selectivity toward two-electron O2 electroreduction: the power of single-atom catalysts, ACS Catal. 9 (2019) 11042–11054.
[269] D. Raciti, C. Wang, Recent advances in CO2 reduction electrocatalysis on copper, ACS Energy Lett. 3 (2018) 1545–1556.
[270] X. Mao, C. Tang, T. He, D. Wijethunge, C. Yan, Z. Zhu, A. Du, Computational screening of MN4 (M = Ti–Cu) based metal organic frameworks for CO2 reduction using the d-band centre as a descriptor, Nanoscale 12 (2020) 6188–6194.
[271] S. Back, J. Lim, N.-Y. Kim, Y.-H. Kim, Y. Jung, Single-atom catalysts for CO2 electroreduction with significant activity and selectivity improvements, Chem. Sci. 8 (2017) 1090–1096.
[272] M.S.A. Bhuyan, M.N. Uddin, M.M. Islam, F.A. Bipasha, S.S. Hossain, Synthesis of graphene, Int. Nano Lett. 6 (2016) 65–83.
[273] N. Kumar, R. Salehiyan, V. Chauke, O. Joseph Botlhoko, K. Setshedi, M. Scriba, M. Masukume, S. Sinha Ray, Top-down synthesis of graphene: a comprehensive review, FlatChem 27 (2021) 100224.
[274] X. Zhang, G. Ma, J. Wang, Hydrothermal synthesis of two-dimensional MoS2 and its applications, Tungsten 1 (2019) 59–79.
[275] Y. Stehle, H.M. Meyer III, R.R. Unocic, M. Kidder, G. Polizos, P.G. Datskos, R. Jackson, S.N. Smirnov, I.V. Vlassiouk, Synthesis of hexagonal boron nitride monolayer: control of nucleation and crystal morphology, Chem. Mater. 27 (2015) 8041–8047.
[276] D. Monga, S. Sharma, N.P. Shetti, S. Basu, K.R. Reddy, T.M. Aminabhavi, Advances in transition metal dichalcogenide-based two-dimensional nanomaterials, Mater. Today Chem. 19 (2021) 100399.
[277] K.N. Dinh, Y. Zhang, J. Zhu, W. Sun, Phosphorene-based electrocatalysts, Chem. Eur J. 26 (2020) 6437–6446.
[278] Q. Fu, J. Han, X. Wang, P. Xu, T. Yao, J. Zhong, W. Zhong, S. Liu, T. Gao, Z. Zhang, L. Xu, B. Song, 2D transition metal dichalcogenides: design, modulation, and challenges in electrocatalysis, Adv. Mater. 33 (2021) 1907818.
[279] D. Voiry, J. Yang, M. Chhowalla, Recent strategies for improving the catalytic activity of 2D TMD nanosheets toward the hydrogen evolution reaction, Adv. Mater. 28 (2016) 6197–6206.
[280] M. Fortin-Deschênes, F. Xia, Synthesis of black phosphorus films, Nat. Mater. 22 (2023) 681–682.